

---

## DRAFT VERSION of PART II:

### Invertible Orientation Scores

R. Duits · E.J. Bekkers

**Abstract** Inspired by the early visual system of many mammals we consider the construction of-and reconstruction from- an orientation score  $U_f : \mathbb{R}^d \times S^{d-1} \rightarrow \mathbb{C}$  as a local orientation representation of an image,  $f : \mathbb{R}^d \rightarrow \mathbb{R}$  for  $d \in \{2, 3\}$ . The mapping  $f \mapsto U_f$  is a wavelet transform  $\mathcal{W}_\psi$  corresponding to a reducible representation of the Euclidean motion group onto  $\mathbb{L}_2(\mathbb{R}^d)$  and oriented wavelet  $\psi \in \mathbb{L}_2(\mathbb{R}^d)$ . This wavelet transform is a special case of generalized wavelet theory and has the practical advantage over the usual wavelet approaches in image analysis (constructed by irreducible representations of the similitude group) that it allows a stable reconstruction from one ('all scale') orientation score. Since our wavelet transform is a unitary mapping with stable inverse, we directly relate operations on orientation scores to operations on images in a robust manner.

Furthermore, we show that an operator  $\Phi$  on orientation scores must be left invariant to ensure that the corresponding operator  $\mathcal{W}_\psi^{-1} \circ \Phi \circ \mathcal{W}_\psi$  on images is Euclidean invariant. The specific design of left-invariant operators (e.g. diffusions, wavefront propagation) will be pursued in subsequent sections.

**Literature:** This section of the lecture notes is primarily based on the following scientific works [18, 48, 2, 52, 19, 6, 23, 25, 24].

#### Learning objectives:

- Understand the general benefits of an invertible orientation score.
- Understand that the domain of an orientation score of a 2D image is the Lie group  $SE(2)$ .
- Understand that the domain of an orientation score of a 3D image is the Lie group quotient  $SE(3)/(0 \times SO(2))$
- Understand why orientation score processing must be left-invariant and not right-invariant.
- Know how to apply invertible orientation scores to images via the 'Lie-Analysis' *Mathematica* package. To be downloaded from [www.lieanalysis.nl](http://www.lieanalysis.nl)
- Know how to prove general unitarity results.
- Understand the design of proper wavelets for invertible orientation scores.

#### NB:

Technical parts and exercises with extra material are indicated in **blue** and may be skipped: The black text forms the core of the course and does not rely on the blue parts. Regular exercises are indicated in **red**.

In many medical image applications it is desirable to construct a local orientation-score of a grey-value image. In the case of 2D images  $f : \mathbb{R}^2 \rightarrow \mathbb{R}$  such an orientation score  $U_f : \mathbb{R}^2 \times S^1 \rightarrow \mathbb{C}$  depends on 3 variables  $(b_1, b_2, e^{i\theta})$ , where  $\mathbf{b} = (b_1, b_2) \in \mathbb{R}^2$  denote position and where  $e^{i\theta} \in S^1 \leftrightarrow (\cos \theta, \sin \theta) \in S^1$  is a local orientation variable.

---

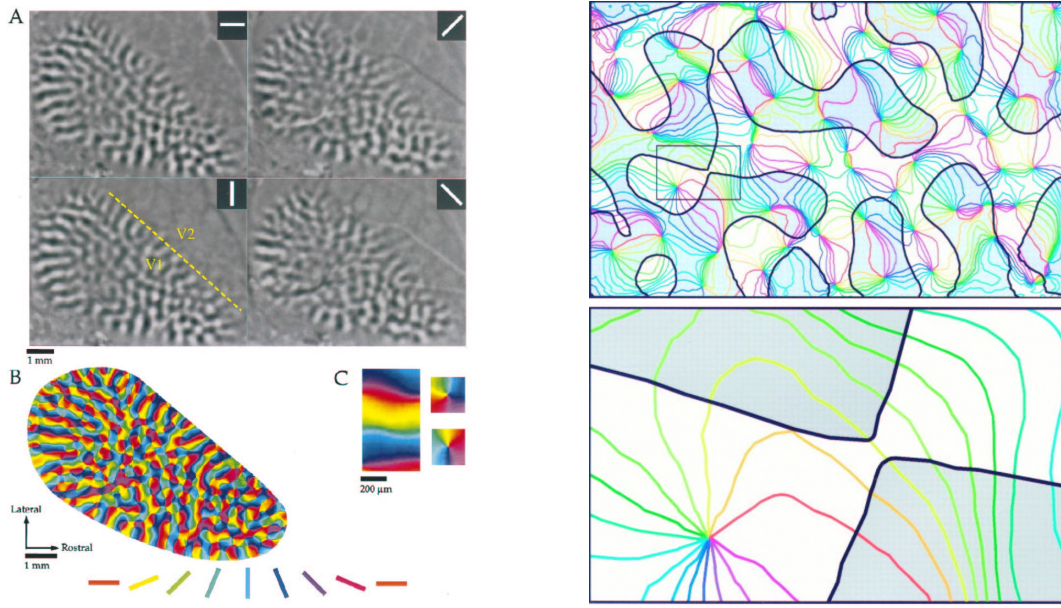


**Fig. 1 Inspiration for Orientation Scores.** Left: A: Parts of visual cortex active under different orientation stimuli. B: Orientation preference map obtained by vector summation of data obtained for each angle. Orientation preference is color coded according to the key shown below, replicated with permission from [9], copyright 1997 Society of Neuroscience. Right: enlarged section of the rectangular area in the upper figure. Shaded and unshaded areas denote the left and right eye resp. Colored lines connect cells with equal orientation sensitivity, replicated with permission from [73].

Mostly, such an **orientation score** is obtained by means of a convolution with some anisotropic wavelet  $\psi \in \mathbb{L}_2(\mathbb{R}^2) \cap \mathbb{L}_1(\mathbb{R}^2)$ , cf. [52], [41]:

$$U_f(\mathbf{b}, e^{i\theta}) = \int_{\mathbb{R}^2} \overline{\psi(R_\theta^{-1}(\mathbf{x}' - \mathbf{b}))} f(\mathbf{x}') d\mathbf{x}', \quad \text{with } R_\theta = \begin{pmatrix} \cos \theta & -\sin \theta \\ \sin \theta & \cos \theta \end{pmatrix}. \quad (1)$$

This idea is inspired by the early visual system of many mammals, in which receptive fields exist that are tuned to various locations and orientations. Thereby a simple cell receptive field can be parameterized by its position and orientation. Assemblies of oriented receptive fields are grouped together on the surface of the primary visual cortex in a pinwheel like structure, known as the orientation preference structure.

The orientation preference structure is an almost everywhere smooth mapping of the Euclidean motion group space  $\mathbb{R}^2 \times S^1$  onto the 2D surface. Due to the difference in dimensionality, the orientation preference structure is punctuated by so-called pinwheels, which are singularities in this mapping, see Figure 1.

For a conceptually convincing overview of the role of sub-Riemannian geometry (and orientation analysis) in modeling the perception of curvilinear structures in the primary visual cortex we refer to the pioneering works of Petitot and Citti-Sarti [61, 62, 13]. These interesting works on cortical modeling may be considered as a source of inspiration for our objective of developing (digital) image processing tools via invertible orientation scores.

See Figure 2 for an illustration of the construction of an orientation score of a 2D image. As invertible orientation scores are actually complex-valued with a real part indicating all local lines in images, and an imaginary part indicating all local edges in images (as we will explain later), we stress that in Figure 2 only the real part of the orientation score is visualized. In Figure 3 we show a key advantage of an orientation score, we enlarge the domain of an image, which allows for crossing wavefronts. In Figure 4 we give two simple examples of image processing via invertible orientation scores.

Perceptual organization (or image enhancement) on the basis of orientation similarity on images  $f$  can be done via their orientation scores  $U_f$ , as there exists a linear *well-posed invertible* transformation  $\mathcal{W}_\psi$  from the image  $f$  to the orientation score  $U_f$  and vice versa. This invertibility ensures that no information is lost in the decomposition of an input image into various orientations. Regarding the orientation preference structure in the visual system this implies that the orientation score may serve as an alternative format

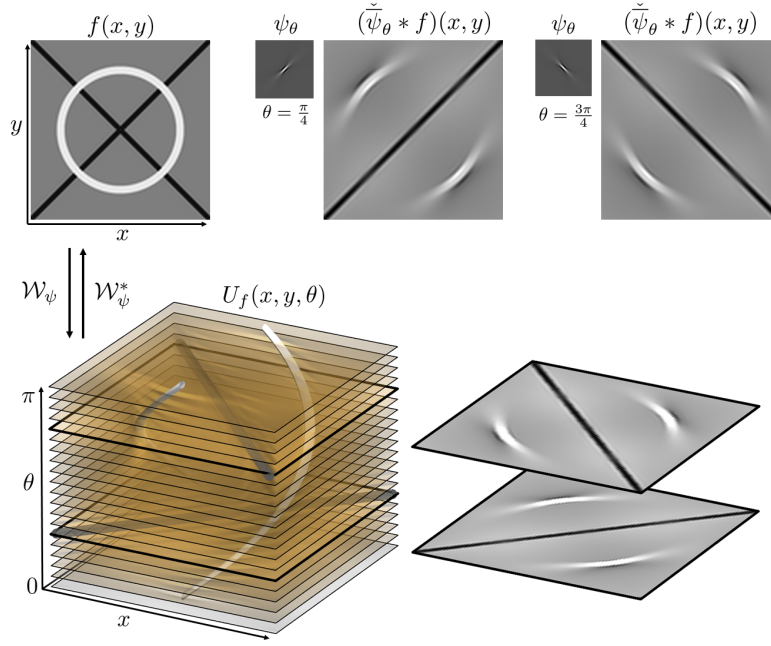


**Fig. 2 Construction of Orientation Scores.** An orientation score is constructed by filtering an image with a set of rotated anisotropic filters. Here we show only the real part of the orientation score. The top row shows two of such rotated filters and their responses on the input image. In an orientation score  $U_f$ , obtained via the orientation score transform  $\mathcal{W}_\psi$ , such responses are “stacked” on top of each other. Using so-called cake-wavelets (to be explained in Sec. 3.1) for  $\psi$  one obtains an invertible orientation score transformation  $\mathcal{W}_\psi$ , for which a stable inverse transformation  $\mathcal{W}_\psi^*$  exists: one can reconstruct the image from the orientation score without loss of information.

to the input luminance function, since there is no loss of data evidence<sup>1</sup>. As a tool for image processing, however, the inverse mapping from orientation score to original image is a very useful one as we will see later.

The domain of an orientation score  $U_f$  is the well-known Euclidean motion group  $G = SE(2) = \mathbb{R}^2 \rtimes S^1$ , with group product

$$g g' = (\mathbf{b}, e^{i\theta})(\mathbf{b}', e^{i\theta'}) = (\mathbf{b} + R_\theta \mathbf{b}', e^{i(\theta+\theta')}) , g = (\mathbf{b}, e^{i\theta}), g' = (\mathbf{b}', e^{i\theta'}) \in \mathbb{R}^2 \rtimes S^1. \quad (2)$$

and the mapping  $f \mapsto U_f$  is a wavelet transformation<sup>2</sup>

$$U_f(\mathbf{b}, e^{i\theta}) := (\mathcal{W}_\psi[f])(g) := (\mathcal{U}_g \psi, f)_{\mathbb{L}_2(\mathbb{R}^2)} = (\mathcal{T}_\mathbf{b} \mathcal{R}_{e^{i\theta}} \psi, f)_{\mathbb{L}_2(\mathbb{R}^2)} , \quad g = (\mathbf{b}, e^{i\theta}) , \quad (3)$$

where  $\mathcal{T}_\mathbf{b} \mathcal{R}_{e^{i\theta}} \psi$  is the translated and rotated wavelet and the representation  $g \mapsto \mathcal{U}_g$  is given by

$$\mathcal{U}_g \psi(\mathbf{x}) = (\mathcal{T}_\mathbf{b} \mathcal{R}_{e^{i\theta}} \psi)(\mathbf{x}) = \psi(R_\theta^{-1}(\mathbf{x} - \mathbf{b})) , \quad g = (\mathbf{b}, e^{i\theta}) \in G, \mathbf{x} \in \mathbb{R}^2, \quad (4)$$

where  $(\mathcal{T}_\mathbf{b} \psi)(\mathbf{x}) = \psi(\mathbf{x} - \mathbf{b})$ ,  $\mathbf{x} \in \mathbb{R}^d$  and  $(\mathcal{R}_{e^{i\theta}} \psi)(\mathbf{x}) = \psi(R_\theta^{-1} \mathbf{x})$ , with  $R_\theta$ ,  $\theta \in [0, 2\pi)$ , the counter clock-wise rotation given in (1).

Because the local orientation is explicitly encoded in the orientation score, it is much easier to do (enhancement or perceptual organization) operations based on local orientations in the score.

<sup>1</sup> This does *not* imply that the visual system of mammals actually runs an inverse process.

<sup>2</sup> Note that we take the convention that inner-products are linear in the second entry.

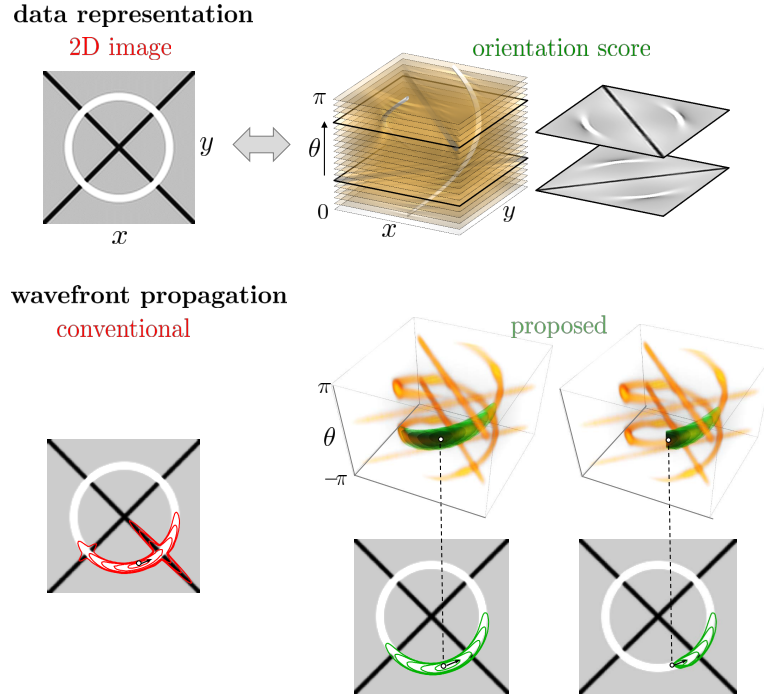


**Fig. 3 The Advantage of an Orientation Score.** Top: An invertible orientation score is an image representation that provides a complete overview of how the image is decomposed out of local orientations. Bottom: Conventional wavefront propagation in images (in red) typically leaks at crossings, whereas the wavefront propagation in orientation scores (in green) does not suffer from this fundamental complication. A minimum intensity projection over orientation gives the optimal fronts in the image. The orange densities denote mobility in the score. This regulates the speed of the propagation of the green opaque spheres (whose precise geometric meaning will be explained later in Part III).

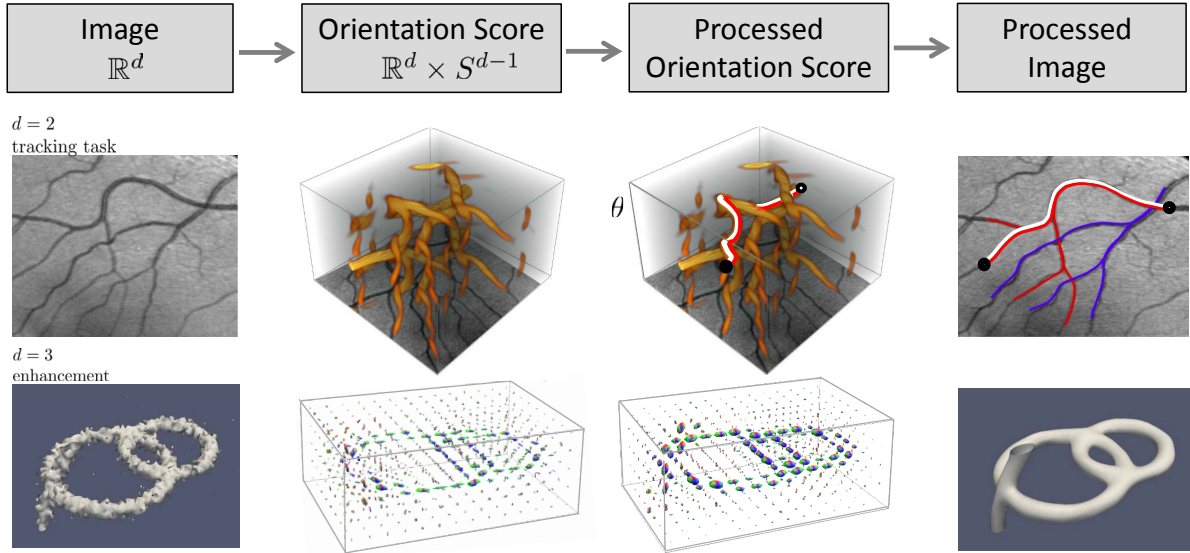


**Fig. 4 Processing via Invertible Orientation Score.** Top: instead of direct processing of an image, we process via an invertible orientation score. Such a score is obtained by convolving the image with a family of rotated proper wavelets allowing for stable reconstruction (cf. Theorem 2 and Theorem 3). Second row: Example of vessel-tracking in a 2D image via orientation scores as we will explain in Part III. Third row: Example of crossing-preserving diffusion via invertible orientation scores of a basic 3D image [48]. Here the modulus of the (processed) orientation score is 5D and visualized by a grid of angular profiles (see preliminaries, Eq. (7)).



## Structure of Part II

In Section 1 we will investigate and quantify the wellposedness of the transform  $\mathcal{W}_\psi$  between images and orientation scores, which depends strongly on the choice of mother-wavelet  $\psi$ .

We first motivate in Subsection 1.1 why standard continuous wavelet theory does not apply to our case of interest.

Then in Subsection 1.2 we will start with a general reproducing kernel Hilbert space view-point which leads to a general unitarity result in Lemma 4 and a sampling theorem in Lemma 5. This yields a general view on continuous wavelet theory. For example, although convenient, the  $SE(d)$  group structure (which is important for processing on orientation scores) is actually irrelevant for unitarity results. It is also not needed to maintain such a group structure in finite discretizations; for  $d > 2$  it would be too restrictive.

In Subsection 1.3 we summarize the main unitarity result for the orientation score transform  $\mathcal{W}_\psi$  in Theorem 2. Here we note that if one wants to drop the constraint to disk limited images for the orientation score transform, one must rely on distributional wavelet transforms and this explained in Appendix A.

In Subsection 1.4 we will show that the wellposedness of  $\mathcal{W}_\psi$  is highly dependent on the choice of wavelet  $\psi$  via a continuous function  $M_\psi$ , which is summarized in Theorem 2, while analyzing formal condition numbers in Theorem 3. We introduce the notion of proper wavelets, that allow stable reconstruction. Here we also account for proper wavelets with the fast reconstruction property, in the sense that a practical integration over angles only suffices for a close approximate image reconstruction.

In Subsection 1.5 we account for a finite number of orientations, and introduce the notion of proper wavelet sets.

Although group representation theory is not crucial for the unitarity results, it does provide a nice structured insight in the construction of proper wavelets via (inverse) Fourier transform on  $SE(2)$ .

In Section 2 we express  $\mathcal{W}_\psi$  as an inverse Fourier transform in Eq. (59), and deduce unitarity of  $\mathcal{W}_\psi$  via the Plancherel theorem on  $SE(2)$ . It does provide a structured view on Theorem 2. Basically, it shows that the ideal case with  $M_\psi = 1_{B_{0,e}}$  (or  $M_\psi = 1$  in the distributional setting of Appendix A) corresponds to a proper wavelet  $\psi$  with equal quadratic mass in each irreducible subspace in the image domain, such that it is unitarily mapped to the irreducible subspace in the orientation score domain. In fact, this is a over-countable generalization of vector-coherent states [2], and follows general ideas in the work on abstract harmonic analysis by Hartmut Führ [40]. For an in-depth treatment the reader is referred to [40, ch:4,ch:5.2]. For explanations on the tool of direct integrals see [40, ch:3.3].

In Section 3 we study the construction of proper 2D and 3D wavelets (and proper wavelet sets). Here we distinguish between:

- Cakewavelets in Subsection 3.1.
- Proper wavelets by expansion in a basis eigenfunctions of the harmonic oscillator in Subsection 3.2.
- Proper wavelets by expansion in a modified (weighted) Zernike basis in Subsection 3.3.

In Section 4 we will provide a first quick overview on image processing via the constructed invertible orientation scores, that we will pursue in this course. Here we distinguish between:

- Geodesic wavefront propagation in orientation scores.
- Geodesic tracking in orientation scores.
- Crossing preserving diffusions in orientation scores.
- Feature analysis in orientation scores.
- Template matching in orientation scores.

## Preliminaries and Notation

- The Fourier transform  $\mathcal{F} : \mathbb{L}_2(\mathbb{R}^d) \rightarrow \mathbb{L}_2(\mathbb{R}^d)$ , is almost everywhere defined by

$$[\mathcal{F}(f)](\boldsymbol{\omega}) = \hat{f}(\boldsymbol{\omega}) = \frac{1}{(2\pi)^{d/2}} \int_{\mathbb{R}^d} f(\mathbf{x}) e^{-i\boldsymbol{\omega} \cdot \mathbf{x}} d\mathbf{x}.$$

- The convolution  $f_1 * f_2$  of two scalar-valued integrable functions  $f_1 : \mathbb{R}^d \rightarrow \mathbb{C}$  and  $f_2 : \mathbb{R}^d \rightarrow \mathbb{C}$  is the scalarvalued function by

$$(f_1 * f_2)(\mathbf{x}) = \int_{\mathbb{R}^d} f_1(\mathbf{x} - \mathbf{v}) f_2(\mathbf{v}) d\mathbf{v}.$$

Note that  $\|\mathcal{F}f\|^2 = \|f\|^2$  and  $\mathcal{F}(f_1 * f_2) = (2\pi)^{\frac{d}{2}} \mathcal{F}(f_1) \mathcal{F}(f_2)$ , for all  $f_1, f_2 \in \mathbb{L}_2(\mathbb{R}^d)$ .

- let  $f_1, f_2$  be two elements of  $\mathbb{L}_2(\mathbb{R}^d)$  then their  $\mathbb{L}_2$ -inner product is denoted by

$$(f_1, f_2)_{\mathbb{L}_2(\mathbb{R}^d)} = \int_{\mathbb{R}^d} \overline{f_1(\mathbf{x})} f_2(\mathbf{x}) d\mathbf{x}.$$

- For  $d = 2$ : We use the following notation for Euclidean/polar coordinates in spatial and Fourier domain, respectively:

$$\mathbf{x} = (x^1, x^2)^T = (x, y)^T = (r \cos \phi, r \sin \phi), \quad \boldsymbol{\omega} = (\omega^1, \omega^2)^T = (\rho \cos \varphi, \rho \sin \varphi)^T,$$

with  $\phi, \varphi \in [0, 2\pi)$ ,  $r, \rho > 0$ . The corresponding complex variables will be denoted by  $z = x + iy = r e^{i\phi}$  and  $w = \omega_x + i\omega_y = \rho e^{i\varphi}$ .

- For  $d = 3$ : We use the following notation for Euclidean/Ball coordinates in spatial and Fourier domain:

$$\begin{aligned} \mathbf{x} &= (x^1, x^2, x^3)^T = (x, y, z)^T = r(\cos \phi \sin \theta, \sin \phi \sin \theta, \cos \theta)^T, \\ \boldsymbol{\omega} &= (\omega^1, \omega^2, \omega^3)^T = \rho(\cos \varphi \sin \vartheta, \sin \varphi \sin \vartheta, \cos \vartheta)^T. \end{aligned}$$

- Images are assumed to be within  $\mathbb{L}_2(\mathbb{R}^d)$ . We mainly consider  $d = 2$ , unless explicitly stated otherwise. The space of ball-limited (by  $\varrho > 0$ ) images is given by

$$\mathbb{L}_2^\varrho(\mathbb{R}^d) = \{f \in \mathbb{L}_2(\mathbb{R}^2) \mid \text{supp}(\mathcal{F}[f]) \subset B_{\mathbf{0}, \varrho}\}, \varrho > 0, \quad (5)$$

where  $B_{\mathbf{0}, \varrho} = \{\boldsymbol{\omega} \in \mathbb{R}^d \mid \|\boldsymbol{\omega}\| < \varrho\}$ .

- For  $d = 3$  we often rely on spherical harmonics given by on

$$Y_l^m(\beta, \gamma) = \sqrt{\frac{2l+1}{4\pi}} \sqrt{\frac{(l-m)!}{(l+m)!}} e^{im\gamma} P_l^m(\cos \beta), \quad (6)$$

where  $P_l^m$  is the associated Legendre function and with integer order  $l \geq 0$  and integer phase factor  $-l \leq m \leq l$ .

- With  $B(H)$  we denote the space of bounded linear operators on  $H$ . The range of a linear operator  $A$  will be denoted by  $\mathcal{R}(A)$  and its nilspace will be denoted by  $\mathcal{N}(A)$ .
- The 2D-Gaussian kernel  $G_s$  at scale  $s$  is given by  $G_s(\mathbf{x}) = \frac{1}{4\pi s} e^{-\frac{\|\mathbf{x}\|^2}{4s}}$ .
- **Glyph Visualization** : Functions  $U : \mathbb{R}^3 \times S^2 \rightarrow \mathbb{R}^+$  will be visualized by a glyph visualization. E.g. in the 1 bottom-middle figures of Fig. 4. A glyph at a grid point  $\mathbf{y} \in c \mathbb{Z}^3$ ,  $c > 0$ , is given by the surface

$$\{\mathbf{y} + \nu U(\mathbf{y}, \mathbf{n}) \mathbf{n} \mid \mathbf{n} \in S^2\}, \quad (7)$$

for a suitable choice of  $\nu \in \mathbb{R}$ . Usually we choose  $\nu > 0$  depending on the maximum of  $U$ , such that the glyphs (within the grid of glyphs) do not intersect.

## Preliminaries on Group Representations

### Definition 1 (representations)

A representation  $\mathcal{R}$  of a group  $G$  onto a Banach space  $H$  is a homomorphism  $\mathcal{R}$  between  $G$  and  $B(H)$ , the space of bounded linear operators on  $H$ . I.e. it must satisfy

$$\mathcal{R}_{gh} = \mathcal{R}_g \mathcal{R}_h \text{ for all } g \in G, h \in G, \text{ and } \mathcal{R}_e = I, \quad (8)$$

where  $I$  is the identity map.

**Definition 2** Let  $G$  be a Lie group. Then according Haar's theorem there exist an –up to constant multiplication– *unique* non-trivial Radon measure<sup>3</sup>  $\mu$  on the Borel subset of  $G$  such that it is left-invariant

$$\mu(gS) = \mu(S) \text{ for all } g \in G \text{ and all Borel sets } S \subset G. \quad (9)$$

For measurable functions  $U : G \rightarrow \mathbb{C}$  we use short-notation:

$$\int_G \tilde{U}(g) dg := \int_G \tilde{U}(g) d\mu(g).$$

Left-invariance of the Haar measure (9) gives  $d\mu(qg') = d\mu(g')$  for all  $q, g' \in G$ . In fact (9) amounts to

$$\int_S \tilde{U}(q^{-1}g) dg = \int_S \tilde{U}(g') d(qg') = \int_S \tilde{U}(g') dg', \quad (10)$$

for all measurable functions  $U : S \rightarrow \mathbb{C}$  on some Borel set  $S \subset G$ .

In particular for elements  $\tilde{U} \in \mathbb{L}_p(G)$  with  $p \geq 1$  one writes

$$\|\tilde{U}\|_{\mathbb{L}_p(G)} := \left( \int_G |\tilde{U}(g)|^p dg \right)^{\frac{1}{p}}.$$

### Definition 3 (left/right regular representations)

Let  $G$  be a Lie group. Then its right regular representation  $\mathcal{R} : G \rightarrow B(\mathbb{L}_2(G))$  is given by

$$\mathcal{R}_g \tilde{U}(h) = \tilde{U}(hg) \text{ for all } g, h \in G \text{ and all } \tilde{U} \in \mathbb{L}_2(G), \quad (11)$$

whereas its left regular representation  $\mathcal{L} : G \rightarrow B(\mathbb{L}_2(G))$  is given by

$$\mathcal{L}_g \tilde{U}(h) = \tilde{U}(g^{-1}h) \text{ for all } g, h \in G \text{ and all } \tilde{U} \in \mathbb{L}_2(G) \quad (12)$$

### Definition 4 (properties of representations)

Let  $G$  be a group and  $H$  a Hilbert space.

A representation  $\mathcal{R} : G \rightarrow B(H)$  is said to be irreducible if the only invariant closed subspaces of  $H$  are  $H$  and  $\{0\}$  and otherwise reducible.

A representation  $\mathcal{U} : G \rightarrow B(H)$  is called unitary if  $(\mathcal{U}_g)^* = \mathcal{U}_g^{-1}$  for all  $g \in G$ .

### Examples:

- Let  $G$  be a Lie group. Then the left regular representation  $G \ni g \mapsto \mathcal{L}_g \in B(\mathbb{L}_2(G))$  is a unitary representation.
- Let  $G$  be a Lie group. Then the right regular representation  $G \ni g \mapsto \mathcal{R}_g \in B(\mathbb{L}_2(G))$  is a unitary representation.
- Set  $G = SE(2)$ . Then the left regular action of the Euclidean motion group  $g \mapsto \mathcal{U}_g$  on  $H = \mathbb{L}_2(\mathbb{R}^d)$  given by (4) is unitary representation. We will also show that it is reducible.

### Lemma 1 (Schur's lemma)

Let  $\mathcal{R} : G \rightarrow B(X)$  be an irreducible representation of a Lie group  $G$  on a Banach space  $(X, \|\cdot\|)$ . Let  $A : X \rightarrow X$  be a bounded linear operator on  $X$  such that

$$\forall_{g \in G} : \mathcal{R}_g \circ A = A \circ \mathcal{R}_g$$

then  $A$  is a scalar multiple of the identity  $A = \lambda I$  for some  $\lambda \in \mathbb{C}$ .

<sup>3</sup> I.e. countably additive, regular (inner-regular and outer regular), and its assigns finite values to compact sets.

*Proof.* As  $A$  is bounded and linear it is continuous and for all  $\mu \in \mathbb{C}$  we have  $V := \mathcal{N}(A - \mu I)$  is closed in  $(X, \|\cdot\|)$ . Now for all  $g \in G$  the operator  $\mathcal{R}_g$  maps  $V$  onto itself. So either  $V = \{0\}$  or  $V = X$ . Now any operator has a complex eigenvalue say  $\lambda \in \mathbb{C}$ . Then choose  $\mu = \lambda$  in which case  $V \neq \{0\}$  so that  $\mathcal{N}(A - \lambda I) = X$  so that  $A = \lambda I$ .  $\square$

**Definition 5** (matrix groups)

We define the following matrix groups:

- $\text{Aut}(\mathbb{R}^d) = \{A : \mathbb{R}^d \rightarrow \mathbb{R}^d \mid A \text{ linear and } A^{-1} \text{ exists}\}$
- dilation group  $D(d) = \{A \in \text{Aut}(\mathbb{R}^d) \mid A = aI, a > 0\}$ .
- orthogonal group  $O(d) = \{X \in \text{Aut}(\mathbb{R}^d) \mid X^T = X^{-1}\}$
- rotation group  $SO(d) = \{R \in O(d) \mid \det(R) = 1\}$ .
- circle group  $S^1 = \{z \in \mathbb{C} \mid |z| = 1\}$ ,  $z = e^{i\theta}$ ,  $\theta = \arg z$  with group homomorphism  $\tau : S^1 \rightarrow SO(2) \subset \text{Aut}(\mathbb{R}^2)$ , given by  $\tau(z) = R_\theta$ , recall (1).
- roto-translation group  $SE(2) = \mathbb{R}^2 \rtimes SO(2)$  with group product (2).
- Set  $d \in \{2, 3\}$ . Then the roto-translation group  $SE(d) = \mathbb{R}^d \rtimes SO(d)$  is equipped with group product

$$g_1 g_2 = (\mathbf{x}_1, R_1)(\mathbf{x}_2, R_2) = (\mathbf{x}_1 + R_1 \mathbf{x}_2, R_1 R_2), \quad (13)$$

for all  $(\mathbf{x}_1, R_1) \in \mathbb{R}^d \rtimes SO(d)$  and all  $(\mathbf{x}_2, R_2) \in \mathbb{R}^d \rtimes SO(d)$ .

(NB. Since it is a *semi*-direct product (as the rotation element  $R_1$  affects the product in the spatial part in (13)) we write  $SE(d) = \mathbb{R}^d \rtimes SO(d)$  instead of  $\mathbb{R}^d \times SO(d)$ ).

Note that  $S^1 \equiv SO(2) \equiv \mathbb{R}/[0, 2\pi)$  under identification

$$e^{i\theta} \leftrightarrow R_\theta \leftrightarrow \theta(\text{Mod } 2\pi). \quad (14)$$

In the lecture notes we will sometimes rely on this straightforward identification.

*Example 1* Under identification (14) the Haar measure on  $SE(2)$  is given by (verify its left-invariance (10)!):

$$dg = d\mathbf{x}d\theta. \quad (15)$$

so that for all measurable functions  $\tilde{U} : G \rightarrow \mathbb{C}$  one has

$$\int_G \tilde{U}(g) dg = \int_{-\pi}^{\pi} \int_{\mathbb{R}^2} \tilde{U}(\mathbf{x}, \theta) d\mathbf{x}d\theta.$$

**Definition 6** Let  $\mathbf{b} \in \mathbb{R}^d$ ,  $a > 0$ . Then the unitary operators  $f \mapsto \check{f}$ ,  $\tau_{\mathbf{b}}$ ,  $\mathcal{D}_a$  are defined by

$$\check{f}(\mathbf{x}) = f(-\mathbf{x}) \text{ and } \mathcal{T}_{\mathbf{b}}\psi(\mathbf{x}) = \psi(\mathbf{x} - \mathbf{b}) \text{ and } \mathcal{D}_a\psi(\mathbf{x}) = \frac{1}{a^{\frac{d}{2}}} \psi\left(\frac{\mathbf{x}}{a}\right), \quad (16)$$

which are left regular actions of  $O(1)$ ,  $\mathbb{R}^d$ ,  $D(d)$  in  $\mathbb{L}_2(\mathbb{R}^d)$ .

**Definition 7** (generators of group representations)

Let  $H$  be a Hilbert space. Let  $\mathcal{V} : G \rightarrow B(H)$  be some group representation of a Lie group  $G$  with unity element  $e$ . Let  $T_e(G)$  denote the Lie algebra of the Lie group. Let  $A \in T_e(G)$ . Then the corresponding generator/derivative  $d\mathcal{V}(A)$  is defined as follows:

$$d\mathcal{V}(A)f := \lim_{t \rightarrow 0} t^{-1}(\mathcal{V}_{e^{tA}} - I)f, \text{ for all } f \in \mathcal{D}_H, \quad (17)$$

where  $\mathcal{D}_H \subset H$  is a domain of sufficiently regular  $f \in H$  such that limit  $d\mathcal{V}(A)f$  exists in  $H$ .

**Exercise 1** (group-representations)

a.) Show that for any group-representation  $\mathcal{R} : G \rightarrow B(H)$  on some Banach space  $H$  one has that

$$\mathcal{R}_{g^{-1}} = (\mathcal{R}_g)^{-1} \text{ for all } g \in G.$$

- b.) Assume that the Haar measure on  $G$  is both left and right-invariant, i.e.  $d\mu_G(hg) = d\mu_G(gh) = d\mu_G(g)$  for all  $h, g \in G$ .  
 Show that the above group-representations  $\mathcal{U}$ ,  $\mathcal{L}$  and  $\mathcal{R}$  (given by respectively (4), (12) and (11)) are indeed group representations. I.e. show that they indeed satisfy (8).
- c.) Show that the above group-representations  $\mathcal{U}$ ,  $\mathcal{L}$  and  $\mathcal{R}$  are indeed *unitary* group representations.
- d.) Show that Lie group  $SE(d)$  equipped with product (13) can be identified with a matrix group that is a subgroup of  $GL(d+1)$ .  
*hint:  $(\mathbf{x}, R) \leftrightarrow \begin{pmatrix} R & \mathbf{x} \\ \mathbf{0} & 1 \end{pmatrix}$ .*
- e.) Set  $G = SE(2) \equiv \mathbb{R}^2 \times S^1$ . Consider the unity element  $e = (\mathbf{x} = (x, y) = (0, 0), \theta = 0)$ . Set  $A_3 = \partial_\theta|_e$ . Show that

$$d\mathcal{U}(A_3) = +y\partial_x - x\partial_y.$$

*hint: note that  $e^{tA_3} = (0, 0, e^{it})$  recall Exercise 12 of Part I of the lecture notes.*

## 1 Quantification of Wellposedness of Transformations between Image and Orientation Score

Because the local orientation is explicitly encoded in the orientation score, it is much easier to do (enhancement or perceptual organization) operations based on local orientations on the score. However, well-posed image enhancement on the basis of orientation similarity in an image  $f$  (without loss of data evidence) can be done via its orientation score  $U_f$  iff there exists a stable transformation from image  $f$  to  $U_f$  and vice versa. Stability entails that a small<sup>4</sup> perturbation in the image, must correspond to a small perturbation on the orientation score and vice versa. For instance in the case of the Fourier transform, the stability is ensured by the Plancherel theorem, which states that  $\|\mathcal{F}(f)\|_{\mathbb{L}_2(\mathbb{R}^d)}^2 = \|f\|_{\mathbb{L}_2(\mathbb{R}^d)}^2$  for all images  $f \in \mathbb{L}_2(\mathbb{R}^d)$ . In standard wavelet theory there also exists such a theorem, but this is not applicable to our case, which requires some extra generalization of standard continuous wavelet theory.

### 1.1 Why Standard Wavelet Theory is not Applicable to our Application

In this subsection we first explain why standard wavelet theory, summarized in Theorem 1, can not be applied to the framework of orientation scores. Then we give a short summary (only as far as relevant for our purpose) of the results from a new wavelet theory which we developed in earlier work.

Let  $H$  be a Hilbert space, e.g. the space of images  $\mathbb{L}_2(\mathbb{R}^d)$ . Let  $\mathcal{U}$  be an irreducible unitary representation of the locally compact group  $G$ , with left-invariant Haar measure  $\mu_G$ . Recall the definitions in the preliminaries.

$$\text{Let } \psi \in H \text{ be admissible, i.e. } C_\psi = \int_G \frac{|(\mathcal{U}_g \psi, \psi)|^2}{(\psi, \psi)} d\mu_G(g) < \infty \quad (18)$$

then the wavelet transform  $\mathcal{W}_\psi : H \rightarrow \mathbb{L}_2(G)$  is defined by

$$(\mathcal{W}_\psi f)(g) = (\mathcal{U}_g \psi, f)_H. \quad (19)$$

The next theorem is well-known in mathematical physics [74], and is first formulated and proven in Grossmann et al. [44].

**Theorem 1 (The Continuous Wavelet Reconstruction Theorem)** *The wavelet transform  $\mathcal{W}_\psi$  given by (19) and constructed from an unitary irreducible representation  $\mathcal{U}$ , is a linear isometry (up to a constant) from the Hilbert space  $H$  onto a closed subspace  $\mathbb{C}_{K_\psi}^G$  of  $\mathbb{L}_2(G, d\mu)$ :*

$$\|\mathcal{W}_\psi[f]\|_{\mathbb{L}_2(G)}^2 = C_\psi \|f\|^2 \quad \text{for all } f \in H, \quad (20)$$

<sup>4</sup> Notice that this depends on the norm imposed on the set of images and on the norm imposed on the set of orientation scores.



The space  $\mathbb{C}_{K_\psi}^G$  is the unique functional Hilbert space with reproducing kernel

$$K_\psi(g, g') = \frac{1}{C_\psi} (\mathcal{U}_g \psi, \mathcal{U}_{g'} \psi).$$

The corresponding orthogonal projection  $\mathbb{P}_\psi : \mathbb{L}_2(G, d\mu) \rightarrow \mathbb{C}_{K_\psi}^G$  is given by

$$(\mathbb{P}_\psi \Phi)(g) = \int_G K_\psi(g, g') \Phi(g') d\mu_G(g') \quad \Phi \in \mathbb{L}_2(G, d\mu). \quad (21)$$

Furthermore,  $\mathcal{W}_\psi$  intertwines  $\mathcal{U}$  and the left regular representation  $\mathcal{L}$  —i.e.  $\mathcal{L}_g$  is given by  $\mathcal{L}_g(\Phi) = (h \mapsto \Phi(g^{-1}h))$  — on  $\mathbb{L}_2(G) : \mathcal{W}_\psi \mathcal{U}_g = \mathcal{L}_g \mathcal{W}_\psi$

*Remark 1* If  $\mathcal{U}$  is the left regular representation of  $G = \mathbb{R} \rtimes D(1) \rtimes O(1)$  (the group consisting of translations, dilations and polarity) onto  $H = \mathbb{L}_2(\mathbb{R})$  one obtains the more familiar framework of continuous wavelet theory in 1D signal processing.

*Remark 2* At this point one may just think of  $\mathbb{C}_{K_\psi}^G$  as being the range of  $\mathcal{W}_\psi$ , i.e

$$U \in \mathbb{C}_{K_\psi}^G \Leftrightarrow \exists f \in \mathbb{L}_2(\mathbb{R}^2) : U = \mathcal{W}_\psi f.$$

In a later stage of the lecture notes (ch:1.2) we will clarify more on reproducing kernel spaces and their notation.

*Remark 3* The proof in [44] is more technical than one expects at first sight. Roughly, the idea is to apply the generalized Schur's Lemma, recall Lemma 22, (but then for closed, possibly unbounded operators [15]) to the kernel operator that *a posteriori* equals  $\mathcal{W}_\psi^* \circ \mathcal{W}_\psi$ . Only *a posteriori* (i.e. after one has deduced that  $\mathcal{W}_\psi$  is indeed linear and bounded from  $\mathbb{L}_2(\mathbb{R}^d)$  into  $\mathbb{L}_2(G)$  so that  $\mathcal{W}_\psi^*$  is uniquely determined by the Riesz-representation theorem) one readily confirms (**verify this!**) via the result the usual Schur's lemma for bounded linear operators:

$$\forall_{g \in G} (\mathcal{W}_\psi^* \circ \mathcal{W}_\psi) \circ \mathcal{U}_g = \mathcal{W}_\psi^* \circ \mathcal{L}_g \circ \mathcal{W}_\psi = \mathcal{U}_g \circ (\mathcal{W}_\psi^* \circ \mathcal{W}_\psi) \Rightarrow \mathcal{W}_\psi^* \mathcal{W}_\psi = \lambda I, \text{ with } \lambda = C_\psi. \quad (22)$$

**Definition 8** In the setting of continuous wavelet transforms constructed from irreducible representations an **admissible wavelet**  $\psi \in \mathbb{L}_1(\mathbb{R}^d) \cap \mathbb{L}_2(\mathbb{R}^d)$  is a wavelet with  $C_\psi < \infty$ .

**Definition 9** Let  $SIM(2)$  denote the group of planar translations, rotations and scalings. Its group product is given by

$$(\mathbf{b}_1, \theta_1, a_1)(\mathbf{b}_2, \theta_2, a_2) = (\mathbf{b}_1 + a_1 R_{\theta_1} \mathbf{b}_2, \theta_1 + \theta_2 \text{ Mod } 2\pi, a_1 a_2).$$

**Corollary 1** (*standard continuous wavelet reconstruction schemes of 2D images*)

Let  $\psi \in \mathbb{L}_2(\mathbb{R}^2) \cap \mathbb{L}_1(\mathbb{R}^2)$  such that  $\hat{\psi}(\mathbf{0}) = 0$ , and consider

$$W_\psi^{SIM(2)} f(\mathbf{b}, e^{i\theta}, a) = (\mathcal{V}_{(\mathbf{b}, e^{i\theta}, a)} \psi, f)_{\mathbb{L}_2(\mathbb{R}^2)} = \frac{1}{a} \int_{\mathbb{R}^2} \overline{\psi(a^{-1} R_\theta^{-1}(\mathbf{x} - \mathbf{b}))} f(\mathbf{x}) d\mathbf{x}, \quad (23)$$

with irreducible representation  $\mathcal{V} : SIM(2) \rightarrow B(\mathbb{L}_2(\mathbb{R}^2))$  given by

$$\mathcal{V}_{(\mathbf{b}, e^{i\theta}, a)} \psi(\mathbf{x}) = \frac{1}{a} \psi(a^{-1} R_\theta^{-1}(\mathbf{x} - \mathbf{b})). \quad (24)$$

Then  $W_\psi^{SIM(2)}$  maps the space unitarily onto a closed (reproducing kernel) sub-space of  $\mathbb{L}_2(SIM(2))$  and we have

$$\forall_{f \in \mathbb{L}_2(\mathbb{R}^2)} : (W_\psi^{SIM(2)})^* \circ W_\psi^{SIM(2)} f = f \quad (25)$$

**Exercise 2 (Application of the Wavelet Reconstruction Theorem to  $G = SIM(2)$ )**

- a.) Show that the (up to scalar multiplications unique) left-invariant Haar-measure on the group of planar rotations, translation and scalings  $SIM(2) = \mathbb{R}^2 \rtimes (SO(2) \times \mathbb{R}^+)$  is given by

$$\int_{SIM(2)} \tilde{U}(g) dg = \int_{-\pi}^{\pi} \int_{\mathbb{R}^+} \int_{\mathbb{R}^2} \tilde{U}(\mathbf{b}, \theta, a) \frac{d\mathbf{b}}{a^2} \frac{da}{a} d\theta \quad (26)$$

for all Haar integrable functions  $\tilde{U} : SIM(2) \rightarrow \mathbb{C}$ . I.e. show that (10) holds for  $G = SIM(2)$ .

*hint: Study the Jacobian of the left-action  $g' = (\mathbf{b}, \theta, a) \mapsto qg' = (\mathbf{b}_0, \theta_0, a_0)(\mathbf{b}, \theta, a)$ .*

- b) Assume  $\psi \in L_2(\mathbb{R}^2) \cap L_1(\mathbb{R}^2)$ , which implies [66, Thm. 7.5] that  $\mathcal{F}\psi$  is a continuous function vanishing at infinity. Show that for all  $(\mathbf{b}, \theta, a) \in SIM(2)$  and all  $\boldsymbol{\omega} \in \mathbb{R}^d$  one has

$$(\mathcal{F} \mathcal{V}_{(\mathbf{b}, e^{i\theta}, a)} \psi)(\boldsymbol{\omega}) = a (\mathcal{F}\psi)(aR_{\theta}^{-1}\boldsymbol{\omega}) e^{-a(R_{\theta}^{-1}\boldsymbol{\omega} \cdot \mathbf{b}) i}. \quad (27)$$

- c) Assume  $\psi \in L_2(\mathbb{R}^2) \cap L_1(\mathbb{R}^2)$ , which implies [66, Thm. 7.5] that  $\mathcal{F}\psi$  is a continuous function vanishing at infinity. Show that if  $C_{\psi} = \frac{\|W_{\psi}^{SIM(2)} f\|_{L_2(SIM(2))}^2}{\|f\|_{L_2(\mathbb{R}^2)}^2}$  is finite for all  $0 \neq f \in L_2(\mathbb{R}^2)$  it equals

$$C_{\psi} = \int_{-\pi}^{\pi} \int_{\mathbb{R}^+} |\mathcal{F}\psi(aR_{\theta}^{-1}\boldsymbol{\omega})|^2 \frac{da}{a^3} d\theta.$$

for all  $\boldsymbol{\omega} \in \mathbb{R}^2$  with  $\boldsymbol{\omega} \neq \mathbf{0}$ .

*hint: Use the previous result and the Plancherel theorem.*

- d.) Assume  $\psi \in L_2(\mathbb{R}^2) \cap L_1(\mathbb{R}^2)$ , which implies [66, Thm. 7.5] that  $\mathcal{F}\psi$  is a continuous function vanishing at infinity. Then show that

$$C_{\psi} < \infty \Rightarrow \hat{\psi}(\mathbf{0}) = \int_{\mathbb{R}^2} \psi(\mathbf{x}) d\mathbf{x} = 0.$$

*hint: you may use the result of the previous exercise.*

- e.) Find an expression for the adjoint operator  $(W_{\psi}^{SIM(2)})^*$  such that

$$\forall U \in L_2(SIM(2)) \quad \forall f \in L_2(\mathbb{R}^2) \quad ((W_{\psi}^{SIM(2)})^* U, f)_{L_2(\mathbb{R}^2)} = (U, W_{\psi}^{SIM(2)} f)_{L_2(SIM(2))}.$$

- f.) Use the result from the previous exercise to rewrite (25) in an explicit reconstruction formula of the type  $f(\mathbf{x}) = \dots$

- g.) Finish the proof of Corollary 1, where you may use (without proof) the fact that  $W_{\psi}^{SIM(2)}$  is bounded.

*hint: follow the idea in Remark 2*

Of course, we would like to apply Theorem 1 to the wavelet transformation that maps an image to its orientation score, recall (3), since it would imply that reconstruction of an image from its orientation score is perfectly well-posed in the sense that (just like in Fourier transform) the quadratic norm is preserved. Unfortunately, the next lemma shows us that the group representation used to construct an orientation score is not reducible!

Therefore we cannot apply standard continuous wavelet theory to the orientation score transform. To account for this fundamental problem, in the subsequent subsections we aim to (re-)formulate continuous wavelet theory in such a way that irreducibility is neither a requirement nor replaced by a requirement.

**Lemma 2** *The left-regular action  $\mathcal{U}$  of the Euclidean motion group in  $L_2(\mathbb{R}^2)$ , given by (3), is a reducible representation.*

$$\begin{array}{|c|c|c|} \hline 0 & -\frac{1}{3} & 0 \\ \hline -\frac{1}{3} & 1 & 1 \\ \hline 0 & -\frac{1}{3} & 0 \\ \hline \end{array} + 
\begin{array}{|c|c|c|} \hline 0 & 1 & 0 \\ \hline -\frac{1}{3} & 1 & -\frac{1}{3} \\ \hline 0 & -\frac{1}{3} & 0 \\ \hline \end{array} + 
\begin{array}{|c|c|c|} \hline 0 & -\frac{1}{3} & 0 \\ \hline 1 & 1 & -\frac{1}{3} \\ \hline 0 & -\frac{1}{3} & 0 \\ \hline \end{array} + 
\begin{array}{|c|c|c|} \hline 0 & -\frac{1}{3} & 0 \\ \hline -\frac{1}{3} & 1 & -\frac{1}{3} \\ \hline 0 & 1 & 0 \\ \hline \end{array} = 
\begin{array}{|c|c|c|} \hline 0 & 0 & 0 \\ \hline 0 & 4 & 0 \\ \hline 0 & 0 & 0 \\ \hline \end{array}$$

**Fig. 5** Integrating the discrete orientation score  $U_f^4$  over its 4 discrete orientations (28), boils down to convolution with the discrete spike  $\delta$ .

**Proof:** Consider the subspace consisting of  $\mathbb{L}_2$ -functions whose Fourier transform have a support inside a given disk around the origin with radius, say  $\varrho > 0$ , i.e.  $\mathbb{L}_2^\varrho(\mathbb{R}^2) = \{f \in \mathbb{L}_2(\mathbb{R}^2) \mid \text{supp}(\mathcal{F}f) \subset B_{0,\varrho}\}$ , then this is a non-trivial vector space unequal  $\mathbb{L}_2(\mathbb{R}^2)$  which is invariant under  $\mathcal{U}$ , which directly follows by  $\mathcal{F}(\mathcal{U}_g\psi) = e^{i\omega \cdot \mathbf{b}} \mathcal{R}_{e^{i\theta}} \mathcal{F}\psi$ , for all  $\psi \in \mathbb{L}_2^\varrho(\mathbb{R}^2)$   $\square$ .

**Corollary 2** *Theorem 1 can not be applied to the transform between images and orientation scores that is given by (3).*

We could consider the similitude group  $SIM(2) = \mathbb{R}^2 \rtimes S^1 \times D(1)$  with representation  $\mathcal{V}$  given by (24), which is irreducible, for proof see [54]p.51-52. Recall that this was studied in Exercise 2. Indeed this brings us within the standard wavelet frameworks in 2D image analysis (in particular to 2D Gabor wavelets, [53], or Cauchy-wavelets [3]).

However, from a practical and efficiency point of view we do not want to consider multiple scales, but merge all scales in a single wavelet. This pertains to the so-called *Euclidean coherent states* from mathematical physics<sup>5</sup> [45].

Clearly, omitting the dilation group has serious consequences (as we have to capture all relevant scales up to the Nyquist frequency at once), however we get hope from the following introductory, finite sampling example, which shows us intuitively that integration over orientations can already be sufficient for sharp reconstruction.

**Example:** Suppose we construct a discrete orientation score with only 4 orientations, up, down left and right, constructed with the following discrete oriented wavelet  $\psi : \mathbb{Z} \times \mathbb{Z} \rightarrow \mathbb{R}$ , given by

$$\psi[x^1, x^2] = \begin{cases} 1 & \text{if } (x^1, x^2) \in \{(0, 0), (1, 0)\} \\ -1/3 & \text{if } (x^1, x^2) \in \{(0, 1), (0, -1), (-1, 0)\} \\ 0 & \text{else,} \end{cases}$$

see Figure 5. Then reconstruction of the original discrete image  $f : \mathbb{Z} \times \mathbb{Z} \rightarrow \mathbb{R}$  from its orientation score is done by integration over all directions.

$$f[x^1, x^2] = \frac{1}{4} \sum_{k=1}^4 U_f^4[x^1, x^2, e^{ik\pi/2}]. \quad (28)$$

## 1.2 Reproducing Kernel Spaces and Continuous Wavelet Transforms

Before we formulate the main theorem (Theorem 2) from which we can quantify the stability of the transformations between image and orientation score, we give some short explanation on reproducing kernel Hilbert spaces (also called ‘functional Hilbert spaces’, as they consist of true functions and not function classes), which is necessary to read and understand the theorem. The reader must keep in mind, that although the Lemmas below hold in a more general setting, we shall be concerned with the space of orientation scores of 2D images which means that we shall soon consider the following setting:

$$\begin{aligned} \text{Index set :} & \quad \mathbb{I} = SE(2), \\ \text{Reproducing kernel: } & K(g, h) = (\mathcal{U}_g\psi, \mathcal{U}_h\psi)_{\mathbb{L}_2(\mathbb{R}^2)}. \end{aligned} \quad (29)$$

<sup>5</sup> which are not to be confused with the more familiar Euclidean coherent states constructed from the irreducible representations of the Euclidean motion group onto  $\mathbb{L}_2(S^1)$ , cf. [2]p.219-220.

### 1.2.1 General Unitarity and Sampling Results on Reproducing Kernel Hilbert Spaces

A reproducing kernel Hilbert space is a Hilbert space consisting of complex valued functions on an index set  $\mathbb{I}$  on which the point evaluation  $\delta_{\mathbf{a}}$ , given by  $\delta_{\mathbf{a}}(f) = f(\mathbf{a})$  is a continuous linear functional for all  $\mathbf{a} \in \mathbb{I}$ . This means that  $\delta_{\mathbf{a}}(f_n) = f_n(\mathbf{a}) \rightarrow \delta_{\mathbf{a}}(f) = f(\mathbf{a})$  for every sequence  $\{f_n\}$  in  $H$  which converges to  $f$ ,  $f_n \rightarrow f$ . It is not difficult to show that a linear functional on a normed space is continuous if and only if it is bounded.

**Exercise 3** Prove the previous statement.

So  $\delta_{\mathbf{a}}$  is a continuous linear functional if and only if there exists a constant  $C_{\mathbf{a}}$  such that  $|f(\mathbf{a})| \leq C_{\mathbf{a}} \|f\|_H$ . For example, the spaces  $\mathbb{L}_2(\mathbb{R}^d)$  are *not* functional Hilbert spaces, but the well known first order Sobolev space  $\mathbb{H}_1(\mathbb{R})$  is such a functional Hilbert space.

If  $H$  is a functional Hilbert space, then  $\delta_{\mathbf{a}}$  is a continuous linear functional, so that by the Riesz representation theorem it has a Riesz representative  $K_{\mathbf{a}} \in H$  such that

$$f(\mathbf{a}) = \delta_{\mathbf{a}}(f) = (K_{\mathbf{a}}, f)_H,$$

for every  $\mathbf{a} \in \mathbb{I}$ . The function  $K : \mathbb{I} \times \mathbb{I} \rightarrow \mathbb{C}$  given by

$$K(\mathbf{a}, \mathbf{b}) = (K_{\mathbf{a}}, K_{\mathbf{b}})_H = K_{\mathbf{b}}(\mathbf{a})$$

is called reproducing kernel, because of its reproducing property. Therefore, ‘functional Hilbert spaces’ are also called ‘reproducing kernel Hilbert spaces’.

An important general observation is that the span  $\langle \{K_m \mid m \in \mathbb{I}\} \rangle$  must be dense in the reproducing kernel Hilbert space. Indeed if  $f \in H$  is orthogonal to all  $K_m$  one has  $f = 0$ .

#### Exercise 4 (Examples of reproducing kernel spaces)

a.) Show that the space of bandlimited 2D images (on a square  $[-L, L] \times [-L, L]$ )

$$\mathbb{L}_2^{BAND, L}(\mathbb{R}^2) := \{f \in \mathbb{L}_2(\mathbb{R}^2) \mid \text{supp}\{\mathcal{F}f\} \subset [-L, L] \times [-L, L]\}$$

is a reproducing kernel space and show that its reproducing kernel equals:

$$K_L(\mathbf{a}, \mathbf{x}') = 2\pi \mathcal{F}^{-1}[1_{[-L, L] \times [-L, L]}](\mathbf{a} - \mathbf{x}') = 4L^2 \text{sinc}(L(x - x')) \cdot \text{sinc}(L(y - y')),$$

with  $\mathbf{a} = (x, y)$ ,  $\mathbf{x}' = (x', y')$  and  $\text{sinc}(v) = \frac{\sin v}{v}$  for  $0 \neq v \in \mathbb{R}$ , and  $\text{sinc}(0) = 1$ .

b.) Let us consider  $L = \pi$  for simplicity in the following sampling theorem. Show that any  $f \in \mathbb{L}_2^{BAND, \pi}$  can be exactly reconstructed from its values on a discrete grid (by ‘sinc-interpolation’):

$$f(\mathbf{a}) = \int_{\mathbb{R}^2} f(\mathbf{x}') K_{\pi}(\mathbf{a}, \mathbf{x}') \, d\mathbf{x}' = \sum_{\mathbf{n} \in \mathbb{Z}^2} f(\mathbf{n}) \frac{K_{\pi}(\mathbf{a}, \mathbf{n})}{4\pi^2}.$$

(hint:  $f(\mathbf{n})$  equals the  $\mathbf{n}$ -th Fourier series coefficient of  $\mathcal{F}f|_{(-\pi, \pi) \times (-\pi, \pi)}$ .)

c.) Show that the space of disk-limited images  $\mathbb{L}_2^{\mathcal{D}}(\mathbb{R}^2)$ , recall (5), is a reproducing kernel Hilbert space, and show that its reproducing kernel equals

$$K(\mathbf{x}, \mathbf{x}') = \mathcal{F}^{-1}[1_{B_{0, \varrho}}](\mathbf{x} - \mathbf{x}') = J_1\left(\frac{\|\mathbf{x} - \mathbf{x}'\|}{\varrho}\right) \frac{\varrho}{\|\mathbf{x} - \mathbf{x}'\|}$$

d.) Derive the reproducing kernel of the first order Sobolev space  $\mathbb{H}_1(\mathbb{R})$  with inner product

$$(f, g)_{\mathbb{H}_1(\mathbb{R})} = (f, g)_{\mathbb{L}_2(\mathbb{R})} + (Df, Dg)_{\mathbb{L}_2(\mathbb{R})},$$

with generalized derivative  $D$ .

In general the reproducing kernel in a functional Hilbert space is a function of positive type on  $\mathbb{I}$ , i.e.

$$\sum_{i=1}^n \sum_{j=1}^n K(m_i, m_j) \bar{c}_i c_j \geq 0, \text{ for all } n \in \mathbb{N}, c_1, \dots, c_n \in \mathbb{C}, m_1, \dots, m_n \in \mathbb{I}.$$

Conversely, as Aronszajn pointed out in his paper, cf. [4], a function  $K$  of positive type on a set  $\mathbb{I}$  uniquely induces a reproducing kernel Hilbert space consisting of functions on  $\mathbb{I}$  with reproducing kernel  $K$ . Henceforward we shall be concerned with the following sort of functions of positive type

$$K(m_i, m_j) = (\phi_{m_i}, \phi_{m_j})_H,$$

where typically, we consider  $H = \mathbb{L}_2(\mathbb{R}^2)$  so that  $(\cdot, \cdot)_H$  denotes the  $\mathbb{L}_2$ -inner product.

**Definition 10** We denote this unique reproducing kernel Hilbert space consisting of functions on index set  $\mathbb{I}$  with reproducing kernel  $K$  by  $\mathbb{C}_K^{\mathbb{I}}$ .

Next we explain some basics on the formal norm on  $\mathbb{C}_K^{\mathbb{I}}$  and a sampling theorem. For further details, see [4, 57]. The span  $\langle \{K_m \mid m \in \mathbb{I}\} \rangle$  is an inner-product space with respect to the following inner product

$$\left( \sum_{i=1}^l \alpha^i K_{m_i}, \sum_{j=1}^n \beta^j K_{m_j} \right) := \sum_{i=1}^l \sum_{j=1}^n \bar{\alpha}^i \beta^j K(m_i, m_j).$$

By taking the completion of this inner product space we get the Hilbert-space  $\mathbb{C}_K^{\mathbb{I}}$ , carrying the norm:

$$\|\Phi\|_{\mathbb{C}_K^{\mathbb{I}}}^2 = \sup \left\{ \frac{\left| \sum_{j=1}^l \alpha^j \Phi(m_j) \right|^2}{\sum_{k,j=1}^l \bar{\alpha}^k \alpha^j K(m_k, m_j)} \mid l \in \mathbb{N}, \alpha_j \in \mathbb{C}, m_j \in \mathbb{I}, \sum_{k,j=1}^l \bar{\alpha}^k \alpha^j K(m_k, m_j) \neq 0 \right\}, \quad (30)$$

which is unfortunately rather intangible from the engineering point of view (due to its technical dual norm formulation). In our case of interest (29) we will derive a tangible description of these inner products.

**Lemma 3** *Let  $K$  be a function of positive type on  $\mathbb{I}$  and  $F$  a complex-valued function on  $\mathbb{I}$ . Then the function  $F$  belongs to  $\mathbb{C}_K^{\mathbb{I}}$  if and only if there exists a constant  $\gamma > 0$  such that*

$$\left| \sum_{j=1}^l \alpha^j \overline{F(m_j)} \right|^2 \leq \gamma \sum_{k,j=1}^l \bar{\alpha}^k \alpha^j K(m_k, m_j), \quad (31)$$

for all  $l \in \mathbb{N}$  and  $\alpha^j \in \mathbb{C}$ ,  $m_j \in \mathbb{I}$ ,  $1 \leq j \leq l$ .

**Proof:** See [57, Lemma 1.7, pp.31].

**Remark 4** From Lemma 3 it follows that the norm on  $\mathbb{C}_K^{\mathbb{I}}$  is given by (30) via dual norm construction.

**Lemma 4** *Let  $V = \{\phi_m \mid m \in \mathbb{I}\}$  be a subset of  $H$  such that its linear span is dense in  $H$ . Define the function  $K : \mathbb{I} \times \mathbb{I} \rightarrow \mathbb{C}$  by*

$$K(m, m') := (\phi_m, \phi_{m'})_H.$$

Then the transform  $\mathcal{W} : H \mapsto \mathbb{C}_K^{\mathbb{I}}$  defined by

$$(\mathcal{W}[f])(m) = (\phi_m, f)_H \quad (32)$$

is a unitary mapping, i.e.  $\|\mathcal{W}[f]\|_{\mathbb{C}_K^{\mathbb{I}}} = \|f\|_H$  for all  $f \in H$ .



**Proof** First we show that  $\mathcal{W}f \in \mathbb{C}_K^\mathbb{I}$  for any element  $f \in H = \overline{\langle V \rangle}$  and that  $\mathcal{W}$  is bounded (and therefore continuous). If  $f \in H$  then

$$\begin{aligned} \left| \sum_{j=1}^l \alpha_j \overline{(\mathcal{W}f)(m_j)} \right|^2 &= \left| \sum_{j=1}^l \alpha_j \overline{(\phi_{m_j}, f)_H} \right|^2 = \left| \left( \sum_{j=1}^l \alpha_j \phi_{m_j}, f \right)_H \right|^2 \\ &\leq \left\| \sum_{j=1}^l \alpha_j \phi_{m_j} \right\|_H^2 \|f\|_H^2 = \left( \sum_{k,j=1}^l \overline{\alpha_k} \alpha_j K(m_k, m_j) \right) \|f\|_H^2, \end{aligned}$$

for all  $l \in \mathbb{N}$ ,  $\alpha_1, \dots, \alpha_l \in \mathbb{C}$ , and  $m_1, \dots, m_l \in \mathbb{I}$ . So  $\mathcal{W}f \in \mathbb{C}_K^\mathbb{I}$  by Lemma 3 and  $\|\mathcal{W}f\|_{\mathbb{C}_K^\mathbb{I}}^2 \leq \|f\|_H^2$ , by (30). Next we prove that  $\mathcal{W}$  is an isometry. Because  $(\phi_m, \phi_{m'}) = K(m, m')$ ,  $\mathcal{W}$  maps a linear combination  $\sum_i \alpha_i \phi_{m_i}$  onto the linear combination  $\sum_i \alpha_i K(\cdot, m_i)$ . So  $\mathcal{W}(\langle V \rangle) = \{K(\cdot, m) | m \in \mathbb{I}\}$ . Moreover, it maps  $\langle V \rangle$  isometrically onto  $\{K(\cdot, m) | m \in \mathbb{I}\}$ , because

$$\begin{aligned} \left( \mathcal{W} \left( \sum_i \alpha_i \phi_{m_i} \right), \mathcal{W} \left( \sum_j \beta_j \phi_{m'_j} \right) \right)_{\mathbb{C}_K^\mathbb{I}} &= \left( \sum_i \alpha_i K(\cdot, m_i), \sum_j \beta_j K(\cdot, m'_j) \right)_{\mathbb{C}_K^\mathbb{I}} \\ &= \sum_{i,j} \overline{\alpha_i} \beta_j K(m_i, m'_j) = \sum_{i,j} \overline{\alpha_i} \beta_j (\phi_{m_i}, \phi_{m'_j})_H. \end{aligned}$$

Since  $\langle V \rangle$  is dense in  $\overline{\langle V \rangle}$  and  $\mathcal{W}$  is bounded on  $H = \overline{\langle V \rangle}$  it follows that  $\mathcal{W}$  is an isometry. Furthermore,  $\mathcal{W}[\langle V \rangle]$  is dense in  $\mathbb{C}_K^\mathbb{I}$ . So  $\mathcal{W}$  is also surjective and therefore unitary.  $\square$

Also, a sampling theorem comes for free on the reproducing kernels spaces, that is, again, as long as the span of  $\{\phi_m | m \in \mathbb{I}\}$  is dense in  $H$ .

**Lemma 5** *Let  $H$  be a separable Hilbert space, such that  $V = \{\phi_m | m \in \mathbb{I}\}$  is a frame in  $H$ . Let  $\{m_n\}_{n \in \mathbb{N}}$  be a sequence in  $\mathbb{I}$  such that  $\{\phi_{m_n} | n \in \mathbb{N}\}$  is an orthogonal basis in  $H$ . Set  $K(m, m') = (\phi_m, \phi_{m'})$ . Then*

$$f(m) = \sum_{n \in \mathbb{N}} f(m_n) \frac{K(m, m_n)}{K(m_n, m_n)},$$

for all  $m \in \mathbb{I}$  and  $f \in \mathbb{C}_K^\mathbb{I}$ . Moreover,

$$\|f\|^2 = \sum_{n \in \mathbb{N}} \frac{|f(m_n)|^2}{K(m_n, m_n)}, \text{ for all } f \in \mathbb{C}_K^\mathbb{I}.$$

**Proof** By Theorem 4, the corresponding map is unitary, and therefore the set  $\{K_{m_n} | n \in \mathbb{N}\}$  is an orthogonal basis for  $\mathbb{C}_K^\mathbb{I}$ . Let  $f \in \mathbb{C}_K^\mathbb{I}$ , then

$$f = \sum_{n \in \mathbb{N}} \beta^n K_{m_n} = \sum_{n \in \mathbb{N}} \frac{(K_{m_n}, f)_{\mathbb{C}_K^\mathbb{I}}}{\sqrt{K(m_n, m_n)}} \frac{K_{m_n}}{\sqrt{K(m_n, m_n)}} = \sum_{n \in \mathbb{N}} f(m_n) \frac{K_{m_n}}{K(m_n, m_n)}.$$

Therefore the second statement follows. For the first statement take the inner product with  $K_m$ .  $\square$

### 1.3 A Unitary Map from the Space of Images onto The Space of Orientation Scores

By applying Lemma 4 to the case

$$H = \mathbb{L}_2(\mathbb{R}^2), \mathbb{I} = \mathbb{R}^2 \rtimes \mathbb{S}^1 \equiv SE(2) = \mathbb{R}^2 \rtimes SO(2), \text{ and } V = \{\mathcal{U}_g \psi | g \in G\}, \quad (33)$$

which is dense in  $\mathbb{L}_2(\mathbb{R}^2)$  iff

$$0 < M_\psi(\omega) = (2\pi) \int_0^{2\pi} |\mathcal{F}(\psi)(\rho \cos \varphi, \rho \sin \varphi)|^2 d\varphi < \infty, \quad (34)$$

almost everywhere on  $\mathbb{R}^2$ , and by characterizing the inner product on the space  $\mathbb{C}_K^{G=\mathbb{R}^2 \rtimes S^1}$  we obtain:

**Theorem 2 (Unitarity Result for Orientation Score Transform )**

Let  $\psi \in \mathbb{L}_1(\mathbb{R}^2) \cap \mathbb{L}_2(\mathbb{R}^2)$  be chosen such that  $M_\psi > 0$ . The space of orientation scores equals the Reproducing Kernel Hilbert Space  $\mathbb{C}_K^{\mathbb{R}^2 \rtimes S^1}$ . The inner product on  $\mathbb{C}_K^{\mathbb{R}^2 \rtimes S^1}$  is characterized by

$$(U, V)_{M_\psi} = (T_{M_\psi}[U], T_{M_\psi}[V])_{\mathbb{L}_2(\mathbb{R}^2 \rtimes S^1)}$$

where

$$[T_{M_\psi}[U]](\mathbf{b}, \theta) = \mathcal{F}^{-1} \left[ \omega \mapsto |(2\pi)^{\frac{d}{2}} M_\psi(\omega)|^{-\frac{1}{2}} \mathcal{F}[U(\cdot, e^{i\theta})](\omega) \right] (\mathbf{b}), \quad (35)$$

characterized by  $M_\psi$  given by (34).

The transform  $\mathcal{W}_\psi : \mathbb{L}_2(\mathbb{R}^2) \rightarrow \mathbb{C}_K^{\mathbb{R}^2 \rtimes S^1}$  between image  $f$  and orientation score  $\mathcal{W}_\psi f$  given by (3) is unitary and

$$\begin{aligned} \|f\|_{\mathbb{L}_2(\mathbb{R}^2)}^2 &= \|\mathcal{W}_\psi f\|_{M_\psi}^2 = (\mathcal{W}_\psi f, \mathcal{W}_\psi f)_{M_\psi}, \\ f &= \mathcal{W}_\psi^* \mathcal{W}_\psi[f] = \mathcal{F}^{-1} \left[ \omega \mapsto \int_0^{2\pi} \mathcal{F}[\mathcal{W}_\psi f(\cdot, e^{i\theta})](\omega) \mathcal{F}[\mathcal{R}_{e^{i\theta}\psi}](\omega) d\theta M_\psi^{-1}(\omega) \right]. \end{aligned} \quad (36)$$

**Proof** First of all we note that each fixed  $\theta$ -layer in the orientation score (recall (1)), i.e. the function  $\mathcal{W}_\psi f(\cdot, \theta)$  can be written as a convolution with the image  $f$ :

$$(\mathcal{W}_\psi f)(\mathbf{b}, \theta) = (\bar{\psi}_{\theta+\pi} * f)(\mathbf{b}) \text{ for all } \mathbf{b} \in \mathbb{R}^2,$$

where we use short notation for the rotated kernel:  $\psi_\theta(\mathbf{x}) = \psi(R_\theta^{-1}\mathbf{x})$ . Note also that  $\psi_{\theta+\pi}(\mathbf{x}) = \psi(-R_\theta^{-1}\mathbf{x})$ . Now, recall from part I that a convolution in the spatial domain corresponds to a direct product in the Fourier domain:  $(\mathcal{F}(f_1 * f_2))(\omega) = (2\pi)^{\frac{d}{2}} \mathcal{F}f_1(\omega) \mathcal{F}f_2(\omega)$ . Here we have  $d = 2$ , so we rewrite

$$(2\pi)^{-1} (\mathcal{F}\mathcal{W}_\psi f(\cdot, \theta))(\omega) = \mathcal{F}(\bar{\psi}_{\theta+\pi})(\omega) (\mathcal{F}f)(\omega) \quad (37)$$

By setting the special case (33) in Lemma 4 we know that  $\mathcal{W}_\psi$  maps  $\mathbb{L}_2(\mathbb{R}^2)$  unitarily onto  $\mathbb{C}_K^{SE(2)}$ . Now by compactness of  $SO(2)$  and Fubini we can switch orders of integration and obtain by Plancherel theorem for Fourier transform  $\mathcal{F} : \mathbb{L}_2(\mathbb{R}^2) \rightarrow \mathbb{L}_2(\mathbb{R}^2)$  that:

$$\begin{aligned} \|\mathcal{W}_\psi f\|_{\mathbb{C}_K^{SE(2)}}^2 &= \|f\|_{\mathbb{L}_2(\mathbb{R}^2)}^2 = \|\mathcal{F}f\|_{\mathbb{L}_2(\mathbb{R}^2)}^2 = \int_{\mathbb{R}^2} |\mathcal{F}f(\omega)|^2 \frac{M_\psi(\omega)}{M_\psi(\omega)} d\omega \\ &= 2\pi \int_{-\pi}^{\pi} \int_{\mathbb{R}^2} |\mathcal{F}f(\omega) \mathcal{F}\bar{\psi}_{\theta+\pi}(\omega)|^2 d\theta (M_\psi(\omega))^{-1} d\omega \\ &\stackrel{(37)}{=} \int_{-\pi}^{\pi} \int_{\mathbb{R}^2} \left| \mathcal{F}\mathcal{W}_\psi f(\omega, e^{i\theta}) (2\pi M_\psi(\omega))^{-\frac{1}{2}} \right|^2 d\omega d\theta \\ &\stackrel{(35)}{=} \int_{-\pi}^{\pi} \int_{\mathbb{R}^2} |\mathcal{F}T_{M_\psi}[\mathcal{W}_\psi f](\omega, e^{i\theta})|^2 d\omega d\theta \\ &= \int_{-\pi}^{\pi} \int_{\mathbb{R}^2} |T_{M_\psi}[\mathcal{W}_\psi f](\mathbf{b}, e^{i\theta})|^2 d\mathbf{b} d\theta \\ &= \|\mathcal{W}_\psi f\|_{M_\psi}^2, \end{aligned} \quad (38)$$

for all  $f \in \mathbb{L}_2(\mathbb{R}^d)$ . For  $U = \mathcal{W}_\psi f$  one indeed has a finite norm  $\|U\|_{M_\psi}^2 < \infty$  and all above integrals in (38) converge<sup>6</sup>.  $\square$

**Consequences and Remarks:**

<sup>6</sup> In the general setting of Theorem 2 the reproducing kernel norm equals the  $M_\psi$ -norm, but it is not equivalent to the  $\mathbb{L}_2(\mathbb{R}^2 \rtimes S^1)$ -norm (since for  $\psi \in \mathbb{L}_1(\mathbb{R}^2)$  function  $M_\psi$  is a continuous function vanishing at infinity). This is in contrast to the setting of Theorem 1 where  $\mathcal{U}$  is assumed to be an unitary irreducible representation and where the reproducing kernel norm was in fact the  $\mathbb{L}_2$ -norm. Recall from Lemma 2 that the representation  $\mathcal{U}$  used for the orientation score transform (3) is reducible.

1. This theorem easily generalizes to  $d$  dimensional images, i.e.  $f \in \mathbb{L}_2(\mathbb{R}^d)$ ,  $d = 2, 3, \dots$ . The only thing that changes is that integration now takes place over  $SO(d)$  and the function  $M_\psi$  becomes

$$M_\psi(\omega) = (2\pi)^{d/2} \int_{SO(d)} |\mathcal{F}(\mathcal{R}_t \psi)(\omega)|^2 d\mu_T(t), \quad (39)$$

where  $d\mu_T(t)$  is the normalized Haar-measure of  $SO(d)$ , which is the Fourier transform of

$$\tilde{\psi}(\mathbf{x}) = \int_{SO(d)} (\overline{\mathcal{R}_t \tilde{\psi}} * \mathcal{R}_t \psi)(\mathbf{x}) d\mu_T(t).$$

It can be shown that if  $\psi \in \mathbb{L}_1(\mathbb{R}^2)$ , then  $M_\psi$  and  $\tilde{\psi}$  are continuous functions in  $\mathbb{L}_1(\mathbb{R})$  and thereby vanishing at infinity. As a result(!) the ideal case  $M_\psi = (2\pi)^{d/2}$  (in which case we would have  $\mathbb{H}_\psi = \mathbb{L}_2(\mathbb{R}^d \rtimes SO(d))$ ) and thereby (quadratic norm preservation between image and orientation score) cannot be obtained *unless* one uses a Gelfand triple structure (just like Fourier transform) constructed by means of the Laplace operator<sup>7</sup>, for details see Appendix A.

2. Theorem 2 easily generalizes to the discrete orientation group, i.e.  $G = \mathbb{T}_N \rtimes \mathbb{R}^2$ , where

$$\mathbb{T}_N = \{e^{ik\Delta\theta} \mid k \in \{0, 1, \dots, N-1\}, \Delta = \frac{2\pi}{N}\}, \text{ for } N \in \mathbb{N}, \quad (40)$$

by replacing integrations by discrete summation. Notice that the discrete orientation score  $U_f^N(\mathbf{b}, e^{ik\Delta\theta})$  of an image  $f \in \mathbb{L}_2(\mathbb{R}^2)$  is given by

$$U_f^N(\mathbf{b}, e^{ik\Delta\theta}) = (\mathcal{T}_{\mathbf{b}} \mathcal{R}_{e^{ik\Delta\theta}} \psi, f)_{\mathbb{L}_2(\mathbb{R}^2)}, \quad k \in \{0, 1, \dots, N-1\}, \Delta\theta = \frac{2\pi}{N}.$$

and the discrete version of the function  $M_\psi$  is  $M_\psi^d(\omega) = \frac{2\pi}{N} \sum_{k=0}^{N-1} |\mathcal{F}(\mathcal{R}_{e^{ik\Delta\theta}} \psi)(\omega)|^2$ .

3. The function  $M_\psi$  completely determines the stability of the forward and backward transformation. In practice (due to sampling) we work with ball-limited images (5). If we restrict the wavelet transformation to the space of ball-limited images  $\mathbb{L}_2^g(\mathbb{R}^2)$ , then we can define a condition number (with respect to quadratic norms on the space of images and the space of orientation scores), [18]. This condition number tends to 1 when  $M_\psi$  tends to a constant function on the relevant part of the spectrum say  $1_{B_{\mathbf{0}, \varrho}}$ . We will call wavelets with the property that  $M_\psi|_{B_{\mathbf{0}, \varrho}} \approx 1$  **proper wavelets** (a formal definition soon follows in Definition A) as they guarantee a stable reconstruction. For these type of wavelets we could as well use the approximative reconstruction formula<sup>8</sup>

$$f \approx \tilde{\psi} * f = \mathcal{F}^{-1} \left[ \omega \mapsto \frac{1}{2\pi} \int_0^{2\pi} \mathcal{F}[\mathcal{W}_\psi f(\cdot, e^{i\theta})](\omega) \mathcal{F}[\mathcal{R}_{e^{i\theta}} \psi](\omega) d\theta \right]. \quad (41)$$

4. In Eq. (33) and (34) and in the above theorem, one could also restrict one-self to ball-limited images and ball-limited wavelets from the beginning, so that all integrals in (38) take only place on  $B_{\mathbf{0}, \varrho}$  and so that the spatial parts of the space  $\mathbb{H}_\psi$  are ball-limited. This simplifies, but is also a little bit inconvenient as  $\psi \in \mathbb{L}_1(\mathbb{R}^2) \cap \mathbb{L}_2^g(\mathbb{R}^2)$  implies  $\mathcal{F}\psi(\omega)$  vanishes continuously towards the boundary  $\rho = \|\omega\| \rightarrow \varrho$ , which would not match our definition of proper wavelets (cf. Definition A below).

<sup>7</sup> This commutes with the left regular actions  $\mathcal{U}_g$  for all  $g \in \mathbb{R}^d \rtimes SO(d)$ .

<sup>8</sup> We stress that even if  $M_\psi \neq 1$  stability is still manifest. The only requirement on  $M_\psi$  is that it remains overall finite and non-vanishing. Recall that in general one has to use (36) for exact reconstruction.

#### 1.4 Quantification Stability of the Transform between Images and Orientation Scores

In this section we will formally quantify stability of the transforms between images orientation scores. There we will also include the cases where approximate reconstruction is performed by integration over angles only. Furthermore, from the engineering point of view imposing  $\mathbb{L}_2$ -norms on domain and range (for condition numbers) seems to be a more fair way of quantifying stability (rather than imposing a kernel dependent reproducing kernel norm on the space of orientation scores). We first provide some preliminary definitions.

**Definition 11 (The condition number)** Let  $(V, \|\cdot\|_V)$  and  $(W, \|\cdot\|_W)$  be two normed vector spaces. Let  $A : V \rightarrow W$  be an invertible linear map. Then

$$\text{cond}(A) := \|A\| \|A^{-1}\| := \sup_{\mathbf{o} \neq \mathbf{v} \in V} \frac{\|Av\|_W}{\|v\|_V} \sup_{\mathbf{o} \neq \mathbf{w} \in W} \frac{\|A^{-1}w\|_V}{\|w\|_W}.$$

If  $A$  is injective (but not surjective) then we define

$$\text{cond}(A) := \sup_{\mathbf{o} \neq \mathbf{v} \in V} \frac{\|Av\|_W}{\|v\|_V} \sup_{\mathbf{o} \neq \mathbf{v} \in V} \frac{\|v\|_V}{\|Av\|_W}.$$

**Definition 12 (The coupled space  $\mathbb{R}^d \rtimes S^{d-1}$  of positions and orientations,  $d \in \{2, 3\}$ ).** Let  $\mathbf{a} \in S^{d-1}$  denote an a priori reference axis.

$$\begin{aligned} \text{For } d = 2, \text{ our default is } \mathbf{a} &= (1, 0)^T. \\ \text{For } d = 3, \text{ our default is } \mathbf{a} &= (0, 0, 1)^T. \end{aligned} \tag{42}$$

Let us denote the action of the rotation-translation group  $SE(d) = \mathbb{R}^d \rtimes SO(d)$  onto set  $\mathbb{R}^d \times S^{d-1}$  by

$$g \odot (\mathbf{x}, \mathbf{n}) = (\mathbf{b}, R) \odot (\mathbf{x}, \mathbf{n}) := (R\mathbf{x} + \mathbf{b}, R\mathbf{n}).$$

Then two rotations and translations  $g_1$  and  $g_2$  are called equivalent if

$$g_1 \sim g_2 \Leftrightarrow g_1 \odot (\mathbf{0}, \mathbf{a}) = g_2 \odot (\mathbf{0}, \mathbf{a}). \tag{43}$$

This boils down to the following partition of equivalence classes (left-cosets) in  $SE(d)$ :

$$g_1 \sim g_2 \Leftrightarrow g_1^{-1} g_2 \in H \tag{44}$$

where  $H := \{\mathbf{0}\} \times \text{Stab}\{\mathbf{a}\} \equiv \{\mathbf{0}\} \times SO(d-1)$ . This partition of equivalence classes is denoted by<sup>9</sup>

$$\mathbb{R}^d \rtimes S^{d-1} := SE(d)/H \equiv SE(d)/(\{\mathbf{0}\} \times SO(d-1)). \tag{45}$$

Similar to  $S^{d-1} = SO(d)/SO(d-1)$  we denote the elements of  $\mathbb{R}^d \rtimes S^{d-1}$  by  $(\mathbf{x}, \mathbf{n})$ . Keep in mind that every element  $(\mathbf{x}, \mathbf{n})$  is a class of roto-translations  $\{(\mathbf{x}, R\mathbf{n}) \mid \text{with } R\mathbf{n} \in SO(d) \text{ s.t. } R\mathbf{n}\mathbf{a} = \mathbf{n}\}$ .

**Exercise 5** Verify that the equivalence relation in (43), is the same as the equivalence relation in (44).

**Definition 13 (proper wavelets)** Let us set a priori bounds<sup>10</sup>  $\delta, M > 0$ ,  $1 \gg \varepsilon > 0$ , (in practice we choose  $\delta = \frac{1}{8}$  and  $M = 1.1$  and  $\varepsilon = 0.01$ ).

Then, a wavelet  $\psi \in \mathbb{L}_2(\mathbb{R}^d)$  is called a proper wavelet if

- 1.)  $\psi \in \mathbb{L}_1(\mathbb{R}^d)$ ,
  - 2.)  $\psi(R^{-1}\mathbf{x}) = \psi(\mathbf{x})$  for all  $R \in \text{Stab}(\mathbf{a}) \subset SO(d)$ ,
  - 3.)  $\forall \boldsymbol{\omega} \in B_{\mathbf{0}, \varepsilon} : \delta \leq M_\psi(\boldsymbol{\omega}) := \int_{S^{d-1}} |\mathcal{F}\psi(R_{\mathbf{n}}^{-1}\boldsymbol{\omega})|^2 d\sigma(\mathbf{n}) \leq M$ .
- (46)

<sup>9</sup> Formally speaking  $S^{d-1}$  is not a group, and the use of the semi-direct product symbol in the left-hand side of (45) is questionable, in contrast to its use in the righthand side. Nevertheless, the notation is convenient and the reader must keep in mind (45) is just our definition.

<sup>10</sup> In practice we choose the default values  $\delta = \frac{1}{8}$  and  $M = 1.1$  and  $\varepsilon = 0.01$  and note that it is actually the ratio  $\frac{M}{\delta}$  that determines the condition number. It is just that it is a convenient choice to set the upper bound close to 1.

If moreover, one has

$$4.) \exists_{\frac{1}{2}\varrho < \varrho_0 < \varrho} \forall_{\boldsymbol{\omega} \in B_{\mathbf{0}, \varrho_0}} : N_{\psi}(\boldsymbol{\omega}) := \int_{S^{d-1}} \mathcal{F}\psi(R_{\mathbf{n}}^{-1}\boldsymbol{\omega}) d\sigma(\mathbf{n}) \in [1 - \varepsilon, 1 + \varepsilon],$$

then we speak of a **proper wavelet with fast reconstruction property**, cf. (47).

*Remark 5* The 1st condition ensures that its Fourier transform is continuous, [66, Thm. 7.5]. The 2nd condition allow for an appropriate definition of an *orientation score* rather than a *rotation score*, see the next definition. The 3rd condition ensures invertibility and stability of the (inverse) orientation score transform. The 4th condition, allows us to use of the approximate reconstruction by integration over angles only:

$$\boxed{f(\mathbf{x}) \approx \int_{S^{d-1}} \mathcal{W}_{\psi} f(\mathbf{x}, \mathbf{n}) d\sigma(\mathbf{n}).} \quad (47)$$

### Exercise 6

a. Show that the 2nd condition in (46) implies that

$$\forall_{R \in SO(d)} \forall_{\boldsymbol{\omega} \in \mathbb{R}^d} : \hat{\psi}(R\boldsymbol{\omega}) = \hat{\psi}(\boldsymbol{\omega}),$$

where  $\hat{\psi} = \mathcal{F}\psi$ .

b. Show that the 2nd condition in (46) indeed implies that the choice of  $R_{\mathbf{n}} \in SO(d)$  such that  $R_{\mathbf{n}}\mathbf{a} = \mathbf{n}$  does not affect the defined continuous functions  $M_{\psi} : \mathbb{R}^d \rightarrow \mathbb{R}^+$ ,  $N_{\psi} : \mathbb{R}^d \rightarrow \mathbb{R}^+$ .

*Remark 6* Formally we have by (39), the fact that  $\text{Stab}_{SO(d)}(\mathbf{a}) \equiv SO(d-1)$ , and the symmetry requirement that  $M_{\psi}(\boldsymbol{\omega}) = (2\pi)^{\frac{d}{2}} \mu(SO(d-1)) \int_{S^{d-1}} |\hat{\psi}(R_{\mathbf{n}}^T \boldsymbol{\omega})|^2 d\sigma(\mathbf{n})$ . Nevertheless in the 3rd item we omit the scalar multiplication before the integral in (46) to keep thing simple. Note to this end that a constant scalar multiplication of the transform  $W_{\psi}$  and/or  $M_{\psi}$  is relevant both for stability and condition numbers.

**Definition 14** For proper wavelets  $\psi \in \mathbb{L}_2(\mathbb{R}^d) \cap \mathbb{L}_1(\mathbb{R}^d)$ , we constrain the domain of our wavelet transform to ball-limited images  $\mathbb{L}_2^{\varrho}(\mathbb{R}^d)$ , and we define the orientation score transform

$$\widetilde{\mathcal{W}}_{\psi} : \mathbb{L}_2^{\varrho}(\mathbb{R}^d) \rightarrow \mathbb{L}_2(\mathbb{R}^d \rtimes S^{d-1})$$

in a well-posed manner by

$$\widetilde{\mathcal{W}}_{\psi} f(\mathbf{b}, \mathbf{n}) = (\mathcal{U}_{(\mathbf{b}, R_{\mathbf{n}})} \psi, f)_{\mathbb{L}_2(\mathbb{R}^d)} \quad (48)$$

for all ball-limited images  $f \in \mathbb{L}_2^{\varrho}(\mathbb{R}^d)$ , where the rotated and translated wavelet is given by

$$\mathcal{U}_{(\mathbf{b}, R_{\mathbf{n}})} \psi(\mathbf{x}) = \psi(R_{\mathbf{n}}^{-1}(\mathbf{x} - \mathbf{b})),$$

and where  $R_{\mathbf{n}} \in SO(d)$  denotes *any* rotation that maps reference axis  $\mathbf{a}$  onto  $\mathbf{n}$ .

**Definition 15** Let  $\psi \in \mathbb{L}_2(\mathbb{R}^d) \cap \mathbb{L}_1(\mathbb{R}^d)$  be a proper wavelet (which is axially symmetric around  $\mathbf{a}$ ). Let us denote the concatenation of the orientation score transform and approximative reconstruction by integration over  $S^{d-1}$  only, by operator  $A_{\psi} : \mathbb{L}_2(\mathbb{R}^d) \rightarrow \mathbb{L}_2(\mathbb{R}^d)$  be given by

$$(A_{\psi} f)(\mathbf{x}) = \int_{S^{d-1}} \mathcal{W}_{\psi} f(\mathbf{x}, \mathbf{n}) d\sigma(\mathbf{n}).$$



**Theorem 3 (Stability of Orientation Score Transform)**

Let  $\psi \in \mathbb{L}_2^\varrho(\mathbb{R}^d)$  be a proper (so axially symmetric) wavelet. Then the condition number of the orientation score transform mapping

$$\widetilde{\mathcal{W}}_\psi : \mathbb{L}_2^\varrho(\mathbb{R}^d) \rightarrow \mathbb{L}_2(\mathbb{R}^d \rtimes S^{d-1})$$

equals

$$(\text{cond}(\widetilde{\mathcal{W}}_\psi))^2 = \|M_\psi\|_{\mathbb{L}_\infty(B_{\mathbf{0},\varrho})} \cdot \|M_\psi^{-1}\|_{\mathbb{L}_\infty(B_{\mathbf{0},\varrho})}.$$

where  $B_{\mathbf{0},\varrho} = \{\boldsymbol{\omega} \in \mathbb{R}^d \mid \|\boldsymbol{\omega}\| \leq \varrho\}$  denotes the ball in the frequency domain with radius  $\varrho > 0$ . The condition number  $\text{cond}(\mathcal{W}_\psi)$  of  $\mathcal{W}_\psi : \mathbb{L}_2^\varrho(\mathbb{R}^d) \rightarrow \mathbb{C}_K^{SE(d)}$  equals 1. The condition number of the orientation score transform concatenated with reconstruction by integration over  $S^{d-1}$  only equals:

$$\text{cond}(A_\psi) = \|N_\psi\|_{\mathbb{L}_\infty(B_{\mathbf{0},\varrho})} \cdot \|N_\psi^{-1}\|_{\mathbb{L}_\infty(B_{\mathbf{0},\varrho})}.$$

**Exercise 7** Verify that the 2nd condition in (46) is both sufficient and necessary for a well-posed definition of  $\widetilde{\mathcal{W}}_\psi f : \mathbb{R}^d \rtimes S^{d-1} \rightarrow \mathbb{C}$  for all ball-limited (grayscale) images  $f \in \mathbb{L}_2^\varrho(\mathbb{R}^d)$ .

**Exercise 8 (Proof of Theorem 3)**

- a.) Show that for any multiplier operator  $\mathcal{M}_m : \mathbb{L}_2(B_{\mathbf{0},\varrho}) \rightarrow \mathbb{L}_2(B_{\mathbf{0},\varrho})$ , given by  $\mathcal{M}_m f = m f$  with a continuous multiplier  $m : B_{\mathbf{0},\varrho} \rightarrow \mathbb{R}^+$ , the operator norm  $\|\mathcal{M}_m\|$  equals the maximum value that  $m$  attains on compact set  $B_{\mathbf{0},\varrho}$ .
- b.) Let  $\psi \in \mathbb{L}_2^\varrho(\mathbb{R}^2)$  be a proper wavelet. Show that for all  $f \in \mathbb{L}_2^\varrho(\mathbb{R}^2)$  one has

$$\|\widetilde{\mathcal{W}}_\psi f\|_{\mathbb{L}_2(\mathbb{R}^2 \rtimes S^1)}^2 = (2\pi)^2 \int_{\mathbb{R}^2} M_\psi(\boldsymbol{\omega}) |(\mathcal{F}f)(\boldsymbol{\omega})|^2 d\boldsymbol{\omega} < \infty$$

$$\text{with } M_\psi(\boldsymbol{\omega}) = \int_{-\pi}^{\pi} |\mathcal{F}\psi(R_\theta^{-1}\boldsymbol{\omega})|^2 d\theta.$$

- c.) Provide a detailed proof of the above theorem for  $d = 2$ .
- d.) Provide a detailed proof of the above theorem for  $d = 3$ .

**Remark 7 (storing the lowest frequencies separately)** In continuous wavelet theory it is common to separately store very low frequency components separately (as they represent average value and very global variations which appear at scales much larger than the elongated structures of interest in the image), see e.g. [70, 56]. This yields a vector valued transform  $f \mapsto \underline{W}_\psi f$ , with a vector valued wavelet

$$\underline{\psi} = (\psi_0, \psi_1)^T \text{ with } \hat{\psi}_0 = \hat{G}_{s_\rho} \hat{\psi}, \quad \hat{\psi}_1 = (1 - \hat{G}_{s_\rho}) \hat{\psi}, \quad (49)$$

with  $\hat{G}_{s_\rho}(\boldsymbol{\omega}) = e^{-s_\rho \|\boldsymbol{\omega}\|^2}$ ,  $s_\rho > 0$ , whose stability can be analyzed in a similar way as in the above theorem. For details see Appendix B.

### 1.5 Working with a Finite Number of Orientations is Simple to include: Proper Wavelet Sets

Instead of working on  $SE(d)$  one may choose to work on sub-groups that use only a finite number of orientations. For  $SE(2) = \mathbb{R}^2 \rtimes S^1$ , one can work with  $SE(2, N_o) = \{(\mathbf{x}, \theta) \in SE(2) \mid \theta = \theta_k = \frac{k}{N_o} 2\pi\}$  via equidistant sampling while identifying  $e^{i\theta} \leftrightarrow \theta \bmod 2\pi$ :

$$\theta_k = \frac{k}{N_o} 2\pi, \text{ for } k = 0, \dots, N_o - 1 \in \mathbb{N}.$$

For  $SE(3)$  (where the subgroup property is much more restrictive, see the exercise below) one may consider, only those rotations that map the vertices of the icosahedron onto each other. Not much changes to the theory so far, as one just replaces the integrals over  $S^{d-1}$  by summations. Even for  $d = 3$  one may drop the formal group constraint (as it is not crucial for reconstruction and stability) and work with orientations that arise by tessellations of the icosahedron [18] while using (spherical Harmonic) interpolation [48].

It is worth noting that a very interesting formal relation with inverse Fourier Transform on discrete subgroups on  $SE(d)$ , cf. [42], similar to the full continuous setting [24, App.A], which we pursue in the next section, only applies to the cases where discrete subgroups of  $SO(d)$  are used. Despite that representation theory of *semi-discrete* subgroups of  $SE(d)$  is mathematically interesting, we do not need it in our framework.

**Exercise 9 (Limited discrete subgroups of  $SO(3)$  and semi-discrete Subgroups of  $SE(3)$ )**

a.) Show that on a *convex* regular solid in  $\mathbb{R}^3$  with  $n$ -gon faces (so that we have  $n$ -points per face) one has

$$2\pi - r(n-2)\pi/n > 0,$$

where  $r$  is the amount of faces meeting at every vertex.

*hint: the above expression is known as ‘the angular defect’<sup>11</sup>*

b.) Show that the largest platonic solid is the icosahedron with  $V = 12$  vertices,  $F = 20$  faces and  $E = V + F - 2 = 30$  edges.

c.) Determine the subgroup  $SE(3, N_R) = \mathbb{R}^3 \rtimes SO(3, N_R)$ , with  $SO(3, N_R)$  denoting the finite group of  $N_R = 60$  rotations that map the vertices of the icosahedron onto itself.

Let  $\{\mathbf{n}_i\}_{i=1}^{N_o}$  be an almost uniform sampling on  $S^{d-1}$ . For  $d = 3$  such almost uniform sampling can be computed using:

- an *electrostatic repulsion model*, where a given number  $N_o$  of charged particles are placed on a sphere such that a cost (reflecting the total amount of magnitudes of electrostatic repulsion forces) is minimized, see for example [14].
- a higher order tessellation of the icosahedron.

Assume we have a number  $N_o$  of orientations  $\mathcal{V} = \{\mathbf{n}_1, \mathbf{n}_2, \dots, \mathbf{n}_{N_o}\} \subset S^{d-1}$ , and define the discrete invertible orientation score  $\mathcal{W}_\psi^d[f] : \mathbb{R}^d \times \mathcal{V} \rightarrow \mathbb{C}$  by the correlations

$$(\mathcal{W}_\psi^d[f])(\mathbf{x}, \mathbf{n}_i) = (\overline{\psi_{\mathbf{n}_i}} \star f)(\mathbf{x}) = \int_{\mathbb{R}^d} \overline{\psi_{\mathbf{n}_i}(\mathbf{y} - \mathbf{x})} f(\mathbf{y}) d\mathbf{y}. \quad (50)$$

The exact reconstruction formula is in the discrete setting given by

$$f(\mathbf{x}) = ((\mathcal{W}_\psi^d)^{-1}[\mathcal{W}_\psi^d[f]])(\mathbf{x}) = \mathcal{F}^{-1} \left[ (M_\psi^d)^{-1} \mathcal{F} \left[ \tilde{\mathbf{x}} \rightarrow \sum_{i=1}^{N_o} (\check{\psi}_{\mathbf{n}_i} \star \mathcal{W}_\psi^d[f])(\cdot, \mathbf{n}_i) (\tilde{\mathbf{x}}) \Delta_i \right] \right] (\mathbf{x}), \quad (51)$$

with  $\Delta_i$  the discrete spherical area measure which for reasonably uniform spherical sampling can be approximated by  $\Delta_i \approx \frac{\mu(S^{d-1})}{N_o}$  (otherwise one could use more accurate approximations [27, Eq.83]), and

$$M_\psi^d(\omega) = \sum_{i=1}^{N_o} \left| \hat{\psi}_{\mathbf{n}_i}(\omega) \right|^2 \Delta_i. \quad (52)$$

Again, an exact reconstruction is possible iff  $0 < \delta \leq M_\psi^d(\omega) \leq M < \infty$  and we have  $\mathbb{L}_2$ -norm preservation for our transform between image and orientation score when  $M_\psi^d = 1$ . Again, for the wavelets for which

$$N_\psi^d = \sum_{i=1}^{N_o} \hat{\psi}_{\mathbf{n}_i}(\omega) \Delta_i \approx 1, \quad (53)$$

the reconstruction can be simplified by a summation over orientations

$$f(\mathbf{x}) \approx \sum_{i=1}^{N_o} \mathcal{W}_\psi^d[f](\mathbf{x}, \mathbf{n}_i) \Delta_i. \quad (54)$$

For this reconstruction by summation we can analyze the stability via the condition number of the mapping that maps an image  $f \in \mathbb{L}_2^g(\mathbb{R}^3)$  to an orientation integrated score

$$A_\psi^d(f) := \sum_{i=1}^{N_o} (\overline{\psi_{\mathbf{n}_i}} \star f) \Delta_i, \quad (55)$$

<sup>11</sup> It can be shown that the angular defect equals  $4\pi$  over the total number of vertices of the platonic solid

with a finite ‘uniform’ spherical sampling  $\{\mathbf{n}_i\}_{i=1}^{N_o}$ , s.t.  $\sum_{i=1}^{N_o} \Delta_i = \mu(S^{d-1}) = \frac{(2\pi)^{\frac{d}{2}}}{\Gamma(d/2)}$ . It has condition number

$$\text{cond}(A_\psi^d) = \frac{\max_{\omega \in B_{0,\varrho}} N_\psi^d(\omega)}{\min_{\omega \in B_{0,\varrho}} N_\psi^d(\omega)},$$

which follows along the same lines as for the fully continuous setting (Theorem 3). Akin to Definition 13 for the continuous case, the reconstruction properties of a set of filters is captured in the following definition:

**Definition 16 (proper wavelet sets)** Let us set a priori bounds<sup>12</sup>  $\delta, M > 0$ ,  $1 \gg \varepsilon > 0$ . (e.g.  $\delta = \frac{1}{8}$ ,  $M = 1.1$ ,  $\varepsilon = 0.01$ ).

Let  $\varrho$  be the maximum frequency radius of our ball-limited image data<sup>13</sup>.

Then,  $\{\psi_{\mathbf{n}_i} \mid i = 1, \dots, N_o\}$  with an almost uniform spherical sampling

with corresponding disjoint surface areas  $\Delta_i$ , such that  $\sum_{i=1}^{N_o} \Delta_i = \mu(S^{d-1}) = \frac{(2\pi)^{\frac{d}{2}}}{\Gamma(d/2)}$  is called a *proper wavelet set* if

- 1.)  $\psi \in \mathbb{L}_1(\mathbb{R}^d) \cap \mathbb{L}_2(\mathbb{R}^d)$ ,
- 2.)  $\psi(R^{-1}\mathbf{x}) = \psi(\mathbf{x})$  for all  $R \in \text{Stab}(\mathbf{a}) \subset SO(d)$ ,
- 3.)  $\forall \omega \in B_{0,\varrho} : \delta \leq M_\psi^d(\omega) := \sum_{i=1}^{N_o} |\hat{\psi}_{\mathbf{n}_i}(\omega)|^2 \Delta_i \leq M$ ,

If moreover, one has

$$4.) \quad \exists \frac{1}{2} \varrho < \varrho_0 < \varrho \quad \forall \omega \in B_{0,\varrho_0} : N_\psi^d(\omega) := \sum_{i=1}^{N_o} \hat{\psi}_{\mathbf{n}_i}(\omega) \Delta_i \in [1 - \varepsilon, 1 + \varepsilon],$$

then we speak of a **proper wavelet set with fast reconstruction property**, cf. (47).

## 2 Proper 2D Wavelets resp. 2D Admissible Wavelets and their Connection to (inverse) Fourier Transform on $SE(2)$ resp. $SIM(2)$

So far we presented a for the application relevant summary of results of our previous theory on invertible orientation scores. A natural question that arises to the reader is how does the invertibility of transform  $W_\psi$  given by

$$\left( \mathbb{R}^2 \ni (x, y) \mapsto f(x, y) \in \mathbb{R} \right) \rightarrow (SIM(2) \ni g \mapsto W_\psi f(g) = (\mathcal{V}_g \psi, f) \in \mathbb{C}) ,$$

relate to the *irreducibility* of the underlying representation  $\mathcal{V}$ , recall (24). Secondly, the question arises how this relates to the fact that we must set<sup>14</sup>  $M_\psi = 1_{B_{0,\varrho}}$  (recall (34) and (36) to guarantee well-posed (ball-limited) images reconstruction of the transform  $\mathcal{W}_\psi$ , given by

$$\left( \mathbb{R}^2 \ni (x, y) \mapsto f(x, y) \in \mathbb{R} \right) \rightarrow \left( SE(2) \ni g \mapsto \widetilde{\mathcal{W}}_\psi f(g) = (\mathcal{U}_g \psi, f) \in \mathbb{C} \right) ,$$

by means of its  $\mathbb{L}_2$ -adjoint  $(\widetilde{\mathcal{W}}_\psi)^*$ . In this section we provide a brief answer to these important questions.

Although the early works of Grossmann et al. [44], [2], are mostly based on decomposition of the identity using extended versions of Schur’s lemma, an alternative and shorter answer to this question can be deduced from the work by Hartmut Führ [40, ch:4] exploiting the relation between the transforms  $W_\psi : \mathbb{L}_2(\mathbb{R}^2) \rightarrow \mathbb{L}_2(SIM(2))$ , recall Eq. (23), and  $\widetilde{\mathcal{W}}_\psi : \mathbb{L}_2(\mathbb{R}^2) \rightarrow \mathbb{L}_2(SE(2))$ , recall Eq. (48), and *inverse* Fourier transforms on respectively the groups  $SIM(2)$  and  $SE(2)$ . Here we will focus only on our specific cases of interest and provide the explicit formulae for these cases.

<sup>12</sup> In practice we choose the default values  $\delta = \frac{1}{8}$  and  $M = 1.1$  and  $\varepsilon = 0.01$  and note that it is actually the ratio  $\frac{M}{\delta}$  that determines the condition number. It is just that it is a convenient choice to set the upper bound close to 1.

<sup>13</sup> Typically  $\varrho$  is close to the Nyquist frequency.

<sup>14</sup> Or  $M_\psi = 1$  if one relies on distributional orientation score transforms in Appendix A.

To this end we use the general identity:  $\text{trace}\{a \otimes b \circ A^*\} = (Ab, a)$ , where  $A$  is some bounded linear operator on a Hilbert space and  $a$  and  $b$  some vectors in the Hilbert space, where we define  $(a \otimes b)(x) = (b, x)a$ . As a result we rewrite the wavelet transform  $W_\psi^{SIM(2)}$  as

$$\begin{aligned} W_\psi^{SIM(2)} f(g) &= (\mathcal{V}_g \psi, f)_{\mathbb{L}_2(\mathbb{R}^2)} = \text{trace}\{f \otimes \psi \circ (\mathcal{V}_g)^*\} = \int_{\widehat{SIM(2)}} \text{trace}\{A_{f,\psi}(\sigma) \sigma(g^{-1})\} \frac{d\nu_{\widehat{SIM(2)}}(\sigma)}{\nu_{\widehat{SIM(2)}}(\mathcal{V})} \\ &= \frac{1}{\nu_{\widehat{SIM(2)}}(\mathcal{V})} [\mathcal{F}_{SIM(2)}^{-1}(A_{f,\psi})](g^{-1}), \end{aligned} \quad (56)$$

where  $\nu_{\widehat{SIM(2)}}$  denotes the Plancherel measure on the dual group  $\widehat{SIM(2)}$ , consisting of all non-equivalent, unitary, *irreducible* representations of the group  $SIM(2)$  and where

$$A_{f,\psi}(\sigma) = \begin{cases} 0 & \text{if } \sigma \neq \mathcal{V} \\ f \otimes \psi & \text{if } \sigma = \mathcal{V} \end{cases}$$

So the Plancherel Theorem for Fourier transform on the group  $SIM(2)$  now yields

$$\|\mathcal{W}_\psi f\|_{\mathbb{L}_2(SIM(2))}^2 = \int_{\widehat{SIM(2)}} \|A_{f,\psi}(\sigma)\|^2 \frac{d\nu_{\widehat{SIM(2)}}(\sigma)}{\nu_{\widehat{SIM(2)}}(\mathcal{V})} = \|f\|_{\mathbb{L}_2(\mathbb{R}^2)}^2 \|\psi\|_{\mathbb{L}_2(\mathbb{R}^2)}^2 \frac{1}{\nu_{\widehat{SIM(2)}}(\mathcal{V})},$$

where  $\|\cdot\|$  denotes the Hilbert-Schmidt norm, which is defined on bounded operators  $A \in B(\mathbb{L}_2(\mathbb{R}^2))$  acting on  $\mathbb{L}_2(\mathbb{R}^2)$  by means of

$$\|A\|^2 = \text{trace}\{A^* A\} = \sum_{k=1}^{\infty} \|A f_k\|^2, \text{ where } \{f_k\}_{k=1}^{\infty} \text{ is some orthonormal basis for } \mathbb{L}_2(\mathbb{R}^2),$$

so in particular, the Hilbert-Schmidt norm of the tensor product  $f \otimes \psi$  of  $\psi$  and  $f$  equals

$$\|f \otimes \psi\|^2 = \|f\|^2 \|\psi\|^2.$$

We conclude that the admissibility constant (18) equals

$$C_\psi = \frac{1}{\nu_{\widehat{SIM(2)}}(\mathcal{V})} \|\psi\|^2$$

and moreover, the unitarity of  $\mathcal{W}_\psi$  directly follows from the Plancherel theorem on  $SIM(2)$  and the fact that  $\mathcal{V} \in \widehat{SIM(2)}$ .

Obviously, one would like to put the same kind of connection of transform  $\mathcal{W}_\psi : \mathbb{L}_2(\mathbb{R}^2) \rightarrow \mathbb{L}_2(SE(2))$  and inverse Fourier transform on  $SE(2)$  but let us recall (from Lemma 2) a technical problem here: In contrast to the representation  $\mathcal{V}$  the representation  $\mathcal{U}$  is *reducible*. Therefore it must be decomposed into irreducible representations, i.e.  $\mathcal{U}$  must be written as a direct integral of irreducible representations. This is similar to the well-known Peter-Weyl theorem for compact groups, [68], but the technical problem is that  $SE(2)$  is not compact giving rise to an over-countable set of irreducible representations requiring direct integral decomposition (for details on these decomposition see [40, p.67-84]) rather than direct sum decomposition. All unitary, irreducible representations, up to unitary equivalence, of  $SE(2)$  are given in [71] and the ones with non-trivial dual Plancherel measure occur only once in the direct integral decomposition of  $\mathcal{U}$ . They can be related to the dual orbits of  $SO(2)$  on  $\mathbb{R}^2$  which coincide with rings in the Fourier domain, using Mackey's theory [55].

Now the theoretical rationale behind  $M_\psi = 1_{B_{0,e}}$ , (recall (34) and (36)), is that the kernel  $\psi$  must be chosen with unit length in each irreducible subspace of  $\mathbb{L}_2^e(\mathbb{R}^2) \cap \mathbb{L}_1(\mathbb{R}^2)$ , meaning that the  $\mathbb{L}_2$ -norm over each fixed ring in the Fourier domain is 1 (note that  $M_\psi(\omega)$  only depends on the radius  $\rho = \|\omega\|$ ) so that each irreducible subspace of  $\mathbb{L}_2(\mathbb{R}^2) \cap \mathbb{L}_1(\mathbb{R}^2)$  is unitarily mapped to each irreducible subspace of the space of orientation scores  $\mathcal{R}(\mathcal{W}_\psi) \subset \mathbb{L}_2(SE(2))$ .

Let us verify these statements on both the transform  $\mathcal{W}_\psi$  between images and orientation scores and the corresponding reducible representation  $\mathcal{U}$  by explicit formulas. First of all we define the representations  $\tilde{\mathcal{U}}^\rho : SE(2) \rightarrow B(\mathbb{L}_2(S_\rho))$ , where  $B(\mathbb{L}_2(S_\rho))$  stands for all bounded operators on the space  $\mathbb{L}_2(S_\rho)$  of quadratic integrable function(s) (classes) defined on the sphere  $S_\rho = \{\omega \in \mathbb{R}^2 \mid \|\omega\| = \rho\}$ , given by

$$\tilde{\mathcal{U}}_g^\rho F(\rho \cos \varphi, \rho \sin \varphi) = e^{i(\rho \cos \varphi, \rho \sin \varphi) \cdot (x, y)} F(\rho \cos(\varphi - \theta), \rho \sin(\varphi - \theta)),$$

for all  $g = (x, y, e^{i\theta}) \in SE(2)$ ,  $F \in \mathbb{L}_2(S_\rho)$ .

**Exercise 10** Show that these representations are unitary equivalent to well-known unitary, irreducible representations of  $SE(2)$ , [71],[12, ch: 10.2], given by

$$\mathcal{U}_g^\rho \phi(\mathbf{v}) = e^{-i\rho(x,v)} \phi((R_\theta)^{-1} \mathbf{v}), \quad \rho > 0, \phi \in \mathbb{L}_2(S_1), \mathbf{v} \in S_1, g = (\mathbf{x}, e^{i\theta}) \in SE(2), \quad (57)$$

*hint:  $\tilde{\mathcal{U}}_g^\rho = \mathcal{D}_\rho \circ \mathcal{U}_g^\rho \circ \mathcal{D}_\rho^{-1}$  with dilation operator  $\mathcal{D}_\rho : \mathbb{L}_2(S_1) \rightarrow \mathbb{L}_2(S_\rho)$  given by  $\mathcal{D}_\rho \phi(\mathbf{v}) = \rho^{-\frac{1}{2}} \phi(\rho^{-1} \mathbf{v})$*

. Consider the dual orbit space  $S^1 \backslash \mathbb{R}^2$ , where the dual orbits are given by  $S_\rho = \{A^T \boldsymbol{\omega} \mid A \in SO(2)\}$ , with  $\rho = \|\boldsymbol{\omega}\|$ , then we have the following direct integral decomposition

$$\mathcal{F} \circ \mathcal{U}_g \circ \mathcal{F}^{-1} = \int_{\mathbb{R}^+ \equiv S^1 \backslash \mathbb{R}^2}^{\oplus} \tilde{\mathcal{U}}_g^\rho d\nu(S_\rho),$$

where the measure on the dual orbits by identification  $\rho \in \mathbb{R}^+ \equiv S_\rho \in S^1 \backslash \mathbb{R}^2$  equals  $d\nu(S_\rho) = \rho d\rho$ . Analogously to (56), we have

$$\begin{aligned} \mathcal{W}_\psi f(g) &= (\mathcal{U}_g \psi, f)_{\mathbb{L}_2(\mathbb{R}^2)} = \left( \int_{\mathbb{R}^+}^{\oplus} \tilde{\mathcal{U}}_g^\rho \rho d\rho \mathcal{F}\psi, \mathcal{F}f \right)_{\mathbb{L}_2(\mathbb{R}^2)} \\ &= \int_0^\infty ((\tilde{\mathcal{U}}_g^\rho) \mathcal{F}\psi|_{S_\rho}, \mathcal{F}f|_{S_\rho}) \rho d\rho = \int_0^\infty \text{trace} \left( \left( \mathcal{F}f|_{S_\rho} \otimes \mathcal{F}\psi|_{S_\rho} \right) \circ \tilde{\mathcal{U}}_{g^{-1}}^\rho \right) \rho d\rho. \end{aligned} \quad (58)$$

Now  $\rho \mapsto \tilde{\mathcal{U}}^\rho$  is injective into the dual group  $\widehat{SE}(2)$ , since  $\tilde{\mathcal{U}}^\rho$  is unitary equivalent to the unitary irreducible representations (57). Moreover  $d\nu(S_\rho)$  equals the restriction of the Plancherel measure to  $\{\tilde{\mathcal{U}}^\rho\}_{\rho>0}$ , [71], so we see that (58) can be rewritten as

$$\boxed{\mathcal{W}_\psi f(g^{-1}) = \mathcal{F}_{SE(2)}^{-1}(\rho \mapsto \mathcal{F}f|_{S_\rho} \otimes \mathcal{F}\psi|_{S_\rho})(g).} \quad (59)$$

Now by the Plancherel theorem on  $SE(2)$ , [71], [12] (and  $\mathbb{R}^2$ ) one has

$$\boxed{\begin{aligned} \|\mathcal{W}_\psi f\|_{\mathbb{L}_2(SE(2))}^2 &= \int_0^\infty \| \mathcal{F}f|_{S_\rho} \otimes \mathcal{F}\psi|_{S_\rho} \|^2 \rho d\rho = \int_0^\infty \| \mathcal{F}\psi|_{S_\rho} \|_{\mathbb{L}_2(S_\rho)}^2 \| \mathcal{F}f|_{S_\rho} \|_{\mathbb{L}_2(S_\rho)}^2 \rho d\rho \\ \|f\|_{\mathbb{L}_2(\mathbb{R}^2)}^2 &= \| \mathcal{F}f \|_{\mathbb{L}_2(\mathbb{R}^2)}^2 = \int_0^\infty \| \mathcal{F}f|_{S_\rho} \|_{\mathbb{L}_2(S_\rho)}^2 \rho d\rho, \end{aligned}} \quad (60)$$

so indeed we have the following sufficient and necessary condition for  $\mathbb{L}_2$ -norm preservation:

$$\widetilde{\mathcal{W}}_\psi = \mathcal{W}_\psi \Leftrightarrow M_\psi = 1_{B_{0,e}} \Leftrightarrow \| \mathcal{F}\psi|_{S_\rho} \|_{\mathbb{L}_2(S_\rho)}^2 = 1 \text{ for all } \rho \geq \rho = \|\boldsymbol{\omega}\| > 0,$$

where we recall the definition of  $M_\psi$  (34) and where we note that

$$M_\psi(\boldsymbol{\omega}) = \| \mathcal{F}\psi|_{S_{\rho=\|\boldsymbol{\omega}\|}} \|_{\mathbb{L}_2(S_\rho)}^2 = \int_{S^2} |\mathcal{F}\psi(\rho \cos \varphi, \rho \sin \varphi)|^2 \rho d\varphi, \text{ with } \rho = \|\boldsymbol{\omega}\|, \quad (61)$$

Moreover, for  $\psi \in \mathbb{L}_2^e(\mathbb{R}^2) \cap \mathbb{L}_1(\mathbb{R}^2)$ , with  $M_\psi = 1_{B_{0,e}}$  its continuous Fourier transform  $\mathcal{F}\psi$  has equal  $\mathbb{L}_2$ -norm over each dual orbit, implying that each irreducible subspace of  $\mathbb{L}_2(\mathbb{R}^2) \cap \mathbb{L}_1(\mathbb{R}^2)$  given by

$$\{f \in \mathbb{L}_2^e(\mathbb{R}^2) \cap \mathbb{L}_1(\mathbb{R}^2) \mid \text{supp}\{\mathcal{F}f\} \subset S_\rho\}$$

is unitarily mapped onto each irreducible subspace within  $\mathcal{R}(\mathcal{W}_\psi) \subset \mathbb{L}_2(SE(2))$ .

**Exercise 11** Study Appendix A and verify that exactly the same arguments (but now with  $\rho \rightarrow \infty$ ) as above apply to proper distributional wavelets  $\psi \in H^{-I}$  in distributional orientation score transforms.



### 3 Construction of Proper Wavelets

#### 3.1 Simple numeric ‘cake-wavelet’ approach relying on DFT

A class of 2D cake-wavelets, see [18, 26], was proposed for the 2D orientation score transformation, which are effective in various medical imaging applications [38, 6].

We now generalize these 2D cake-wavelets to dD cake-wavelets, and thanks to the splitting in Appendix B, we no longer need the spatial window used there. Our cake-wavelets (which are proper wavelets with reconstruction property), should fulfill a set of requirements:

1. The orientation score should be constructed for a finite number ( $N_o$ ) of orientations.
2. The transformation should be invertible and reconstruction should be achieved by summation. Therefore we aim for  $N_\psi^d \approx 1$ . Additionally, to guarantee all frequencies are transferred equally to the orientation score domain we aim for  $M_\psi^d \approx 1$ . The set should be a proper wavelet set with fast reconstruction property (Def. 16)
3. The kernel should be strongly directional. Preferably, for  $d = 2$  the kernels must be supported in a cone within the Fourier domain in view of the  $SE(2)$ -uncertainty principle [18, ch:7.5], likewise the  $SIM(2)$ -uncertainty principle [3].
4. The kernel should be ball-separable in the Fourier domain, i.e.,

$$(\mathcal{F}\psi)(\omega) = g(\rho) A\left(\frac{\omega}{\|\omega\|}\right), \text{ with } \rho = \|\omega\| \quad (62)$$

and as the wavelet  $\psi$  must be proper (recall Definition 13) it has a rotational symmetry around the normalized reference-axis  $\mathbf{a}$ , recall (42), we must have the form

$$A\left(\frac{\omega}{\|\omega\|}\right) = \mathfrak{h}\left(\frac{\omega}{\|\omega\|} \cdot \mathbf{a}\right). \quad (63)$$

5. The kernel should be localized in the spatial domain, since we want to pick up local oriented structures.
6. The real part of the kernel should detect oriented structures and the imaginary part should detect oriented edges. The constructed orientation score is therefore a complex orientation score.

**Remark 8 (Some intuition on the design of cake-wavelets)**

The intuitive idea is that for  $d = 2$  covering pieces of cake fill up the entire cake of frequencies in the Fourier domain. Recall to this end the role of function  $M_\psi$  in Theorem 2. When one applies the same idea by combining covering ‘ice-cones’ to create a ‘ball’ one does not get a real-part that is a line detector. One rather gets a plane detector see Figure 7 or [18, fig.4.14]. To this end one must for  $d = 3$  rely on a Funk-Radon transform, that turns ‘icecones’ into ‘donuts’ that yield line-detecting real-parts. See Figure 8. For the statement that the splitting in Appendix B allows us to cut on extra spatial windows, see Figure 9.

**Exercise 12 (anisotropies in spatial domain and Fourier domain)**

- a.) Compute the Fourier transform of the 2D anisotropic Gaussian  $G(\mathbf{x}) = \frac{1}{4\pi s} e^{-\frac{\|A\mathbf{x}\|^2}{4s}}$  with  $A = \text{diag}(\lambda, \lambda^{-1}) \in \mathbb{R}^{2 \times 2}$ , with  $0 < \lambda \ll 1$ ,  $s > 0$ , and  $\mathbf{x} = (x, y)^T \in \mathbb{R}^2$ .
- b.) Compute the Fourier transform of the 3D anisotropic Gaussian  $G(\mathbf{x}) = \frac{1}{(4\pi s)^{\frac{3}{2}}} e^{-\frac{\|A\mathbf{x}\|^2}{4s}}$  with  $A = \text{diag}(\lambda, \lambda^{-\frac{1}{2}}, \lambda^{-\frac{1}{2}}) \in \mathbb{R}^{3 \times 3}$ ,  $0 < \lambda \ll 1$ ,  $s > 0$ , and  $\mathbf{x} = (x, y, z)^T \in \mathbb{R}^3$ .
- c.) How does this exercise relate to the above remark, and what you see in Figure 7 and Figure 8?

**Remark 9 (Choice of radial function  $g$  and its decay)** To prevent numerical problems with the inverse DFT after sampling in the Fourier domain it is best to aim at  $M_\psi(\omega) \approx 1$  for  $\|\omega\| < \varrho$ , where  $\varrho$  is close to the Nyquist frequency  $\varrho_N$  of the discretely sampled image. Because of the discontinuity at  $\|\omega\| = \varrho$ , which causes practical problems with the discrete inverse Fourier transform, we will use wavelets  $\psi$ , with  $M_\psi(\omega) = \mathcal{M}_N(\rho^2 t^{-1})$ ,  $N \in \mathbb{N}$ ,  $t > 0$  and  $\rho = \|\omega\|$  where

$$g(\rho) = \mathcal{M}_N(\rho^2 t^{-1}) = e^{-\frac{\rho^2}{t}} \sum_{k=0}^N \frac{(\rho^2 t^{-1})^k}{k!} \leq 1, \quad (64)$$

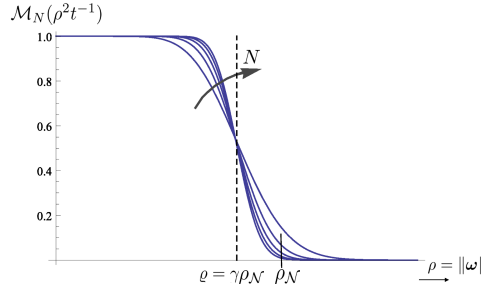


**Fig. 6** Plots of  $\mathcal{M}_N(\rho^2/t)$ , with  $t = \frac{2(\gamma \varrho_N)^2}{1+2N}$  for  $N = 5, 10, 15, 20, 25$

where  $t$  denotes a scale parameter. To fix the inflection point close to the Nyquist frequency  $\varrho_N$ , say at  $\rho = \varrho := \gamma \cdot \varrho_N$  with  $0 \ll \gamma < 1$ , we set

$$t = t_* := \frac{2 \varrho^2}{1+2N} \quad (65)$$

in order to fix the bending point:

$$\left. \frac{d^2}{d\rho^2} \mathcal{M}_N(\rho^2 t^{-1}) \right|_{\rho=\varrho} = 0,$$

see Fig. 6). The function  $\mathcal{M}_N$  is a Gaussian function at scale  $t$  multiplied with the Taylor series of its inverse up to a finite order  $2N$  to ensure a slower decay. Therefore  $\mathcal{M}_N$  smoothly approximates 1 on the domain  $\rho \in [0, \varrho]$ , see Figure 6. A wavelet  $\psi : \mathbb{R}^2 \rightarrow \mathbb{C}$  with  $M_\psi(\boldsymbol{\omega}) = \mathcal{M}_N(\|\boldsymbol{\omega}\|^2 t_*^{-1})$  is a proper wavelet according to Definition 13. A simple alternative radial Fourier decay function that does a similar job is given by

$$g(\rho) = \frac{1}{2} \left( 1 - \operatorname{erf} \left( \frac{\rho - \varrho}{\sigma_{\operatorname{erf}}} \right) \right), \quad (66)$$

with  $\operatorname{erf}(z) = \frac{2}{\sqrt{\pi}} \int_0^z e^{-x^2} dx$ , and where  $\sigma_{\operatorname{erf}}$  controls the slope of the error function, similar to  $N$  above.

### 3.1.1 The 2D case

We use polar coordinates  $\boldsymbol{\omega} = (\rho \cos \varphi, \rho \sin \varphi)^T$  and set

$$\begin{aligned} \hat{\psi}(\rho \cos \varphi, \rho \sin \varphi) &= A(\cos \varphi, \sin \varphi) g(\rho), \text{ with} \\ \text{angular function } A(\cos \varphi, \sin \varphi) &= B_k \left( \frac{(\varphi \bmod 2\pi) - \frac{\pi}{2}}{s_\theta} \right), \text{ with angular stepsize } s_\theta = \frac{2\pi}{N_o} \\ \text{and radial function } g(\rho) &\text{ given by (64) or by (66).} \end{aligned} \quad (67)$$

where  $N_o$  denotes the number of orientation we encode in the score, and where  $B_k$  denotes the  $k$ th order B-spline given by

$$B_k(x) = (B_{k-1} * B_0)(x), \quad B_0(x) = \begin{cases} 1 & \text{if } -1/2 < x < +1/2 \\ 0 & \text{otherwise} \end{cases}. \quad (68)$$

which are chosen because of their strictly local support and covering property, see Figure 10.

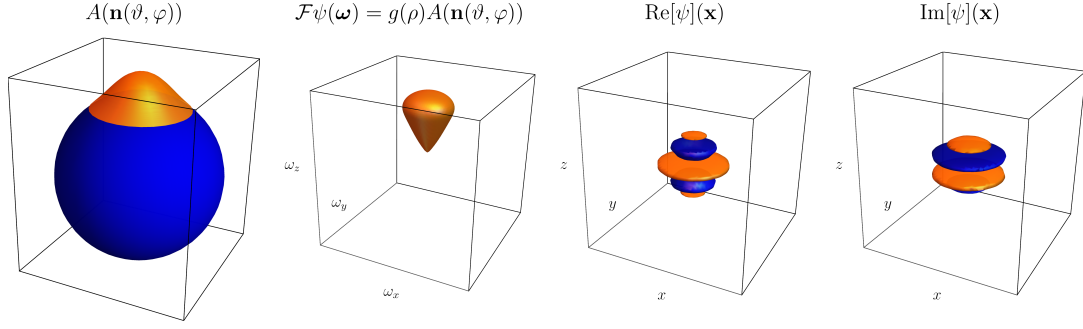
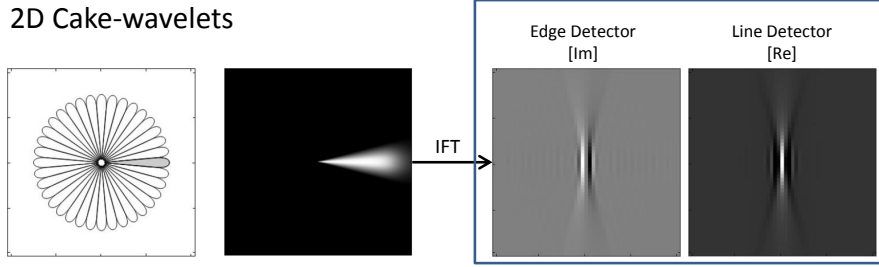


**Fig. 7** When directly setting orientation distribution  $A = A_{\text{aux}}$  as angular part of the Fourier transformed wavelet  $\mathcal{F}\psi$  we construct plate detectors. From left to right: Orientation distribution  $A = A_{\text{aux}}$  wavelet in the Fourier domain, the plate detector (real part) and the edge detector (imaginary part). Orange: Positive iso-contour. Blue: Negative iso-contour. Parameters used:  $L = 19, \sigma_\theta = 0.25, \sigma_{\text{erf}} = 3, \gamma = 0.85$  and evaluated on a grid of  $51 \times 51 \times 51$  pixels.

### 2D Cake-wavelets



### 3D Cake-wavelets

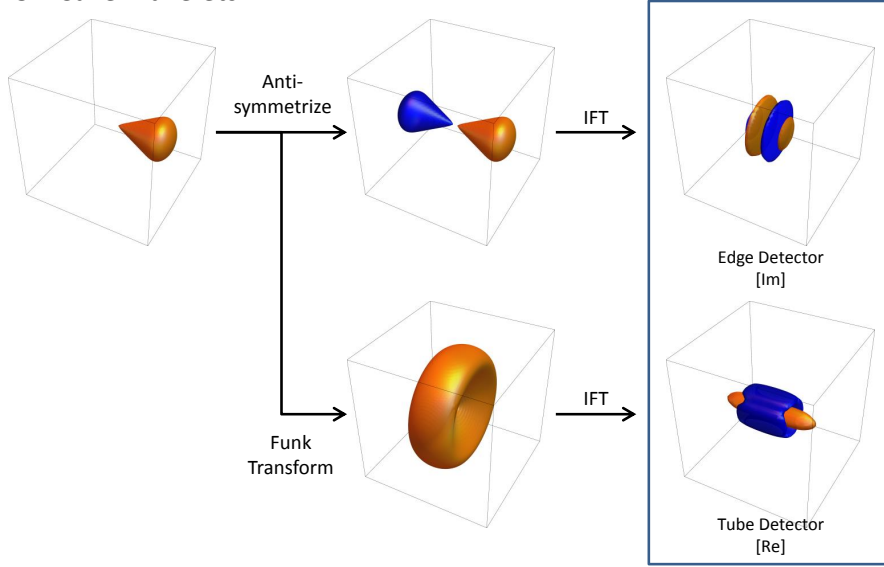


**Fig. 8** Cake-Wavelets. *Top* 2D cake-wavelet given by (67). From left to right: Illustration of the Fourier domain coverage, the wavelet in the Fourier domain and the real and imaginary part of the wavelet in the spatial domain. *Bottom* 3D cake-wavelet given by (73). Overview of the transformations used to construct the wavelets from a given orientation distribution. Upper part: The wavelet according to Eq. (75). Lower part: The wavelet according to Eq. (74). IFT: Inverse Fourier Transform. Parameters used:  $L = 16, s_o = \frac{1}{2}(0.25)^2, s_\rho = 2, \sigma_{\text{erf}} = 3, \gamma = 0.85$  and evaluated on a grid of  $81 \times 81 \times 81$  pixels.

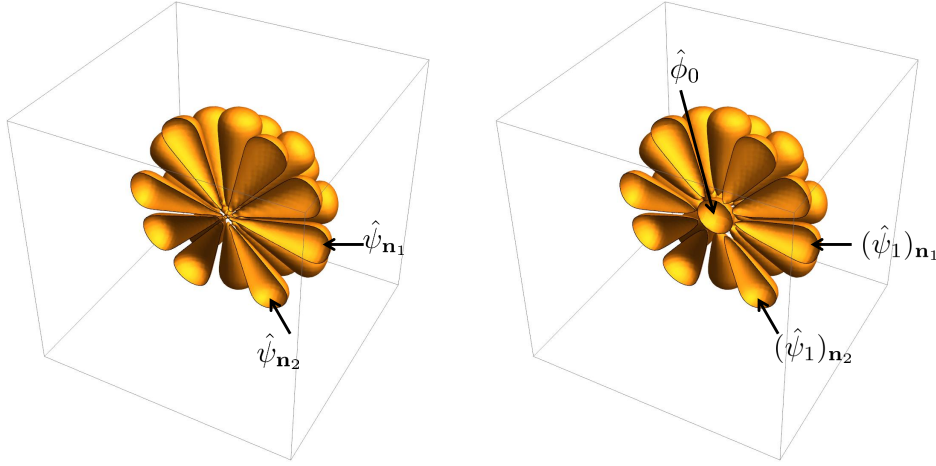


**Fig. 9** Coverage of the Fourier domain before and after splitting according to Appendix B. *Left:* The different wavelets cover the Fourier domain. The "sharp" parts when the cones reach the center however cause the filter to be non-localized, which was solved in earlier works by applying a spatial window after filter construction. *Right:* By splitting the filter in lower and higher frequencies we solve this problem. In the figure we show  $g(\rho)A(\mathbf{n}(\vartheta, \varphi))$  for the different filters, before applying the Funk transform to the orientation distribution  $A$ .

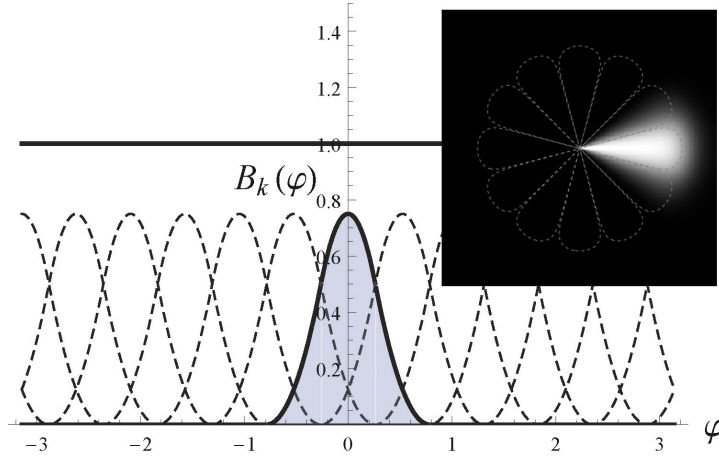


**Fig. 10** The use of B-splines in the construction of cake wavelets. Plot showing quadratic B-splines ( $k=2$ ), the sum of all shifted B-splines add up to 1. The image in the upper right corner illustrates a Fourier cake wavelet  $\tilde{\psi}^{cake}(\omega)$  constructed using quadratic B-splines and  $\mathcal{M}_N$  with  $N = 60$ , according to Eq. (67).

**Exercise 13** We set a priori bounds  $\delta, M > 0$ ,  $1 \gg \varepsilon > 0$  by our default parameters  $\delta = \frac{1}{8}$  and  $M = 1.1$ . Let  $\psi$  given by (67) with radial function (64) with  $N = 8$  and with  $t = t_*$  given by (65). It can be verified (you do not have to show this) that for these settings one has

$$\delta \leq |g(\rho)|^2 \leq M \text{ for all } 0 < \rho < \varrho.$$

- Compute  $B_1(x)$  symbolically.
- Show (by induction w.r.t.  $k$ ) that equality  $\sum_{i \in \mathbb{Z}} B_k(x - i) = 1$  holds for all  $k \in \mathbb{N} \cup \{0\}$  and for all  $x \in \mathbb{R}$ .
- Show (by induction w.r.t.  $k$ ) that equality  $\int_{\mathbb{R}} B_k(x) dx = 1$  holds for all  $k \in \mathbb{N} \cup \{0\}$ .
- Show that  $\psi$  given by (67) is a **proper wavelet** with upper-bound  $M_{new} = M * \|A\|_{L_2(S^1)}^2$  and with lower-bound  $\delta_{new} = \delta * \|A\|_{L_2(S^1)}^2$  (according to Definition 13).

### 3.1.2 The 3D case

In the 3D-case things get a little bit more complicated compared to the 2D case. First of all, the B-splines on  $S^1$  do not straightforwardly generalize to B-splines on  $S^2$ , and secondly choosing a sharp cone in the 3D-Fourier domain as a point of departure, does not yield an appropriate 3D-cake wavelet with a line-detecting real part, as can be seen in Figure 7.

We now need to find an appropriate angular part  $A$  for the cake-wavelets. First, we specify an auxiliary orientation distribution  $A_{\text{aux}} : S^2 \rightarrow \mathbb{R}^+$ , which determines what orientations the wavelet should measure. To satisfy requirement 3 this function should be a localized spherical window, for which we propose the (truncated) spherical diffusion kernel centered around reference axis  $\mathbf{a} = (0, 0, 1)^T$ :

$$\begin{aligned} A_{\text{aux}}(\mathbf{n}(\vartheta, \varphi)) &= G_{s_o}^{S^2}(\mathbf{n}(\vartheta, \varphi)) = G_{s_o}^{S^2}(\mathbf{n}(\vartheta, 0)) \\ &= \sum_{l=0}^L a_l^0 Y_l^0(\vartheta, \varphi) = \sum_{l=0}^L e^{-s_o l(l+1)} Y_l^0(0, 0) Y_l^0(\vartheta, 0), \quad 0 < L, \end{aligned} \quad (69)$$

with  $s_o > 0$  and  $\mathbf{n}(\vartheta, \varphi) = (\sin \vartheta \cos \varphi, \sin \vartheta \sin \varphi, \cos \vartheta)$ . The parameter  $s_o$  determines the trade-off between requirements 2 and 3, where higher values give a more uniform  $M_\psi^d$  at the cost of less directionality.

*Remark 10* Because of the exponential decay w.r.t.  $l$  in  $A_{\text{aux}}$  we can approximate the true diffusion kernel (where  $L \rightarrow \infty$ ) when truncating at the smallest  $L$  such that  $a_L^0/a_0^0 < 10^{-3}$  (e.g.  $L = 21$  for  $s_o = \frac{1}{2}(0.25)^2$ ).

*Remark 11 (basic properties spherical harmonics)* Recall that the spherical harmonics  $\{Y_l^m\}_{l=0, |m| \leq l}^\infty$  were given by (6), and recall that they form an orthonormal basis for  $\mathbb{L}_2(S^2)$  with the property

$$\Delta_{S^2} Y_l^m = -l(l+1) Y_l^m, \quad e^{s \Delta_{S^2}} Y_l^m = e^{-l(l+1)s} Y_l^m, \quad \text{and} \quad \mathcal{R}_{\mathbf{a}, \alpha} Y_l^m = e^{im\alpha} Y_l^m, \quad (70)$$

from which the 2nd identity in (69) readily follows. They also form a complete orthonormal system w.r.t. Funk transform

$$FA(\mathbf{n}) = \frac{1}{2\pi} \int_{S_p(\mathbf{n})} A(\mathbf{n}') ds(\mathbf{n}'), \quad (71)$$

where integration is performed over  $S_p(\mathbf{n})$  denoting the great circle perpendicular to  $\mathbf{n}$ . In fact, one has

$$FY_l^m = P_l(0) Y_l^m, \quad (72)$$

where we allow ourselves (sloppy) notation  $Y_l^m(\mathbf{n}(\varphi, \vartheta)) := Y_l^m(\varphi, \vartheta)$ .

*Remark 12* In implementations, one truncates the spherical harmonics at  $L \in \mathbb{N}$  which leaves  $\sum_{l=0}^L (2l+1) = (L+1)^2$  coefficients. If one would start with an almost uniform spherical sampling  $\{A(\mathbf{n}_i)\}_{i=1}^{N_o}$  for some square integrable  $A : S^2 \rightarrow \mathbb{C}$ , then it is wise to choose the number of spherical harmonics a little less than  $N_o$  to prevent both over-fitting and data-loss, when relying on the pseudo-inverse of the discretization of the inverse discrete spherical harmonic transform to approximate the forward continuous (SHT) Spherical Harmonic Transform  $(SHT(A))(l, m) = (Y_l^m, A)_{\mathbb{L}_2(S^2)}$ . For a short, self-contained explanation on discretization of the SHT and its inverse see [27, ch:7.1].

Via our auxiliary function  $A_{\text{aux}}$  like the spherical heat-kernel in (69) we construct our 3D cake-wavelets in the spatial Fourier domain as follows. Note that one the expansion in spherical harmonics of auxiliary function  $A_{\text{aux}}$  all rotated wavelets are computed and steered analytically without approximations.

**Result 1.** *Let  $A_{\text{aux}} : S^2 \rightarrow \mathbb{R}^+$  be an  $\mathbb{L}_1$ -normalized function mostly supported in a sharp convex cone around the  $\mathbf{a}$ -axis and symmetrically around the  $\mathbf{a}$ -axis (i.e the  $z$ -axis recall (42)). Then  $A_{\text{aux}}$ , together with our function  $g(\rho)$  given by (64) or by (66), provides our wavelet  $\hat{\psi}$  in the Fourier domain via*

$$\begin{aligned} \hat{\psi}(\boldsymbol{\omega}) &= g(\rho) (FA_{\text{aux}}(\mathbf{n}_\omega) + A_{\text{aux}}(\mathbf{n}_\omega) - A_{\text{aux}}(-\mathbf{n}_\omega)), \\ \text{with } \boldsymbol{\omega} &= \rho \cdot \mathbf{n}_\omega = \rho \cdot \mathbf{n}(\vartheta, \varphi) \text{ and } \rho = \|\boldsymbol{\omega}\|, \end{aligned} \quad (73)$$

The real part of  $\psi$  is a tube detector given by

$$\text{Re}(\psi) = \mathcal{F}^{-1}(\boldsymbol{\omega} \mapsto g(\rho) \cdot (FA_{\text{aux}})(\mathbf{n}_\omega)). \quad (74)$$

The imaginary part of  $\psi_{\mathbf{n}}$  is an edge detector given by

$$\text{Im}(\psi) = \frac{1}{i} \mathcal{F}^{-1} (\boldsymbol{\omega} \mapsto g(\rho) \cdot (A(\mathbf{n}_{\boldsymbol{\omega}}) - A(-\mathbf{n}_{\boldsymbol{\omega}}))). \quad (75)$$

When expanding the angular part in spherical harmonics and choosing  $A = G_{s_o}^{S^2}$ :

$$A_{aux}(\mathbf{n}(\vartheta, \varphi)) = \sum_{l=0}^L a_l^0 Y_l^0(\vartheta, \varphi), \quad \text{with } a_l^0 = \sqrt{\frac{2l+1}{4\pi}} e^{-l(l+1)s_o}, \quad (76)$$

we have the following wavelet in the Fourier domain

$$\hat{\psi}(\boldsymbol{\omega}) = g(\rho) \cdot A(\mathbf{n}(\vartheta, \varphi)) := g(\rho) \cdot \sum_{l=0}^L c_l^0 Y_l^0(\vartheta, \varphi), \quad (77)$$

and the coefficients  $a_l^0$  of  $A_{aux}$  and  $c_l^0$  of the angular part  $A$  of  $\hat{\psi}$  relate via

$$c_l^0 = P_l(0) a_l^0 + (1 - (-1)^l) a_l^0. \quad (78)$$

We obtain rotated versions of our filter via

$$\hat{\psi}_{\mathbf{n}}(\boldsymbol{\omega}) = g(\rho) \cdot \sum_{l=0}^L \sum_{m'=-l}^l c_l^0 D_{0,m'}^l(\gamma, \beta, 0) Y_l^{m'}(\vartheta, \varphi), \quad (79)$$

As we do not have analytical expressions for the spatial wavelets  $\psi_{\mathbf{n}}$ , we sample the filter in the Fourier domain using Eq. (79) and apply an inverse DFT afterwards. For  $L > 0$ ,  $N > 0$  (or  $\sigma_{erf}^{-1}$ ) sufficiently large the wavelet  $\psi$  is a (steerable) proper wavelet with fast reconstruction property (Def. 13).

#### Exercise 14 (questions on the construction of 3D cakewavelets)

- Show that (78) follows by (73) and (69), (72).
- Show that the wavelets real part (74) and its imaginary part (75) follow by (73).
- See Figure 8. Why is the anti-symmetrization required in (75) and (73)?
- Show that the fast reconstruction property indeed holds for  $g(\rho)$  given by (66) and  $\sigma_{erf}^{-1}$  sufficiently large. *hint:*

$$g(\rho) = g(\rho) P_0(0) = g(\rho) \int_{S^2} A(\mathbf{n}) d\sigma(\mathbf{n}) = g(\rho) \int_{S^2} A_{aux}(\mathbf{n}) d\sigma(\mathbf{n}) = N_{\psi}(\boldsymbol{\omega}), \quad \rho = \|\boldsymbol{\omega}\|.$$

**Lemma 6** Let  $\psi$  be a wavelet constructed via the procedure in Result 1. Then we have the bounds

$$1 - \sum_{l=0}^L \|\mathbf{d}_l\| \sqrt{\frac{2l+1}{4\pi}} \leq N_{\psi}^d \leq 1 + \sum_{l=0}^L \|\mathbf{d}_l\| \sqrt{\frac{2l+1}{4\pi}}, \quad (80)$$

with  $\mathbf{d}_l = (d_l^m)_{m=-l}^l$  and  $d_l^m = \sum_{i=1}^{N_o} c_l^0 \cdot \Delta_i \cdot \mathcal{D}_{0,m}^l(0, \beta_i, \gamma_i)$ .

*Proof.* First we expand function  $N_{\psi}^d$  in spherical harmonics:

$$\begin{aligned} N_{\psi}^d(\boldsymbol{\omega}) &= \sum_{i=1}^{N_o} \mathcal{F}[\psi_{\mathbf{n}_i}](\boldsymbol{\omega}) \Delta_i = g(\rho) \sum_{i=1}^{N_o} h_{\mathbf{n}_i}(\vartheta, \varphi) \Delta_i \\ &= g(\rho) \sum_{l=0}^L \sum_{m'=-l}^l \underbrace{\sum_{i=1}^{N_o} c_l^0 D_{0,m'}^l(0, \beta_i, \gamma_i) \Delta_i}_{d_l^{m'}} Y_l^{m'}(\vartheta, \varphi) \\ &= g(\rho) \sum_{l=0}^L \sum_{m'=-l}^l d_l^{m'} Y_l^{m'}(\vartheta, \varphi) \end{aligned} \quad (81)$$

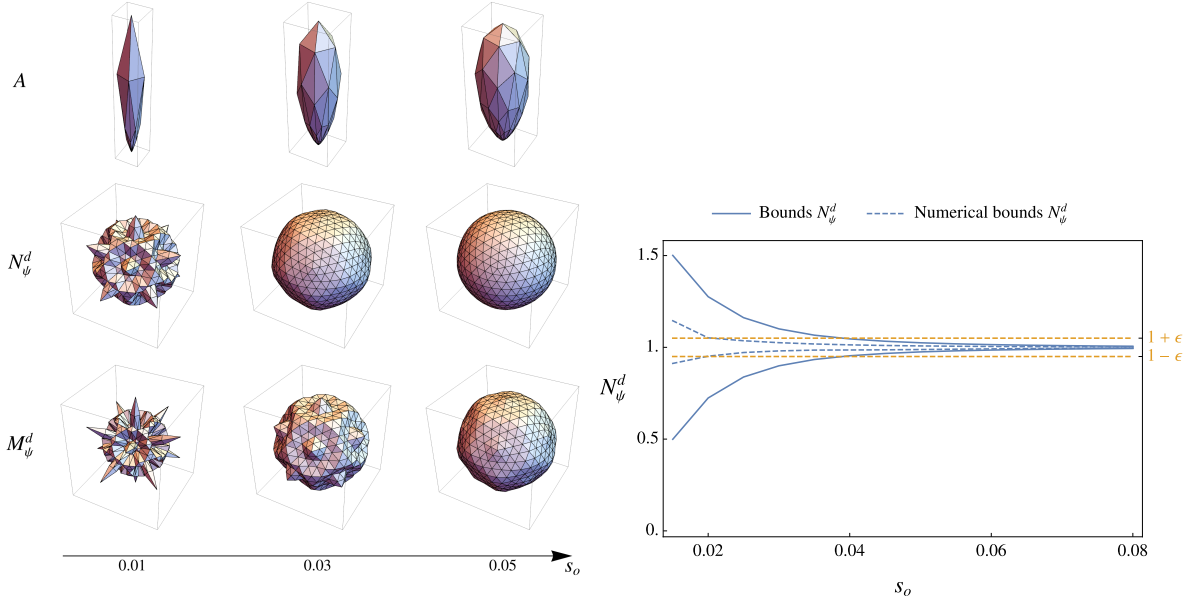


**Fig. 11** Inspection of the stability of the transformation for different values of  $s_o$  given a orientation distribution  $A = G_{s_o}^{S^2}$  and for  $N_o = 42$ . *Left:* Spherical plot of  $A$  and the angular part of polar separable function  $N_\psi^d$  and  $M_\psi^d$  which gives insight in whether we cover all orientations equally. Where closer to the ball means more equal coverage of all orientations. *Right:* The upper and lower bounds of  $N_\psi^d$ . Comparison of the bounds according to Eq. (80) (filled line) and numerical results (dashed line) of the bounds by a very fine sampling of the sphere (icosahedron of tessellation order 6).

We have  $g(\rho) = 1$  for  $\rho = \|\omega\| \leq \varrho$ , but we still need to quantify the angular part. We define  $\mathbf{Y}_l^N = (Y_l^{-l}, Y_l^{-l+1}, \dots, Y_l^{l-1}, Y_l^l)$ , so that

$$\sum_{l=0}^L \sum_{m'=-l}^l d_l^{m'} Y_l^{m'}(\vartheta, \varphi) = \sum_{l=0}^L \mathbf{d}_l \cdot \mathbf{Y}_l(\vartheta, \varphi) = Y_0^0(\vartheta, \varphi) c_0^0 + \sum_{l=1}^L \mathbf{d}_l \cdot \mathbf{Y}_l(\vartheta, \varphi) = 1 + \sum_{l=1}^L \mathbf{d}_l \cdot \mathbf{Y}_l(\vartheta, \varphi) \quad (82)$$

This varying component should remain small. We use Cauchy-Schwarz for each order  $l$ :

$$\left| \sum_{l=0}^L \mathbf{d}_l \cdot \mathbf{Y}_l(\vartheta, \varphi) \right| \leq \sum_{l=0}^L |\mathbf{d}_l \cdot \mathbf{Y}_l(\vartheta, \varphi)| \leq \sum_{l=0}^L \|\mathbf{d}_l\| \|\mathbf{Y}_l(\vartheta, \varphi)\| = \sum_{l=0}^L \|\mathbf{d}_l\| \sqrt{\frac{2l+1}{4\pi}}, \quad (83)$$

from which (80) follows.  $\square$

See Fig. 11 for visual inspection of bounds of  $M_\psi^d$  and  $N_\psi^d$ , and numerical results for the bounds of  $N_\psi^d$ .

**Corollary 3** *Given our analytical bounds (80) from Proposition 6 and  $N_o = 42$ , we can guarantee that our set of wavelets from Result 1 sampled at  $\{\mathbf{n}_i\}_{i=1}^{N_o}$  is a proper wavelet set with fast reconstruction property according to Def. 16 with  $\epsilon = 0.05$  when choosing parameter  $s_0 \gtrapprox 0.04$ .*

In practice we have a proper wavelet set with fast reconstruction property already for smaller values of  $s_o$ , as follows by the numeric computations in Figure 11 where we see that  $s_0 \gtrapprox 0.02$  is already enough.

#### Exercise 15 (question on the construction of 3D proper wavelet sets)

Prove that for each  $N_0$  there exists a unique  $s_{\min}(N_0) > 0$  such that for all  $s > s_{\min}(N_0)$  the set of wavelets from Result 1 and verify Corollary 3.

In the two subsequent subsections, we will overcome the theoretical short-coming that we must sample the cake-wavelets in the Fourier domain and apply an inverse DFT (iDFT) to get their representations on the spatial grid. We will consider two natural approaches for constructing proper wavelets that

allow for a spatial analytic description in both spatial and Fourier domain (where one relies on inverse continuous Fourier transform rather than iDFT):

- A) proper wavelet expansion in the harmonic oscillator basis.
- B) proper wavelet expansion in a modified (weighted) Zernike basis.

From the practical point of view, we will observe that:

- the harmonic oscillator basis approach, generalizes Kalitzin's wavelet [52], but has some limitations (especially when applying hard truncations) for local control of proper wavelets.
- the modified Zernike basis allows for a relatively simple analytic description of proper wavelets, whose grid samplings are very close to the practical 3D cake-wavelets described in Result 1 above.

### 3.2 Analytic Approach relying on Expansion in Eigenfunctions of the Harmonic Oscillator

For control of the shape and the localization of proper wavelets  $\psi$  we must analyze in the spatial domain, whereas for control of the stability/invertibility of the orientation score transform we need to analyze in the Fourier domain. It is therefore, important to come up with a choice of basis in the Fourier domain that has a simple counterpart in the spatial domain as well.

A natural idea here (inspired by Kalitzin's distributional wavelet, see Exercise 19 in Appendix A), is to use the Harmonic oscillator basis for this purpose. Especially in view of the Bochner-Hecke theorem, cf. Appendix C, that allows us to easily transfer ball-coordinate expansions of wavelets from the spatial to the Fourier domain and back.

Fourier transform  $\mathcal{F}$  and the Harmonic oscillator operator  $-\Delta + \|\mathbf{x}\|^2$  commute

$$\mathcal{F} \circ (-\Delta + \|\mathbf{x}\|^2) = (-\Delta + \|\boldsymbol{\omega}\|^2) \circ \mathcal{F},$$

where we apply multipliers  $\mu = \|\mathbf{x}\|^2, \|\boldsymbol{\omega}\|^2$  with their (unbounded) multiplier operators  $\mathcal{M}_\mu$  acting in respectively the spatial and Fourier domain, and thereby they have a common basis of eigenfunctions.

#### 3.2.1 The 2D case

In this subsection we will expand our wavelet into eigenfunctions of the 2D harmonic oscillator.

Note that  $\mathbb{L}_2(\mathbb{R}^2) = \mathbb{L}_2(S_1) \otimes \mathbb{L}_2((0, \infty), r dr)$ . Decompose  $\mathbb{L}_2(S_1)$  into irreducible representations:

$$\mathbb{L}_2(S_1) = \bigoplus_{m \in \mathbb{Z}} \mathcal{D}^{(m)} = \bigoplus_{m \in \mathbb{Z}} \langle Y_m \rangle = \bigoplus_{m \in \mathbb{Z}} \langle \phi \mapsto \frac{e^{-im\phi}}{\sqrt{2\pi}} \rangle$$

Let  $\{\gamma_{mn}\}_{n \in \mathbb{N}}$  in  $\mathbb{L}_2((0, \infty), r dr)$  be an orthonormal base for each  $m \in \mathbb{Z}$ , then  $(\gamma_{mn} \otimes Y_m)(r, \phi) = \gamma_{mn}(r)Y_m(\phi)$  is an orthonormal base in  $\mathbb{L}_2(\mathbb{R}^2; r dr)$ . As a result we can expand any wavelet  $\psi \in \mathbb{L}_2(\mathbb{R}^2)$  in terms of this basis:

$$\begin{aligned} \psi(r, \phi) &= \sum_{m \in \mathbb{Z}} \sum_{n=0}^{\infty} \gamma_{mn}(r) Y_m(\phi) (\gamma_{mn} \otimes Y_m, \psi)_{\mathbb{L}_2(\mathbb{R}^2)} \\ &= \sum_{m \in \mathbb{Z}} \psi_m(r, \phi) = \sum_{m \in \mathbb{Z}} g_m(r) Y_m(\phi) \end{aligned} \tag{84}$$

By the Bochner-Hecke Theorem, see Appendix C, the Fourier Transform  $\mathcal{F}(\psi)$  of  $\psi \in \mathbb{L}_2(\mathbb{R}^2)$  is given by

$$\mathcal{F}(\psi)(\rho \cos \varphi, \rho \sin \varphi) = \sum_{m \in \mathbb{Z}} \tilde{g}_m(\rho) Y_m(\varphi),$$

with  $\tilde{g}_m \in \mathbb{L}_2(\mathbb{R}^2; r dr)$  given by  $\tilde{g}_m(\rho) = \rho^{1/2} \mathcal{H}_m[r^{1/2} g_m(r)](\rho)$ , where the unitary Hankel Transform  $\mathcal{H}_m : \mathbb{L}_2((0, \infty)) \rightarrow \mathbb{L}_2((0, \infty))$  is given by (150). Given such a wavelet  $\psi \in \mathbb{L}_2(\mathbb{R}^d)$ , the orientation score  $U_f$  can be written

$$U_f(\mathbf{b}, e^{i\theta}) = \overline{(\mathcal{R}_{e^{i\theta}} \tilde{\psi} * f)(\mathbf{b})} = \overline{(\mathcal{R}_{e^{i(\theta+\pi)}} \tilde{\psi} * f)(\mathbf{b})} = \sum_{m \in \mathbb{Z}} (-1)^m \frac{e^{-im\theta}}{\sqrt{2\pi}} (\overline{\psi_m} * f)(\mathbf{b}).$$



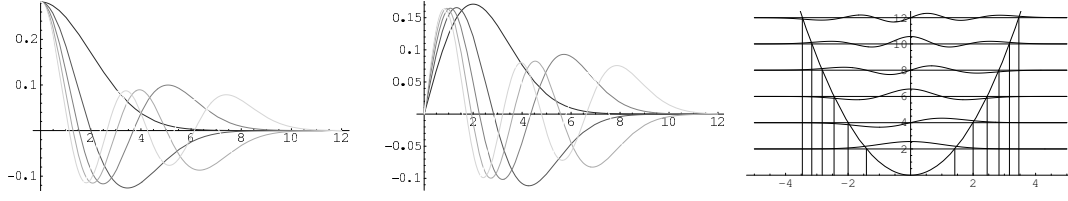


**Fig. 12** Radial basis functions  $h_n^m$ , left for  $m = 0$  and middle for  $m = 1$  and lighter gray for  $n = 0, 1, 2, \dots$ . Right, the basis functions are effectively active on  $[0, R_{mn})$ , where  $R_{mn} = \sqrt{2(2n + |m| + 1)}$ , as this equals the radius where the total energy  $E_{mn} = 2(2n + |m| + 1)$  equals the potential energy given by  $V(\mathbf{x}) = r^2$ . This is illustrated by joining the graphs of  $h_n^m$ ,  $m = 0, 1$ ,  $n = 0, 1, 2$  together with their corresponding energy levels and the graph of the potential  $V$ .

If the radial functions do not depend wildly on  $m$ , the wavelet will be directed along  $\phi = 0$ . The real part of the orientation score (constructed by a real valued wavelet which is even around  $\phi = 0$ ) reveals elongated line structures, whereas the imaginary part (constructed by a real valued wavelet which is odd around  $\phi = 0$ ) reveals elongated edge structures.

The function  $M_\psi : \mathbb{R}^2 \rightarrow \mathbb{R}$ , which by theorem 3 completely determines the well-posedness of  $f \leftrightarrow U_f$ , is now given by

$$\begin{aligned} M_\psi(\omega) &= \int_{SO(2)} |\mathcal{F}(\mathcal{R}_R \psi)(\omega)|^2 dR \\ &= \sum_{m \in \mathbb{Z}} |\tilde{g}_m(\rho)|^2, \quad \text{with } \rho = \|\omega\|. \end{aligned} \quad (85)$$

*Expansion of  $\psi$  and  $M_\psi$  in a Fourier Invariant Polar Base*

Although equation (85) is of rather simple form, it still includes the non-trivial operator  $\rho^{-1/2} \mathcal{H}_m r^{1/2}$ . This unitary operator on  $L_2((0, \infty); r dr)$  has the following complete set of orthonormal eigenfunctions  $h_n^m$ , for details see Appendix C and Figure 12,

$$h_n^m(r) = \left( \frac{2n!}{(m+n)!} \right)^{1/2} r^m e^{-r^2/2} L_n^{(m)}(r^2), \quad r > 0, m \geq 0, \quad (86)$$

For  $m < 0$  we define  $h_n^m = h_n^{|m|}$ . Therefore, we expand  $\psi$  and express  $M_\psi$  in this angular-irreducible radially Fourierinvariant basis, which are also the eigen functions of the 2D-harmonic oscillator<sup>15</sup>:

$$\begin{aligned} \psi(\mathbf{x}) &= \sum_{m \in \mathbb{Z}} \sum_{n=0}^{\infty} \alpha_m^n (Y_m \otimes h_n^m)(\phi, r), \\ \mathcal{F}[\psi](\omega) &= \sum_{m \in \mathbb{Z}} \sum_{l=0}^{\infty} (i)^{|m|} (-1)^{n+m} \alpha_m^n (Y_m \otimes h_n^m)(\varphi, \rho), \\ (\mathcal{R}_{e^{i\theta}} \psi)(\mathbf{x}) &= \sum_{m \in \mathbb{Z}} \sum_{n=0}^{\infty} \alpha_m^n e^{+im\theta} (Y_m \otimes h_n^m)(\phi, r) \\ M_\psi(\omega) &= \sum_{m=-\infty}^{\infty} \left| \sum_{n=0}^{\infty} (-1)^n \alpha_m^n h_n^m(\rho) \right|^2 \\ &= \sum_{m=-\infty}^{\infty} \sum_{n=0}^{\infty} \sum_{n'=0}^{\infty} (-1)^{n+n'} \alpha_m^n \overline{\alpha_m^{n'}} h_n^m(\rho) h_{n'}^m(\rho). \end{aligned} \quad (87)$$

Considering numerical expansions of typical local patches of elongated structures into this basis we notice that for each  $|m|$  a soft (linear) cut-off in  $n$  is required, see Figure 13.

In the remainder of this section we will construct wavelets  $\psi_{N_1, N_2}$ , with coefficients  $\alpha_m^n = 0$ , for  $|m| > N_1$  and  $n > N_2$ , for fixed  $N_1, N_2 \in \mathbb{N}$ , i.e.

$$\psi_{N_1, N_2} = \sum_{m=-N_1}^{N_1} \sum_{n=0}^{N_2} \alpha_m^n Y_m \otimes h_n^m$$

<sup>15</sup> The self-adjoint operators  $\mathcal{F}$ ,  $\mathcal{R}_R$  and the harmonic oscillator  $\Delta - \|\mathbf{x}\|^2$  commute and thereby they have a common base of eigen functions which is indeed given by  $Y_m \otimes h_n^m$ .

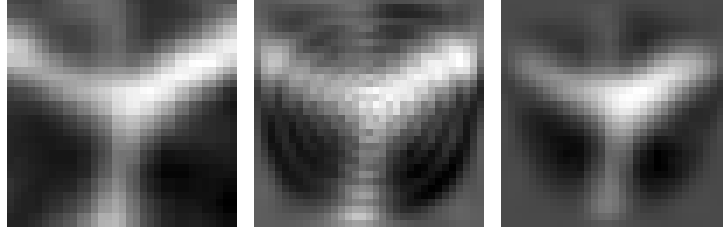


**Fig. 13** Local expansion of a  $33 \times 33$  pixel patch of an MRI-image showing a bifurcating bloodvessel in the retina. The original image is left, the reconstruction with basis function up to  $|m| = 32$  and  $n = 12$  is in the middle, and the same reconstruction linearly dampening higher  $m$  and  $n$  components is depicted on the right.

such that

$$M_{\psi_{N_1, N_2}}(\omega) = \mathcal{M}_N(\rho^2), \quad \text{with } N = N_1 + 2N_2, \rho = \|\omega\| \quad (88)$$

where we recall that  $\mathcal{M}_N(\rho^2)$  is given by (64). We consider (88) as an equation in variable  $\psi$ , determined by its coefficients  $\{\alpha_m\}_{|m|=0}^{N_1} = \{\{\alpha_m^n\}_{n=0}^{N_2}\}_{|m|=0}^{N_1}$  and thereby we obtain  $\rho = \|\omega\| > 0$ , if and only if

$$\begin{aligned} M_{\psi_{N_1, N_2}}(\omega) = \mathcal{M}_N(\rho^2) \Leftrightarrow \\ \sum_{|m|=0}^{N_1} \sum_{n=0}^{N_2} \sum_{n'=0}^{N_2} (-1)^{n+n'} \sqrt{\frac{2n!}{(n+|m|)!}} \sqrt{\frac{2n'!}{(n'+|m|)!}} \rho^{2|m|} L_n^{(m)}(\rho^2) L_{n'}^{(m)}(\rho^2) = \sum_{q=0}^N \frac{\rho^{2q}}{q!} \\ \sum_{k=0}^{2N_2} \sum_{|m|=0}^{N_1} \alpha_m^\dagger A_k^m \alpha_m \rho^{2(k+|m|)} = \sum_{q=0}^N \frac{\rho^{2q}}{q!}, \end{aligned} \quad (89)$$

where the  $(N_2 + 1) \times (N_2 + 1)$  positive symmetric matrices  $A_k^m$  equal  $[A_k^m]_{n'}^n = \sum_{j=0}^k (\mathbf{a}_j^m)_n (\mathbf{a}_{(k-j)}^m)_{n'}$ , with

$$(\mathbf{a}_k^m)_n = \begin{cases} (-1)^n \sqrt{\frac{2(n!)}{(n+|m|)!}} d_k^{m,n} = (-1)^{n+k} \sqrt{\frac{2(n!)}{(n+|m|)!}} \frac{1}{k!} \binom{n+|m|}{n-k} & \text{if } k \leq n, \\ 0 & \text{else,} \end{cases}$$

where  $d_k^{m,n} = \frac{(-1)^k}{k!} \binom{n+|m|}{n-k}$  equals the coefficient of  $\rho^{2k}$  in  $L_n^{(|m|)}(\rho^2)$ . Now in the left hand side of (88) we introduce the summation index  $q = |m| + k$  and assume  $\alpha_{-m} = \alpha_m \in \mathbb{R}^{N_2+1}$  for all  $m$ , (i.e. the wavelet is symmetric around its direction) then we obtain

$$\begin{aligned} \sum_{q=0}^N \sum_{k=\max\{0, q-N_1\}}^{2N_2} \alpha_m^T A_k^{q-k} \alpha_{q-k} \rho^{2q} &= \sum_{q=0}^N \frac{\rho^{2q}}{q!} \Leftrightarrow \\ \sum_{k=\max\{0, q-N_1\}}^{2N_2} \alpha_{q-k}^T A_k^{q-k} \alpha_{q-k} \rho^{2q} &= \frac{1}{q!}, \quad \text{for } q = 0, \dots, N, \end{aligned}$$

which are  $N + 1 = N_1 + 2N_2 + 1$  equations for  $(N_1 + 1)(N_2 + 1)$  variables  $\{\alpha_m\}_{m=0}^{N_1}$ .

**Example: The special case**  $\alpha_m^n = \alpha^m \delta_{n0}$

We take for each  $m$  the radial basis function that oscillates the least (i.e.  $n = 0$ ). We get :

$$M_\psi(\omega) = \sum_{m=0}^N |\alpha^m|^2 (h_n^m(\rho))^2 = \mathcal{M}_N(\rho^2), \quad \rho = \|\omega\|, \quad (90)$$

The (up to phase factors unique) solution  $\psi_N^0$  of (88) is now given by ( $\alpha_m = 1$  for all  $m$ )

$$\begin{aligned} \psi_N^0(\mathbf{x}) &= \sum_{m=0}^N \frac{1}{\sqrt{m!}} \rho^m e^{-\frac{\rho^2}{2}} \frac{e^{-im\phi}}{\sqrt{2\pi}} = \frac{1}{\sqrt{2\pi}} \sum_{m=0}^N \frac{(\bar{z})^m}{\sqrt{m!}} e^{-\frac{|z|^2}{2}} \\ &= \frac{1}{\sqrt{2\pi}} \sum_{m=0}^N \left(-\frac{1}{2}\right)^m \frac{\left(\frac{\partial}{\partial \bar{z}}\right)^m}{\sqrt{m!}} e^{-\frac{|z|^2}{2}} \quad z = re^{i\phi}. \end{aligned} \quad (91)$$

This series converges uniformly on compacta, but not in  $\mathbb{L}_2$ -sense. The real part of this wavelet corresponds to the wavelet first proposed by Kalitzin cf.[52] as a line detector in medical images. The imaginary part is a good edge detector. For plots of the graph of wavelet  $\psi_N$  for several values of  $N$ , see figure 14. For more plots and a comparison of the corresponding  $M_\psi$  function to the  $M_\psi$  function of some wavelet used in practice for end-point detection see Figure 16.

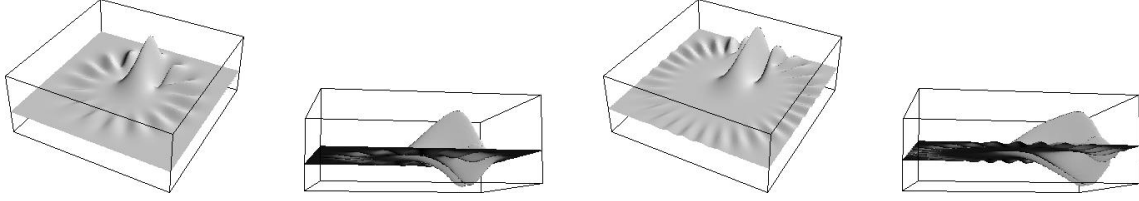


**Fig. 14** Top row: Left: 2 different viewpoint Plots of graphs  $\psi_{N=15}^0$ , Right: 2 different viewpoint Plots of graphs  $\psi_{N=30}^0$ . Notice that the kernel becomes sharper and the wiggle-ring vanishes as  $N$  increases.

#### Practical aspects regarding this example:

The cutoff index  $N$  has a practical upper bound because of sampling. If  $N$  increases the reconstruction will become better, but if we choose  $N$  too large the wavelet behaves badly along  $\phi = 0$ , see Figure 15.

We stress that  $\psi_N^0$  is essentially different than the proper wavelets constructed in the previous subsection. The simple approximative reconstruction from an orientation score  $U_f$  constructed by  $\psi_N^0$  to image  $f$ , by integration over the angles only, see (47), is not possible.

The size of the wavelet  $\psi_0^N$  can be controlled by dilation,  $\mathbf{x} \mapsto (\mathcal{D}_\sigma \psi_0^N)(\mathbf{x}) = \frac{1}{\sqrt{\sigma}} \psi_0^N(\mathbf{x}/\sigma)$ . This does effect  $\mathcal{M}_\psi$  and fixing the bending-point, like in Figure 6) is the appropriate choice of choosing  $\sigma$  (or  $t = \sigma^2$ ).

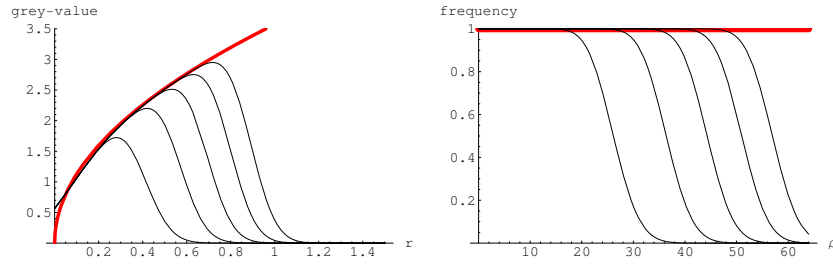


**Fig. 15** Left: The graphs of the kernel  $\psi_N^0(r, 0)$  cut off at  $N = 10, 20, 30, 40, 50$  with  $\sigma = 1/8$ . Notice that the peaks move out as  $m$  increases. The formula derived for  $\psi_\infty^0(r, \phi = 0) = (8\pi)^{1/4} \sqrt{r} + O\left(r^{-\frac{3}{2}}\right)$  see [18], is a good approximation (we included the graph of  $r \mapsto (8\pi)^{1/4} \sqrt{r}$ ). Right: The corresponding functions  $\mathcal{M}_{\psi_N^0} = \mathcal{M}_N \rightarrow 1$  as  $N \rightarrow \infty$ .

#### 3.2.2 The 3D case

We expand our wavelets in the harmonic oscillator eigenfunctions restricting ourselves to eigenfunctions which are symmetric around the  $z$ -axis: the spherical harmonics with  $m = 0$ . The wavelet then equals

$$\psi(\mathbf{x}) = \sum_{n=0}^{\infty} \sum_{l=0}^{\infty} \alpha_l^n g_n^l(r) Y_l^0(\theta, \phi), \quad \hat{\psi}(\boldsymbol{\omega}) = \sum_{n=0}^{\infty} \sum_{l=0}^{\infty} \alpha_l^n (-1)^{n+l} i^l g_n^l(\rho) Y_l^0(\vartheta, \varphi), \quad (92)$$

with  $Y_l^m$  the spherical harmonics,  $(r, \theta, \phi)$  and  $(\rho, \vartheta, \varphi)$  spherical coordinates for  $\mathbf{x}$  and  $\boldsymbol{\omega}$  respectively, i.e.

$$\begin{aligned} \mathbf{x} &= (r \cos \phi \sin \theta, r \sin \phi \sin \theta, \cos \theta), \\ \boldsymbol{\omega} &= (\rho \cos \varphi \sin \vartheta, \rho \sin \varphi \sin \vartheta, \rho \sin \varphi), \end{aligned} \quad (93)$$

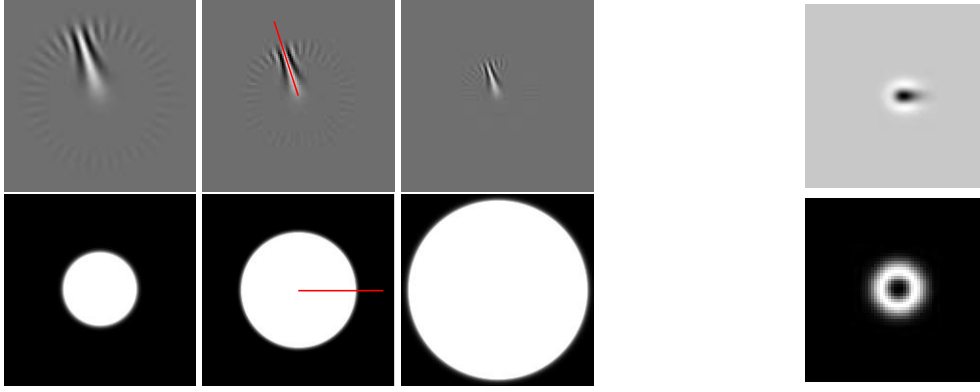


**Fig. 16** Top row: left three images; Example of rotated line detector-wavelets  $\psi_N^0$  in practice at different scales. Right image: Example of kernel developed for catheter endpoint detection. Bottom row: The corresponding functions  $M_\psi$ . Notice that the line detectors have better  $M_\psi$  and thereby induce a more stable exact reconstruction than the catheter endpoint detector (most right image). The intensity profiles along the red-lines are given in Figure 15.

and  $g_n^l$  given by

$$g_n^l(\rho) = \frac{1}{\rho} E_n^{l+\frac{1}{2}}(\rho), \text{ with } E_n^\nu(\rho) = \left( \frac{2n!}{\Gamma(n+\nu+1)} \right)^{\frac{1}{2}} \rho^{\nu+\frac{1}{2}} e^{-\frac{\rho^2}{2}} L_n^{(\nu)}(\rho^2), \quad (94)$$

where  $L_n^{(\nu)}(\rho)$  is the generalized Laguerre polynomial and  $\Gamma(z) = \int_0^\infty t^{z-1} e^{-t} dt$  denotes the usual Gamma function. We then choose the case with least radial oscillations  $\alpha_l^n = \alpha^l \delta_n^0$  up to  $l \leq L$ . If we then choose

$$\alpha_l = \sqrt{\frac{\Gamma(l+\frac{3}{2})}{\Gamma(l+1)}}, \quad (95)$$

for  $l \in \{0, \dots, L\}$  we again have that

$$M_\psi(\omega) = \int_{SO(3)} |\hat{\psi}(R^{-1}\omega)|^2 dR = M_{N=L}(\rho^2) \text{ given by (64)} \quad (96)$$

smoothly approximates 1 in the Fourier domain as  $L \rightarrow \infty$  and we get the following wavelet:

$$\psi_H(\mathbf{x}) = \sum_{l=0}^L \frac{1}{\sqrt{l!}} r^l e^{-\frac{r^2}{2}} Y_l^0(\theta, \phi). \quad (97)$$

For this wavelet we have an analytical description in both spatial and Fourier domain. This wavelet, however, again has some slight drawbacks: 1) the wavelet is not localized and has long spatial oscillations. 2) the wavelet is not centered. Both problems can be observed in Fig. 17. However, due to use of spherical harmonics for the angular part of the wavelet it is nicely steerable, and allows for steerable implementations of orientation scores, where rotations are exactly implemented (without interpolation). See Appendix D.

**Exercise 16** Show by direct computations that (96) indeed holds.

*hint: Apply Weyl's Theorem for the compact group  $SO(3)$  (or alternatively Fourier theory on  $SO(3)$ ), and switch orders of integration and summation (Fubini's theorem). For details see [18, ch:4.7.2].*

### 3.3 Analytic Approach relying on Modified Zernike Basis Expansion (for $d = 3$ )

Here we consider the case  $d = 3$  only. The case  $d = 2$  can be treated in a similar way.

The wavelets from the previous subsection had some unwanted properties such as poor spatial localization (long oscillations) and the fact that the wavelets maximum does not lie at the wavelets center. A possible explanation is that the basis used is orthogonal on the full  $\mathbb{L}_2(\mathbb{R}^3)$  space and not limited to the ball in the Fourier domain, and truncation of this basis at the Nyquist frequency could lead to oscillations.

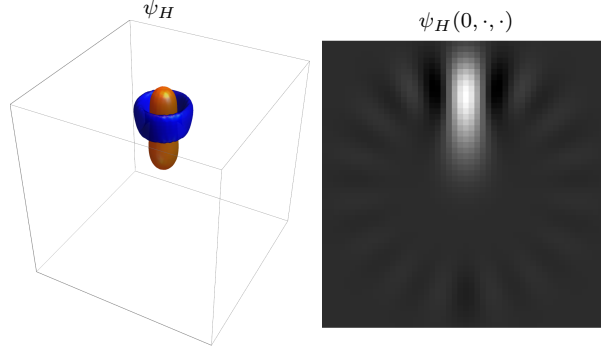


**Fig. 17** Wavelet expanded in the harmonic oscillator basis according to Eq. (97) for  $L = 20$ . *Left* 3D visualization showing one negative (blue) and one positive (orange) isocontour. *Right* Cross section of the wavelet at  $x = 0$ .

An alternative basis that is a basis for the unit-ball is the Zernike basis which we can scale later to be a basis in the Fourier domain for ball-limited images  $f \in \mathbb{L}_2^g(\mathbb{R}^3)$ , recall Eq. (5).

The 2D Zernike basis is often used in applications as optics, lithography and acoustics [1, 10], since efficient recursions can be used for calculating the basis functions and nice formulas exist for many transformations among which the Fourier transform which is expressed in jinc functions. The basis is therefore highly suitable for problems where the shape needs to be controlled in both domains such as in aberration retrieval where the basis is used in an inverse problem with an unknown aberration in the Fourier domain and optimization functional in the spatial domain.

The Zernike basis was extended to 3D in [49]. The Zernike basis is orthogonal on the unit-ball and has explicit results for the Fourier transform and is therefore more suitable for the application in mind. Here we will use the generalized Zernike functions [46], which have the added advantage of going to zero when approaching the edge of the ball.

### 3.3.1 The 3D Generalized Zernike Basis

Let  $\alpha > 0$ . Then the generalized Zernike functions are given by

$$Z_{n,l}^{m,\alpha}(\omega) = R_n^{l,\alpha}(\rho) Y_l^m(\vartheta, \varphi), \quad (98)$$

for all  $\omega = \rho \mathbf{n}(\vartheta, \varphi)$ , with  $0 \leq \rho \leq 1$ , for integer  $n, l \geq 0$  such that  $n = l + 2p$  with integer  $p \geq 0$  and  $m = -l, -l + 1, \dots, l$ , and

$$R_n^{l,\alpha}(\rho) = \rho^l (1 - \rho^2)^\alpha P_{p=\frac{n-l}{2}}^{(\alpha, l+\frac{1}{2})}(2\rho^2 - 1), \quad (99)$$

where  $P_p^{\alpha, l+\frac{1}{2}}(z)$  denotes the Jacobi polynomial with weight-function  $(1-z)^\alpha(1+z)^{l+\frac{1}{2}}$  of degree  $p$ . The generalized Zernike functions are orthogonal on the unit ball

$$\iint_{\|\omega\| \leq 1} Z_{n_1, l_1}^{m_1, \alpha}(\omega) \overline{Z_{n_2, l_2}^{m_2, \alpha}(\omega)} \frac{d\omega}{(1 - \rho^2)^\alpha} = N_{n,l}^\alpha \delta_{n_1, n_2} \delta_{m_1, m_2} \delta_{l_1, l_2}, \quad (100)$$

with  $\delta$  the Kronecker delta and with normalization factor

$$N_{n,l}^\alpha = \frac{(p+1)_\alpha}{(p+l+\frac{3}{2})_\alpha} \frac{1}{2(n+\alpha+\frac{3}{2})}, \quad (101)$$

in which  $(x)_\alpha = \frac{\Gamma(x+\alpha)}{\Gamma(x)}$  is the (generalized) Pochhammer symbol.

*Remark 13* They are called ‘generalized’ Zernike functions because of the extra factor  $(1 - \rho^2)^\alpha$  suppressing the Zernike basis functions at the boundary  $\rho = 1$ , where later we will rescale this to the boundary  $\rho = \varrho$  in the Fourier domain of our restriction to ball-limited images  $\mathbb{L}_2^g(\mathbb{R}^3)$ . Note that for  $\alpha = 0$  the functions  $Z_{n,l}^{m,0}$  correspond, up to normalization, to the standard 3D Zernike ball polynomials considered in [50, 51]

### Fourier transform

The Fourier transform of the generalized Zernike function

$$(\mathcal{F}^{-1} Z_{n,l}^{m,\alpha})(\mathbf{x}) = \iiint_{\|\boldsymbol{\omega}\| \leq 1} e^{2\pi i(\boldsymbol{\omega} \cdot \mathbf{x})} R_n^{l,\alpha}(\rho) Y_l^m(\vartheta, \varphi) d\boldsymbol{\omega} \quad (102)$$

is given by

$$(\mathcal{F}^{-1} Z_{n,l}^{m,\alpha})(\mathbf{x}) = 4\pi i^l S_{n,l}^{\alpha}(2\pi r) Y_l^m(\theta, \phi), \quad (103)$$

with  $\mathbf{x} = r \mathbf{n}(\theta, \phi)$  and

$$\begin{aligned} S_{n,l}^{\alpha}(q) &= \int_0^1 R_n^{l,\alpha}(\rho) j_l(q\rho) \rho^2 d\rho \\ &= \begin{cases} 2^\alpha (-1)^p (p+1)_\alpha \sqrt{\frac{\pi}{2q}} \frac{J_{n+\alpha+\frac{3}{2}}(q)}{q^{\alpha+1}} & \text{if } q > 0, \\ \frac{\sqrt{\pi} \Gamma(\frac{1+\alpha}{2})}{4 \Gamma(\frac{5}{2}+\alpha)} \delta_{n,0} & \text{if } q = 0. \end{cases} \end{aligned} \quad (104)$$

For integer  $\alpha \in \mathbb{N}$ , the expression for  $q > 0$  reduces to  $2^\alpha (-1)^p \frac{(p+\alpha)!}{p!} \frac{j_{n+\alpha+1}(q)}{q^{\alpha+1}}$ . For details on the computation see [46].

### Expansion of separable functions

An additional constraint for the wavelets is that they should be separable in the Fourier domain, i.e.,  $(\mathcal{F}\psi)(\boldsymbol{\omega}) = F(\boldsymbol{\omega}) = A(\mathbf{n}(\vartheta, \varphi)) \cdot B(\rho)$ . When expanding such a function in the generalized Zernike basis,

$$F(\boldsymbol{\omega}) = \sum_{n,l,m} c_{n,l}^{m,\alpha}(F) Z_{n,l}^{m,\alpha}(\boldsymbol{\omega}), \quad (105)$$

we can split the coefficients in radial coefficients and angular coefficients

$$\begin{aligned} c_{n,l}^{m,\alpha}(F) &= \frac{1}{N_{n,l}^\alpha} \iiint_{\|\boldsymbol{\omega}\| \leq 1} \overline{(Z_{n,l}^{m,\alpha}(\boldsymbol{\omega}))} F(\boldsymbol{\omega}) \frac{d\boldsymbol{\omega}}{(1-\rho^2)^\alpha} = a_l^m(A) \cdot \tilde{b}_n^{l,\alpha}(B), \\ \tilde{b}_n^{l,\alpha}(B) &:= \frac{1}{N_{n,l}^\alpha} b_n^{l,\alpha}(B). \end{aligned} \quad (106)$$

Due to orthogonality of the basis functions (98) one has

$$a_l^m(A) = \int_0^\pi \int_0^{2\pi} \overline{(Y_l^m(\vartheta, \varphi))} A(\mathbf{n}(\vartheta, \varphi)) \sin \vartheta d\vartheta d\varphi, \quad (107)$$

$$b_n^{l,\alpha}(B) = \int_0^1 B(\rho) R_n^{l,\alpha}(\rho) \frac{\rho^2 d\rho}{(1-\rho^2)^\alpha}. \quad (108)$$

The coefficients  $c_{n,l}^{m,\alpha}$  in (106) reflect the separation of  $F$  as a product of an angular and radial factor as well as a corresponding separation of the generalized Zernike basis functions in (98). In the latter, the index  $l$  appears both in the angular and radial factor. Thus we have

$$A(\mathbf{n}(\vartheta, \varphi)) = \sum_{l=0}^{\infty} \sum_{m=-l}^l a_l^m Y_l^m(\vartheta, \varphi), \quad (109)$$

while for all  $l = 0, 1, \dots$

$$B(\rho) = \sum_{n=l, l+2, \dots} \tilde{b}_n^{l,\alpha} R_n^{l,\alpha}(\rho). \quad (110)$$

For each  $l$ , the radial functions  $R_n^{l,\alpha}$  with  $n$  varying are a basis for functions defined on the interval  $[0, 1]$ . For separable functions, we expand the same radial function  $B(\rho)$  for each  $l$ , and it can be shown that there is an efficient recursion formula for the radial coefficients [46].

### 3.3.2 Wavelets

We now choose an appropriate radial and angular functions for our wavelets expressed in the Zernike basis.

### Angular function for the Zernike wavelets

For the angular functions we again choose the (truncated) spherical diffusion kernel  $A(\mathbf{n}(\vartheta, \varphi)) = G_{s_o}^{S^2}(\mathbf{n}(\vartheta, \varphi))$ , recall (69).

### Flat radial profile for all-scale transform

Recall the procedure of splitting of the lowest frequencies (49) in a vector-valued wavelet  $\underline{\psi} = (\psi_0, \psi_1)$ .

For all-scale wavelets we design a radial function for the relevant part of the wavelet  $\psi_1$  that is used in processing, and we set  $\int_{S^{d-1}} \psi_{0,\mathbf{n}} d\sigma(\mathbf{n}) = G_{s_\rho}(\rho)$ .

The radial function of  $\psi_1$  should therefore approximate  $B(\rho) = 1 - G_{s_\rho}(\rho)$  on the interval  $[0, \varrho]$  and should smoothly go to zero when approaching the edges of the interval. For the moment we set  $\varrho = 1$  and include the scaling later.

To start, we define the function

$$B_{\alpha,\beta}(\rho) = (1 - \rho^2)^\alpha \rho^\beta, \quad (111)$$

see Fig. 18a. For this function we have the following coefficients

$$b_{n=l+2p}^{l,\alpha,\beta} = \frac{\binom{\frac{\beta-1}{2}}{\frac{p}{2}}}{(2\alpha + \beta + l + 2p + 3) \binom{\frac{1}{2}(\beta+l+1)+\alpha+p}{\alpha+p}}. \quad (112)$$

To obtain a flatter function we multiply the function with a second order Taylor expansion of the reciprocal function  $\rho \mapsto (B_{\alpha,\beta}(\rho))^{-1}$  around the function maximum obtained at

$$\rho_{\max} = \left( \frac{\frac{1}{2}\beta}{\alpha + \frac{1}{2}\beta} \right)^{\frac{1}{2}}, \quad (113)$$

see Fig. 18b. Henceforth we denote the 2nd order Taylor expansion of the reciprocal basis function around  $\rho_{\max}$  by  $B_{\alpha,\beta}^{\text{rec}}(\rho)$ . The resulting function is again a sum of functions of type (111) with different values for  $\beta$ , so we can find the coefficients  $b_{n=l+2p}^{l,\alpha}$  for the flattened function. For the specific case  $\beta = 2$  we get the following flattened function

$$B_{\alpha,2}^{\text{flat}}(\rho) = B_{\alpha,2}(\rho) \cdot B_{\alpha,2}^{\text{rec}}(\rho) = (1 - \rho^2)^\alpha \rho^2 \cdot \left( 1 + \frac{(\alpha+1)^3}{2\alpha} \right) (\rho^2 - \rho_{\max}^2)^2,$$

The flattened function and its coefficients are now given by

$$B_{\alpha,2}^{\text{flat}}(\rho) = \sum_{\substack{n-l=2p, \\ l, n \geq 0}} b_n^{l,\text{flat}} R_n^{l,\alpha}(\rho) \quad \text{and} \quad b_n^{l,\text{flat}} = \sum_{i=0}^2 c_i b_n^{l,\alpha,\beta+2i}, \quad (114)$$

with  $c_i$  the coefficients before the different powers of  $\rho^2$  in the second order Taylor series of the reciprocal. These coefficients are given by

$$B_{\alpha,2}^{\text{rec}}(\rho) = \sum_{i=0}^2 c_i \rho^{2i} = c_0 + c_1 \rho^2 + c_2 \rho^4, \quad \text{with} \quad \begin{pmatrix} c_0 \\ c_1 \\ c_2 \end{pmatrix} = \begin{pmatrix} 1 + \frac{(\alpha+1)^3}{2\alpha} \rho_{\max}^4 \\ -2 \frac{(\alpha+1)^3}{2\alpha} \rho_{\max}^2 \\ \frac{(\alpha+1)^3}{2\alpha} \end{pmatrix}. \quad (115)$$

The filters from this section are summarized in the following result:

### Result 2. (Analytic 3D-wavelets in generalized Zernike basis)

Let  $\alpha > 0$  and let  $A : S^2 \rightarrow \mathbb{R}^+$  be a function mostly supported in a sharp, convex cone around the  $z$ -axis and symmetrically around the  $z$ -axis. Then  $A$  provides our wavelet  $\hat{\psi}$  in the Fourier domain by Eq. (73). The real part of  $\psi$  detects tubes, whereas the imaginary part detects edges. We choose radial function  $g(\rho) = B^{\text{flat}}(\frac{\rho}{\rho_N})$ , angular function  $A(\mathbf{n}(\vartheta, \varphi)) = G_{s_o}^{S^2}(\mathbf{n}(\vartheta, \varphi))$  and expand in the generalized Zernike basis:

$$\hat{\psi}_\alpha(\omega) = \sum_{\substack{n-l=2p, \\ l, n \geq 0}} c_{n,l}^0 R_n^{l,\alpha} \left( \frac{\rho}{\rho_N} \right) Y_l^0(\vartheta, \varphi). \quad (116)$$

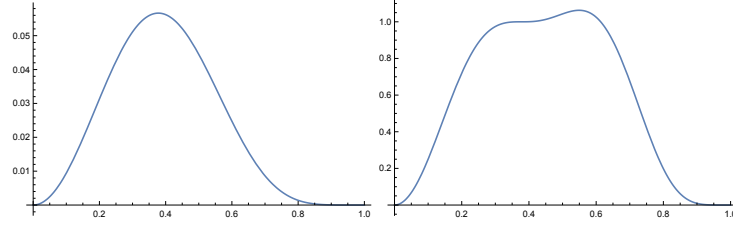


**Fig. 18** *Left* Function  $B_{\alpha=6, \beta=2}(\rho) = (1 - \rho^2)^6 \rho^2$  with maximum at  $\rho^2 = \frac{1}{7}$ . *Right* Flattened function which is obtained from  $B_{\alpha, \beta}(\rho)$  by multiplying with the 2nd order Taylor approximation of its reciprocal around the function maximum:  $B_{6,2}^{\text{flat}}(\rho) = (1 + \frac{7^3}{12}(\rho^2 - \frac{1}{7})^2)B_{6,2}(\rho)$ .

Then the coefficients  $c_{n,l}^0$  follow by expanding  $A$  in spherical harmonics and  $B_{\alpha,2}^{\text{flat}}$  in the radial Zernike polynomials, recall Eq. (109) and Eq. (110). This yields  $a_l^0$  (Eq. (76)) and  $b_{n,l}^\alpha$  (Eq. (114)) and

$$c_{n,l}^0 = \tilde{b}_{n,l}^\alpha \cdot a_l^0 \cdot \left(1 - (-1)^l + P_l(0)\right). \quad (117)$$

The spatial wavelet is given by

$$\psi_\alpha(\mathbf{x}) = \sum_{\substack{n-l=2p, \\ l, n \geq 0}} c_{n,l}^0 4\pi i^l S_{n,l}^\alpha(2\pi r \rho_N) Y_l^0(\theta, \phi), \quad (118)$$

with  $\mathbf{x} = r\mathbf{n}(\theta, \phi)$  and  $S_{n,l}^\alpha$  given by Eq. (104). This yields the rotated filters in the spatial domain:

$$\begin{aligned} \psi_{\alpha, \mathbf{n}}(\mathbf{x}) &= \sum_{\substack{n-l=2p, \\ l, n \geq 0}} \sum_{m'=-l}^l (c_{\mathbf{n}})_{n,l}^{m'} 4\pi i^l S_{n,l}^\alpha(2\pi r \rho_N) Y_l^{m'}(\theta, \phi), \\ \text{where } (c_{\mathbf{n}})_{n,l}^{m'} &= c_{n,l}^0 D_{0,m'}^l(\gamma, \beta, 0) \text{ and } \mathbf{n} = \mathbf{n}(\beta, \gamma), \end{aligned} \quad (119)$$

and with Wigner-D-matrices  $D_{m=0, m'}^l(\gamma, \beta, \alpha=0)$  are according to the conventions in Mathematica.

Since now we do have analytical expressions for the spatial filter, in contrary to the filters from Result 1, we sample them by Eq. (119). The filter is a proper wavelet with fast reconstruction property (recall Def. 13).

### 3.4 Comparison of wavelets obtained via DFT and analytical expressions using the Zernike basis

First we compare the filters obtained by sampling in the Fourier domain followed by a DFT (Section 3.1) to the filters obtained by expansion in the Zernike basis (Section 3.3). Settings were chosen such that the radial functions of both wavelets matched best and the same settings for the angular function were used. In Fig. 19 we show that the filters are very similar in shape. We see no major artifacts caused by sampling followed by an inverse DFT.

### 3.5 Quality of the 3D image reconstruction

A visual inspection of the reconstruction after the transformation and reconstruction procedure can be found in Fig. 20. As expected, a small amount of regularization is observed. We see no qualitative differences between the two reconstructions.

The series in (119) converges rapidly and the analytic wavelets in Result 2 are really close to the numerical and practical ones from Result 1. This justifies the numeric DFT-approach, and at the same time the analytic description of the kernels could be used for analytic (and steerable) processing in the orientation score. For example, for computing left-invariant derivatives.



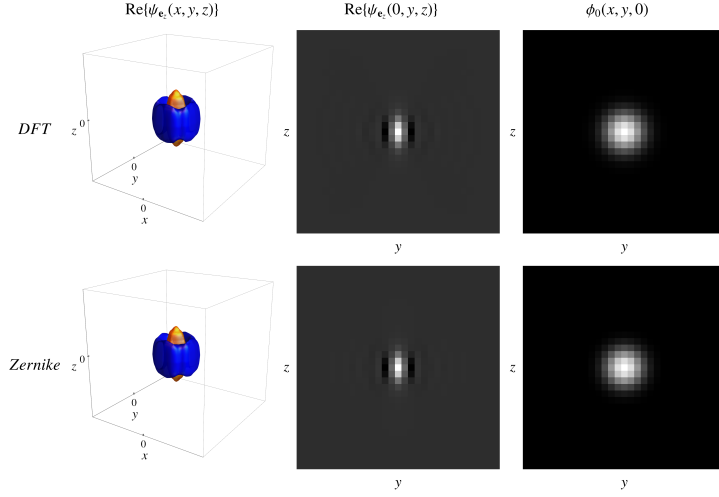


**Fig. 19** Comparison of the filters obtained by sampling in the Fourier domain and performing an inverse-DFT (Result 1 in Section 3.1) and the filters expressed in the Zernike-basis (Result 2 in Section 3.3). *Left* Iso-contour plot of the filter aligned with the x-axis showing one positive iso-contour (orange) and one negative iso-contour (blue). *Middle* Cross section of the filter for  $z = 0$ . *Right* The low-pass filter. *Top* Filters according to Result 1 with parameters  $s_\rho = \frac{1}{2}(1.9)^2$ ,  $\gamma = 0.85$ , and  $\sigma_\rho = 1.125$ . *Bottom* The filters according to Result 2 with  $\alpha = 3$  and  $\beta = 2$ . Both have  $s_o = \frac{1}{2}(0.4)^2$ ,  $L = 19$  and are evaluated on a grid of  $31 \times 31 \times 31$  voxels.

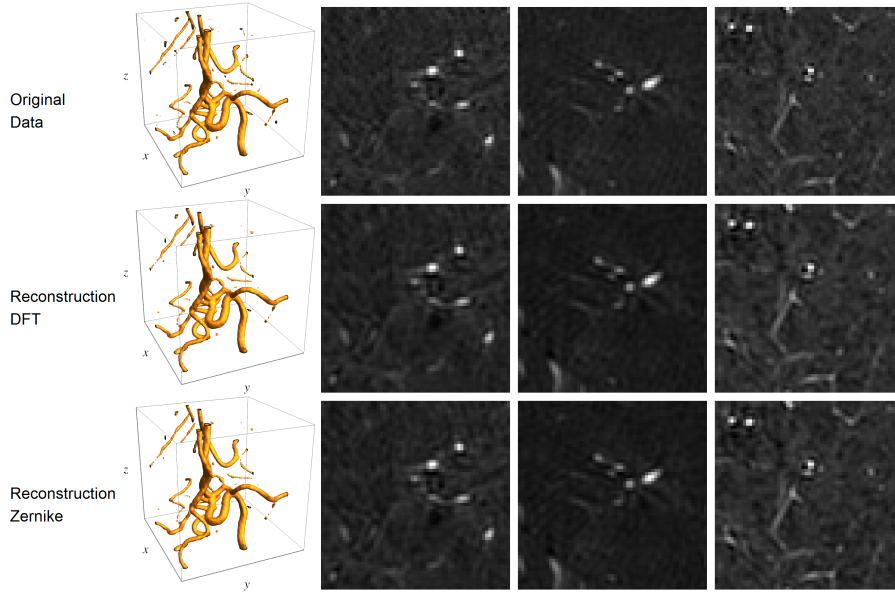


**Fig. 20** Comparison of construction and reconstruction of data A.1 using the different types of filters. In each row from left to right an iso-contour of the data and 3 slices through the middle of the data along the three principal axis. *Top*: The original data. *Middle*: the data after construction and reconstruction using the filters from Result 1. *Bottom*: the data after construction and reconstruction using the filters from Result 2.

**Exercise 17** (relating derivatives on kernels to left-invariant derivatives on scores on Lie groups) Let  $G$  be a Lie group. Let  $\psi : \mathbb{R}^d \rightarrow \mathbb{R}^+$  be smooth. Let  $\mathcal{U} : G \rightarrow B(\mathbb{L}_2(\mathbb{R}^d))$  be a group representation with which we construct the score given by

$$\mathcal{W}_\psi f(g) = (\mathcal{U}_g \psi, f)_{\mathbb{L}_2(\mathbb{R}^d)}.$$

Let  $\mathcal{R} : G \rightarrow \mathbb{B}(\mathbb{L}_2(G))$  denote the right-regular representation given by (11). Let  $\mathcal{L} : G \rightarrow \mathbb{B}(\mathbb{L}_2(G))$  denote the left-regular representation given by (12). Let us recall from the preliminaries how generators of Lie group representations were defined; see Eq. (17).

a.) Show that

$$\mathcal{W}_{\mathcal{U}_g \psi} f = \mathcal{R}_g \mathcal{W}_\psi f.$$

for all  $f \in \mathbb{L}_2(\mathbb{R}^d)$  and all  $g \in G$ .

b.) Show that

$$\mathcal{W}_{d\mathcal{U}(A)\psi} f = d\mathcal{R}(A)(\mathcal{W}_\psi f),$$

for all  $A \in T_e(G)$  and all  $f \in \mathbb{L}_2(\mathbb{R}^d)$ .

c.) Show that

$$\mathcal{L}_g \circ \mathcal{R}_h = \mathcal{R}_h \circ \mathcal{L}_g \text{ for all } g, h \in G.$$

d.) Show that

$$\mathcal{L}_g \circ d\mathcal{R}(A) = d\mathcal{R}(A) \circ \mathcal{L}_g \text{ for all } g \in G \text{ and all } A \in T_e(G).$$

e.) Set  $d = 3$  and  $G = SE(3)$ . How can the above four items (in combination with analytic representations in Result 2) be used to compute left-invariant derivatives of an orientation score?

## 4 Processing via Invertible Scores

### 4.1 Image Processing via Scores on Lie groups $G = \mathbb{R}^d \rtimes_\tau T$

Let  $G = \mathbb{R}^d \rtimes_\tau T$  be a Lie group which is the semi-direct product of the translation group with another Lie group  $T$  via an isomorphism  $\tau : T \rightarrow \text{aut}(\mathbb{R}^d)$ . Let  $\mathcal{U} : G \rightarrow B(\mathbb{L}_2(\mathbb{R}^d))$  be a unitary Lie group representation chosen to tackle the application of interest. For example the representation given by  $\mathcal{U}_{g=(\mathbf{b},t)}\psi(\mathbf{x}) = \frac{1}{\det(\tau(t))} \psi((\tau(t))^{-1})(\mathbf{x} - \mathbf{b})$ , or in particular the representation  $\mathcal{U} : SE(d) \rightarrow B(\mathbb{L}_2(\mathbb{R}^d))$  given by (4) which essentially rotates and translates images and wavelets. This could also be the Schrödinger representation of the Heisenberg group  $H(2d+1)$  onto  $B(\mathbb{L}_2(\mathbb{R}^d))$ .

Set  $\psi \in \mathbb{L}_1(\mathbb{R}^d) \cap \mathbb{L}_2(\mathbb{R}^d)$ . Then (in all cases) we consider the corresponding ‘score’ given by

$$(\mathcal{W}_\psi^G f)(g) = (\mathcal{U}_g \psi, f)_{\mathbb{L}_2(\mathbb{R}^d)} \text{ for all } g \in G, f \in H,$$

where  $\mathcal{W}_\psi^G : H \rightarrow \mathbb{C}_K^G$  with

$$H = \overline{\{\mathcal{U}_g \psi \mid g \in G\}},$$

is unitary according to Lemma 4.

Now in our primary case of interest (4) with  $G = SE(d) = \mathbb{R}^d \rtimes SO(d)$ ,  $\psi$  an (axially symmetric) proper wavelet according to Definition 13), and  $H_{NEW} = H \cap \mathbb{L}_2^g(\mathbb{R}^d)$ , the ‘rotation score of a ball-limited image’ boils down to an ‘orientation score’ of a ball-limited image, as we define

$$\mathcal{W}_\psi f(\mathbf{x}, \mathbf{n}) = (\mathcal{W}_\psi^{G=SE(d)} f)(\mathbf{x}, R_{\mathbf{n}}),$$

for all  $f \in \mathbb{L}_2^g(\mathbb{R}^d)$ , and  $(\mathbf{x}, \mathbf{n}) \in \mathbb{R}^d \rtimes S^{d-1}$ , which is independent on the choice of  $R_{\mathbf{n}} \in SO(d)$  mapping reference axis  $\mathbf{a}$  onto  $\mathbf{n}$ .

In other cases of interest, such as the Schrodinger representation of the Heisenberg group [20] the score is a Gabor transform (equipped with a relevant phase), which is very similar to a ‘musical score’ and provides an overview of all local frequencies (instead of local orientations) present in a signal.

There exists a 1-to-1 correspondence between bounded operators  $\Phi \in B(\mathbb{C}_K^G)$  on scores and bounded operators  $\Upsilon \in B(\mathbb{L}_2(\mathbb{R}^d))$  on images given by

$$\Upsilon[f] = ((\mathcal{W}_\psi^G)^* \circ \Phi \circ \mathcal{W}_\psi^G)[f], \quad f \in H \subset \mathbb{L}_2(\mathbb{R}^d). \quad (120)$$

If the closed vector subspace of images  $H$  and  $\psi$  is chosen such that the space  $\mathbb{C}_K^G$  is embedded as a normed subspace of  $\mathbb{L}_2(G)$ , this allows us to relate operators on transformed images to operators on images in a robust manner. To get a schematic view of the operations see Figure 21.

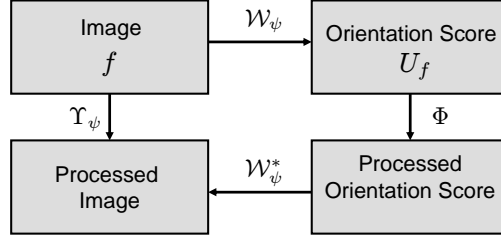


**Fig. 21** A schematic view on image processing via invertible orientation scores. According to Theorem 4,  $\Phi$  must be left-invariant and not right-invariant.

Let us consider the case  $G = SE(d)$  where  $T = SO(d)$ . By Theorem 2 the range of the unitary wavelet transform  $\mathcal{W}_\psi : \mathbb{L}_2(\mathbb{R}^2) \rightarrow \mathbb{C}_K^G$  is a subspace of  $\mathbb{L}_2(G)$ . For proper wavelets we have (approximative)  $\mathbb{L}_2$ -norm preservation when restricting to ball-limited images. For certain distributional proper wavelets  $\psi$ , see the exercise in Appendix A), one even has  $M_\psi = 1$  and this case the reproducing kernel norm truly equals the  $\mathbb{L}_2$ -norm itself.

Now this idea, can unfortunately be transferred to a limited amount of other unimodular Lie groups  $G = \mathbb{R}^d \rtimes T$  where  $T$  is a matrix group, since for a finite definition of function  $M_\psi$ , cf. [40] of

$$M_\psi(\omega) = (2\pi)^{\frac{d}{2}} \int_T |\hat{\psi}(\tau(t)^T \omega)|^2 d\mu_T(t),$$

with (left) Haar-measure  $\mu_T$ , we need compact stabilizers  $\text{Stab}_T(\omega) := \{t \in T \mid (\tau(t))^T \omega = \omega\}$ , which already rules out  $SO(m_d, n_d)$  with  $n_d, m_d \in \mathbb{N}$  such that  $n_d + m_d = d$  and  $\min\{m_d, n_d\} \geq 2$ . Even the Lorentz group case for  $d \geq 3$  is problematic as  $T = SO(d-1, 1)$  gives a rather strong condition on  $\omega$  for  $\text{Stab}_T(\omega)$  to be compact, namely the cone-condition  $(\omega^d)^2 > \sum_{i=1}^{d-1} (\omega^i)^2$ .

In general, we consider some matrix group  $T$  and a mother wavelet  $\psi$  such that  $M_\psi$  is essentially bounded on  $\mathbb{R}^d$  (in particular we think of  $T = SO(d)$ ) and in that case  $\mathcal{W}_\psi^G$  maps  $\mathbb{L}_2(\mathbb{R}^d)$  into  $\mathbb{L}_2(G)$ . Let  $\Phi : \mathbb{C}_K^G \rightarrow \mathbb{L}_2(G)$  be a bounded operator. Then its range need not be contained in  $\mathbb{C}_K^G$ , i.e. the transformed score  $\Phi(\mathcal{W}_\psi^G f)$  is a function on a Lie group and may not be equal to the score of some image....

Therefore we also consider  $\widetilde{\mathcal{W}}_\psi : \mathbb{L}_2(\mathbb{R}^d) \rightarrow \mathbb{L}_2(G)$  given by  $\widetilde{\mathcal{W}}_\psi f = \mathcal{W}_\psi^G f$ . Its adjoint is given by,

$$(\widetilde{\mathcal{W}}_\psi)^*(V) = \int_G \mathcal{U}_g \psi V(g) d\mu_G(g), \quad V \in \mathbb{L}_2(G). \quad (121)$$

The operator  $\mathbb{P}_\psi = \widetilde{\mathcal{W}}_\psi (\widetilde{\mathcal{W}}_\psi)^*$  is the orthogonal projection on the space  $\mathbb{C}_K^G$ , whereas  $\mathcal{W}_\psi^G (\mathcal{W}_\psi^G)^* = I$ . This projection can be used to decompose operator  $\Phi$ :

$$\Phi(U_f) = \mathbb{P}_\psi(\Phi(U_f)) + (I - \mathbb{P}_\psi)(\Phi(U_f)).$$

Notice that the orthogonal complement  $(\mathbb{C}_K^G)^\perp$ , which equals range  $\mathcal{R}(I - \mathbb{P}_\psi)$ , is exactly the null-space of  $(\widetilde{\mathcal{W}}_\psi)^*$  as  $\mathcal{N}((\widetilde{\mathcal{W}}_\psi)^*) = \mathcal{N}((\mathcal{W}_\psi)^*) = (\mathcal{R}(\mathcal{W}_\psi))^\perp = (\mathbb{C}_K^G)^\perp$  and so

$$[(\widetilde{\mathcal{W}}_\psi)^* \circ \Phi \circ \widetilde{\mathcal{W}}_\psi][f] = [(\widetilde{\mathcal{W}}_\psi)^* \circ \mathbb{P}_\psi \circ \Phi \circ \widetilde{\mathcal{W}}_\psi][f], \quad (122)$$

for all  $f \in \mathbb{L}_2(\mathbb{R}^2)$  and all  $\Phi \in B(\mathbb{L}_2(G))$ , so we see that the net operator associated to  $\Phi : \mathbb{L}_2(G) \rightarrow \mathbb{L}_2(G)$  is given by  $\mathbb{P}_\psi \circ \Phi : \mathbb{L}_2(G) \rightarrow \mathbb{C}_K^G$ . In the remainder of this section we present design principles for  $\mathcal{T}$ .

## 4.2 Design Principles

We now formulate a few desirable properties of  $\mathcal{T}$ , and sufficient conditions for  $\Phi$  that guarantee that  $\mathcal{T}$  meets these requirements.

1. **Covariance with respect to the group representation in the image domain:**

$$\mathcal{T} \circ \mathcal{U}_g = \mathcal{U}_g \circ \mathcal{T}, \quad \forall g \in G. \quad (123)$$

This is achieved by restricting one self to left-invariant operators  $\Phi$ . Often we will omit scaling covariance in Eq.(123) as in many imaging applications this is not natural and therefore we require (123) only to hold for the  $SE(2)$  subgroup.

2. **Left-invariant vector fields:** In order to achieve the Euclidean invariance mentioned above, we need to employ left-invariant vector fields on  $SIM(2)$  as a moving frame of reference.
3. **Nonlinearity:** The requirement that  $\mathcal{T}$  commute with  $\mathcal{U}$  immediately rules out linear operators  $\Phi$ . Here we note that  $\mathcal{U}$  can be decomposed into irreducible representations (recall for example Section 2). Now by Schur's lemma [15], any linear intertwining operator with an irreducible representations is a scalar multiple of the identity. For continuous wavelet transforms on  $G = SIM(2)$ , or Gabor transforms on  $G = H(2d+1)$  the representation used is already irreducible, which shows that linear operators acting on those types of scores are useless. For invertible orientation scores, one has that linear operators  $\Phi$  just correspond to isotropic convolutions  $\mathcal{T}$  in the spatial domain, which again would not need an orientation score decomposition. Combining linear diffusions with monotone operations on the co-domain can be simple and effective though [18].
4. **Crossing-preserving, left-invariant parabolic evolutions on  $G$ :** We consider the following two types of evolutions which include the wavelet transform as a initial condition.
5. **Crossing-preserving wavefront propagation in  $G$ :** Avoid the hassle of book-keeping of multi-valued solutions: extend the domain instead of the range of images  $f : \mathbb{R}^d \rightarrow \mathbb{R}$ .
6. **Probabilistic models for contextual, left-invariant feature propagation in the wavelet domain:** Instead of uncorrelated soft-thresholding of wavelet coefficients we aim for PDE flows that amplify the wavelet coefficients which are probabilistically coherent w.r.t. neighbouring coefficients. This coherence w.r.t. neighbouring coefficients is based on underlying stochastic processes (random walks) for multiple-scale contour enhancement.
7. **Geometric curve fitting in the score using left-invariant Finslerian, Riemannian and sub-Riemannian (SR) geometries within  $G$ :**  
Deal with both crossings and bifurcations: Turn off the reverse gear along SR geodesics in scores to avoid cusps in their spatial projections.

#### 4.3 Score Processing via Left-invariant (and not Right-invariant) Operators

Let  $G = \mathbb{R}^d \rtimes_\tau T$  denote an arbitrary unimodular Lie-group.

**Definition 17** An operator  $\Phi : \mathbb{L}_2(G) \rightarrow \mathbb{L}_2(G)$  is *left-invariant* iff

$$\Phi[\mathcal{L}_h V] = \mathcal{L}_h[\Phi V], \quad \text{for all } h \in G, \quad V \in \mathbb{L}_2(G), \quad (124)$$

where the left-regular action  $\mathcal{L}_g$  of  $g \in G$  onto  $\mathbb{L}_2(G)$  is given by  $\mathcal{L}_h V(g) = V(h^{-1}g)$ .

Recall that the right-regular action is given by  $\mathcal{R}_h V(g) = V(gh)$ .

**Theorem 4** Let  $\mathcal{U} : G \rightarrow B(\mathbb{L}_2(\mathbb{R}^d))$  be a unitary representation. Let  $\Phi : \mathbb{C}_K^G \rightarrow \mathbb{L}_2(G)$  be a bounded operator. Then the unique corresponding operator  $\mathcal{T}$  on  $H$  given by  $\mathcal{T}[f] = (\widetilde{\mathcal{W}_\psi})^* \circ \Phi \circ \widetilde{\mathcal{W}_\psi}[f]$  on the images satisfies

$$\mathcal{U}_g \circ \mathcal{T} = \mathcal{T} \circ \mathcal{U}_g \quad \text{for all } g \in G$$

if and only if the effective operator on the score  $\mathbb{P}_\psi \circ \Phi$  is left-invariant, i.e.

$$\mathcal{L}_g(\mathbb{P}_\psi \circ \Phi) = (\mathbb{P}_\psi \circ \Phi)\mathcal{L}_g, \quad \text{for all } g \in G,$$

which shows that score processing must be left-invariant. Moreover, we have

$$\Phi \circ \mathcal{R}_g = \mathcal{R}_g \circ \Phi \Rightarrow \mathcal{T}_\psi = \mathcal{T}_{\mathcal{U}_g \psi} \quad \text{for all } g \in G,$$

which shows that right-invariance is a highly undesirable property for score processing.

**Exercise 18** Consider  $G = SE(d)$ , and for the red exercises below you may restrict yourself to  $d = 2$  where  $SE(2) \cong \mathbb{R}^2 \rtimes S^1$ .

a.) Show that for all  $f \in \mathbb{L}_2(\mathbb{R}^2)$  and almost every  $\omega \in \mathbb{R}^2$  and all  $\theta \in [0, 2\pi)$  we have

$$(\mathcal{F}\widetilde{\mathcal{W}}_\psi f(\cdot, \theta))(\omega) = 2\pi \overline{\mathcal{F}\psi_\theta(\omega)} \mathcal{F}f(\omega)$$

with  $\psi_\theta(\mathbf{x}) := \psi(R_\theta^{-1}\mathbf{x})$  for  $\mathbf{x} \in \mathbb{R}^2$ ,  $\theta \in [0, 2\pi)$ .

b.) Show that for all  $f \in \mathbb{L}_2^g(\mathbb{R}^2)$  one has

$$\|\widetilde{\mathcal{W}}_\psi f\|_{\mathbb{L}_2(\mathbb{R}^2 \rtimes S^1)}^2 = (2\pi)^2 \int_{\mathbb{R}^2} M_\psi(\omega) |(\mathcal{F}f)(\omega)|^2 d\omega < \infty$$

c.) Derive the adjoint operator of  $\widetilde{W}_\psi : \mathbb{L}_2^g(\mathbb{R}^d) \rightarrow \mathbb{L}_2(G)$ , and the adjoint operator of  $W_\psi : \mathbb{L}_2^g(\mathbb{R}^d) \rightarrow \mathbb{C}_K^G$ , and explain the difference of their operator description in terms of  $M_\psi : \mathbb{R} \rightarrow \mathbb{R}^+$ .

*hint: Recall (36) and (121)*

d.) Use the unitarity of the representation  $\mathcal{U}$  to show that

$$\widetilde{\mathcal{W}}_\psi \circ \mathcal{U}_g = \mathcal{L}_g \circ \widetilde{\mathcal{W}}_\psi \text{ and } \widetilde{\mathcal{W}}_{\mathcal{U}_g \psi} = \mathcal{R}_g \circ \widetilde{\mathcal{W}}_\psi \text{ for all } g \in G$$

e.) Show that

$$\widetilde{\mathcal{W}}_\psi^* \circ \mathcal{L}_g = \mathcal{U}_g \circ \widetilde{\mathcal{W}}_\psi^* \text{ for all } g \in G.$$

f.) Prove Theorem 4.

g.) Show that  $P = \widetilde{\mathcal{W}}_\psi \circ (\widetilde{\mathcal{W}}_\psi)^* : \mathbb{L}_2(SE(d)) \rightarrow \mathbb{L}_2(SE(d))$  is the orthogonal projection onto the range of  $\widetilde{\mathcal{W}}_\psi$ , and express  $(PU)(g)$  in terms of the reproducing kernel of the space of orientation scores.

h.) Generalize the above results to  $d \in \{2, 3\}$ .

**Corollary 4** Every PDE-image processing technique involving shift-invariant partial derivatives  $\{\partial_{x^1}, \dots, \partial_{x^d}\}$  in  $\mathbb{R}^d$  admits a PDE-processing extensions involving left-invariant derivatives  $\{\mathcal{A}_1, \dots, \mathcal{A}_d, \mathcal{A}_{d+1}, \dots, \mathcal{A}_n\}$  in  $G = \mathbb{R}^d \rtimes T$  where left-invariant derivatives coincide with left-invariant vector fields given by

$$\mathcal{A}_i|_g = (L_g)_* \mathcal{A}_i = d\mathcal{R}(\mathcal{A}_i)|_g, \quad i = 1, \dots, n = \dim(G), \text{ for all } g \in G,$$

where  $*$  denotes the push-forward, and where  $d\mathcal{R}(\mathcal{A}_i)$  denote the generator (17) of the left-invariant (!), right regular representation  $\mathcal{R}$ , relative to some choice of Lie algebra basis  $\{\mathcal{A}_1, \dots, \mathcal{A}_d, \mathcal{A}_{d+1}, \dots, \mathcal{A}_n\}$ . The key advantage is that this extended PDE-processing technique allows one to deal with complex-structures requiring multiple frames per position.

**Remark 14 (practical illustrations for  $G = SE(2)$ )**

See Figure 22 and Figure fig:comp on how Theorem 4 for our case of interest  $G = SE(2)$  (where our score is an orientation score) enters practical image processing. Figure 22 illustrates the crucial identity  $\mathcal{W}_\psi \mathcal{U}_g = \mathcal{L}_g \mathcal{W}_\psi$ . However, the crucial idea that left-invariant score processing is a must from the application point of view, is best seen in Figure 23 where we compare application of left-invariant derivatives

$$\mathcal{A}_1 = \cos \theta \partial_x + \sin \theta \partial_y, \mathcal{A}_2 = -\sin \theta \partial_x + \cos \theta \partial_y, \mathcal{A}_3 = \partial_\theta, \quad (125)$$

to application of Cartesian derivatives  $\partial_x, \partial_y, \partial_\theta$  to real parts of orientation scores  $\mathcal{W}_\psi f : SE(2) \rightarrow \mathbb{C}$ .

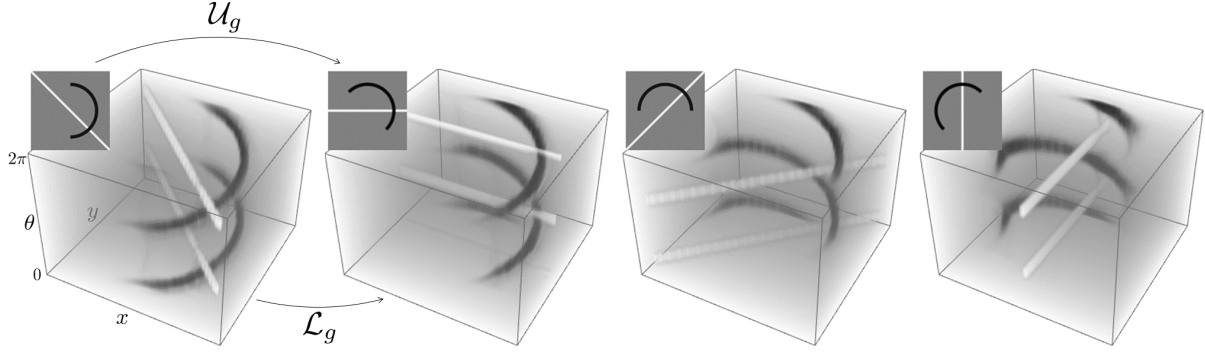


**Fig. 22** A roto-translation of the image corresponds to a shift-twist of the orientation score, both defined via a group representations of  $SE(2)$  on the image and the orientation score. Shift-twist of images and orientation scores are denoted respectively by the *left-regular* representations  $\mathcal{U}_g$  and  $\mathcal{L}_g$ . In this illustration of  $\mathcal{W}_\psi \circ \mathcal{U}_g = \mathcal{L}_g \circ \mathcal{W}_\psi$  we have set  $g = (\mathbf{0}, \theta)$ , with  $\theta$  increasing from left to right.

#### 4.4 Concise Overview of Image Processing Techniques via Invertible Orientation Scores

The orientation scores provide a full comprehensive overview of all local orientations present in the image, and this can be exploited for many processing techniques (typically where the assignment of only one orientation per spatial location is un-sufficient; i.e. where complex structures are involved, or where some notion of contextual-alignment for a more robust processing).

In the remainder of this course we shall restrict ourselves on the following type of *crossing-preserving* image processing operators in the orientation score domain:

- Nonlinear (adaptive) diffusions on invertible orientation scores for enhancement of elongated structures or denoising. Recall the bottom figures in Figure 4. See the top figure in Figure 24.
- 3D: To stress the strength of the crossing-preserving diffusions via 3D invertible orientation scores, we compare with (Gaussian) regularization acting directly in the image domain, see Figure 26. For a fair comparison diffusion times are in both cases separately optimized for contrast to noise ratios. For details see [48]. It is remarkable to see how stable vessel-widths stay under the data-adaptive diffusions for a wide range of diffusion times, see Figure 27.
- 2D: To see the basic idea of the advantage of 2D-crossing-preserving diffusion see Figure 25. For a more challenging case see the denoising example of a 2-photon microscopy containing collagen fibers at <http://bmia.bmt.tue.nl/people/RDuits/CEDOS-example.avi>.
- Linear Diffusions combined with soft-thresholding of wavelet coefficients (via non-linear transformations in co-domain) for line-amplification/enhancement. See [24, 18].
- Wavefront propagation for connectivity quantification. See [28, 11]. The basic idea is illustrated in Figure 3. This is particularly interesting in Diffusion Weighted-MRI applications (where crossings fiber structures are prominently present), see e.g. [60, 63, 58].
- Feature-analysis and biomarkers via locally adaptive frames [6, chapter 11].
- Tracking of elongated structures (vessels, fibers) in medical images. The key advantage to do tracking via orientation scores is illustrated in Figure 4 (2nd row) as crossings are manifestly disentangled in the score allowing for decent tracking without weird corners and short-cuts at complex regions such as crossings. For a first impression see also Figure 29. See Figure 28 where we track vessels in retinal images, and show advantages of our approach. For many more test-cases we refer to [6, 7, 64] and extensions that deal generically with bifurcations, cusps and spherical data see [28, 47, ?].

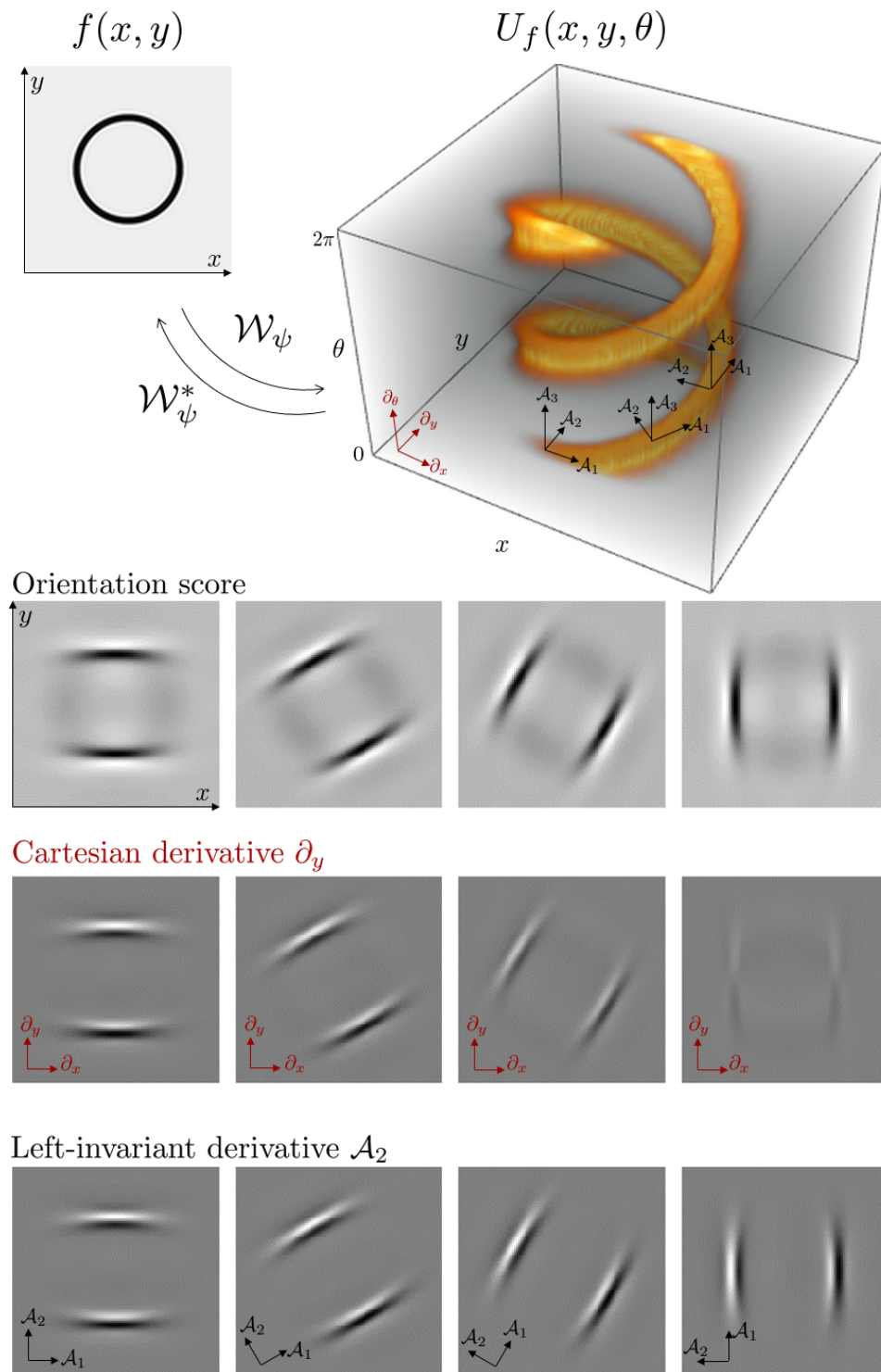
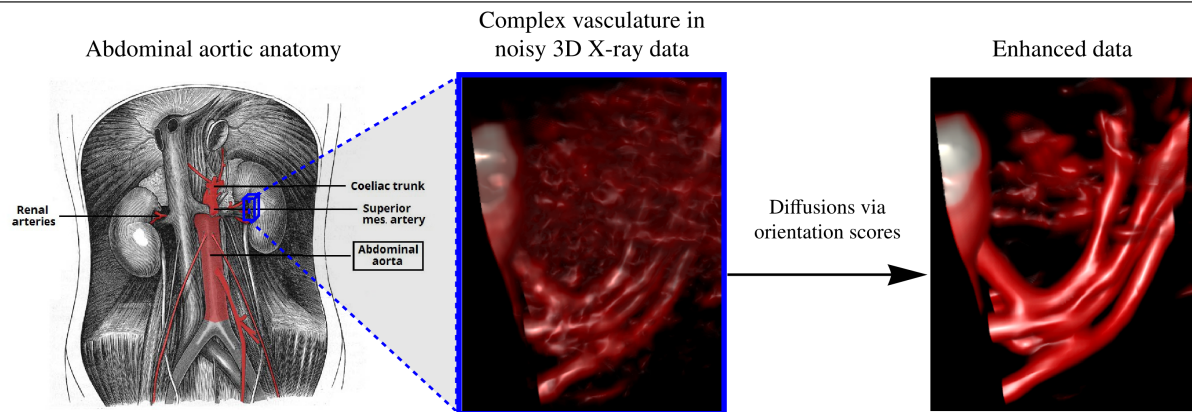


**Fig. 23** In orientation scores a left-invariant derivative frame  $\{A_1, A_2, A_3\}$  should be used instead of the axes-aligned frame  $\{\partial_x, \partial_y, \partial_\theta\}$  (illustrated in the top figure). The bottom three rows of figures compare different orientation layers of the orientation score with the Cartesian derivative  $\partial_y$  and left-invariant derivative  $\mathcal{A}_2$ . Here we see that  $\mathcal{A}_2$  is invariant under the orientation, i.e., its interpretation does not change.



### Application 1: Noise Reduction



### Application 2: Tubularity via Orientation Scores

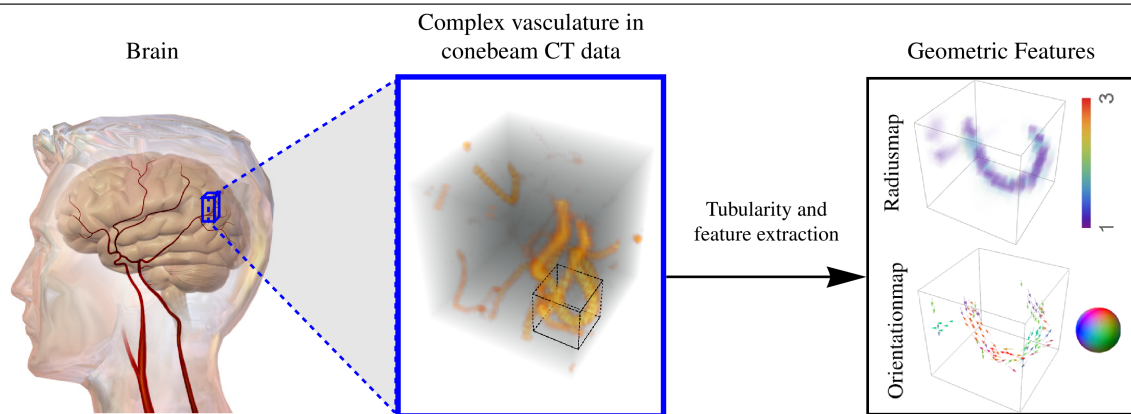


**Fig. 24** Applications of processing via 3D orientation scores. *Top:* We reduce noise in real medical image data (3D rotational Xray) of the abdomen containing renal arteries by applying diffusions via 3D orientation scores. *Bottom:* Geometrical features can be directly extracted from our tubularity measure via 3D orientation scores. We apply this method to cone beam CT data of the brain. The picture of the brain (bottom left) was used with permission from Blausen Medical inc., copyright 2016.



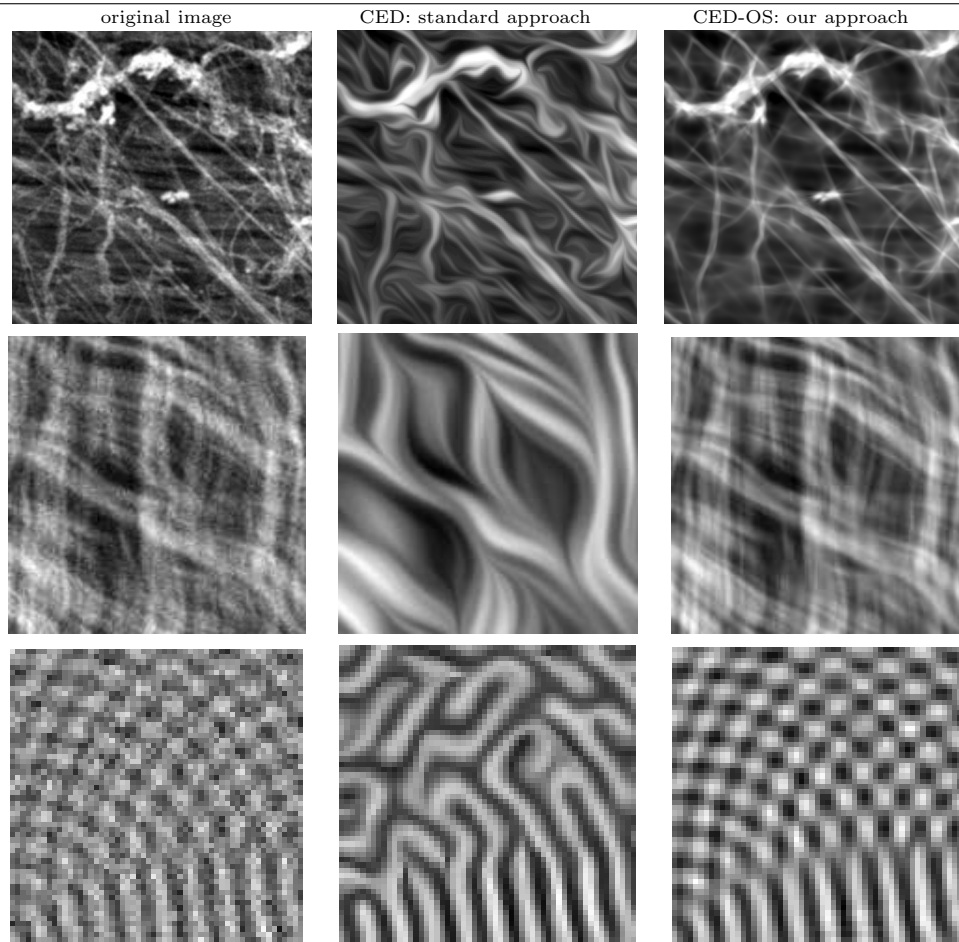


**Fig. 25** Left-invariant processing via invertible orientation scores is the right approach to generically deal with crossings and bifurcations. Left column: original images. Middle column: result of standard coherence enhancing diffusion applied directly on the image (CED), cf. [76]. Right column: coherence enhancing diffusion via invertible orientation score cf. [37, 25]. Top row: 2-photon microscopy image of bone tissue. Middle row: collagen fibers of the heart. Bottom row: artificial noisy interference pattern. CED-OS is capable of handling crossings and bifurcations, whereas CED produces spurious artifacts at such junctions.

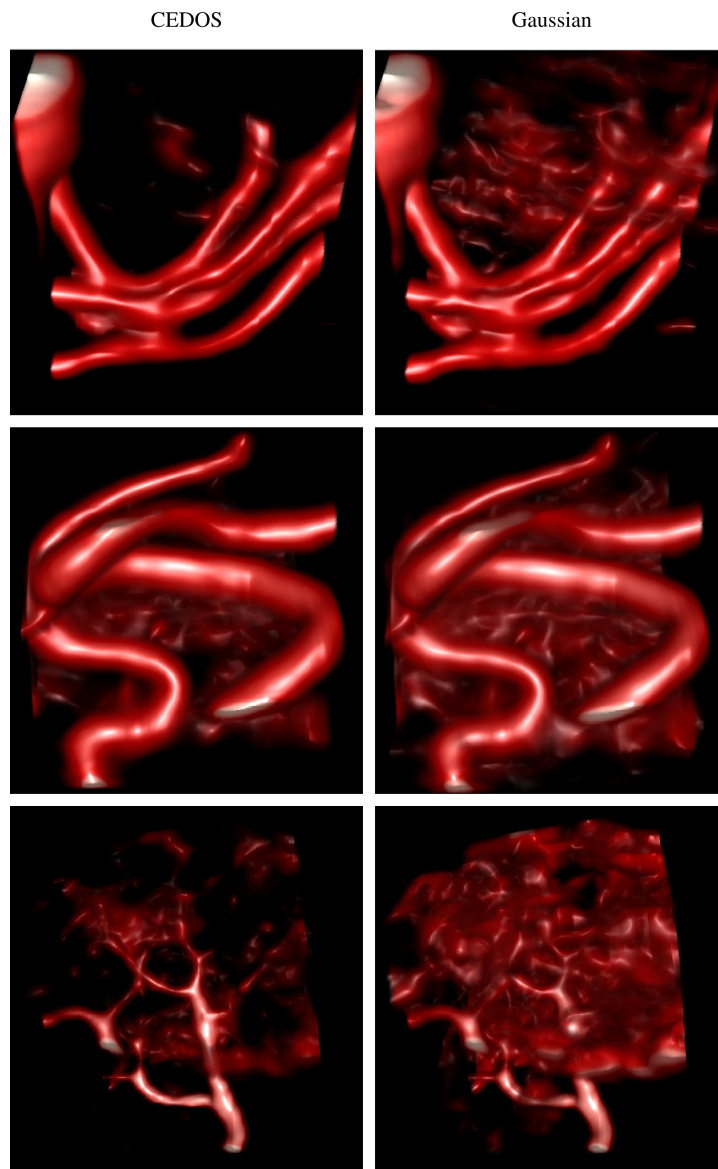


**Fig. 26** Volume rendering of the diffusion output results for 3 noisy datasets visualized in the Philips viewer [67] using default settings in both cases. For both cases we used optimized diffusion times w.r.t. contrast to noise ratios as explained in [48].

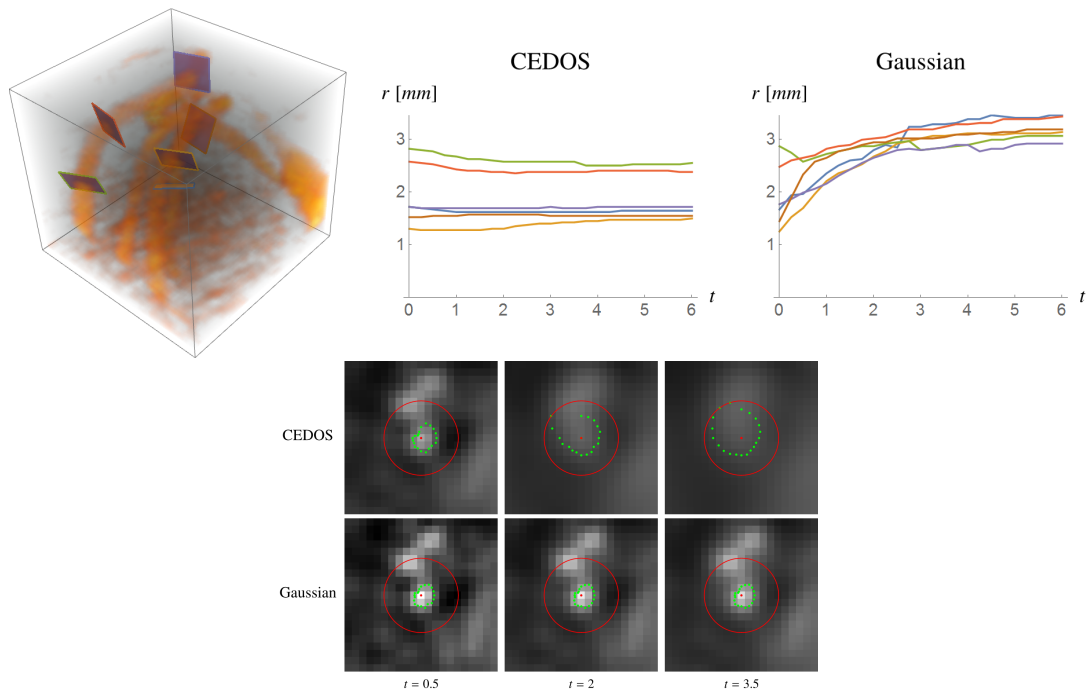


**Fig. 27** Measurement of vessel radius in vessel cross-sections after different amounts of diffusion in a noisy dataset. *Left:* 3D Visualization of the data with the select slices. *Middle:* Radii measurements for increasing diffusion time for CEDOS. *Right:* Radii measurements for increasing diffusion time for Gaussian regularization. The detected vessel width is not influenced by our regularization method which is the case for Gaussian regularization. *Bottom:* Cross-sections of one vessel for increasing diffusion time with detected vessel edge position (green points) and search area for edge detection (red circle).

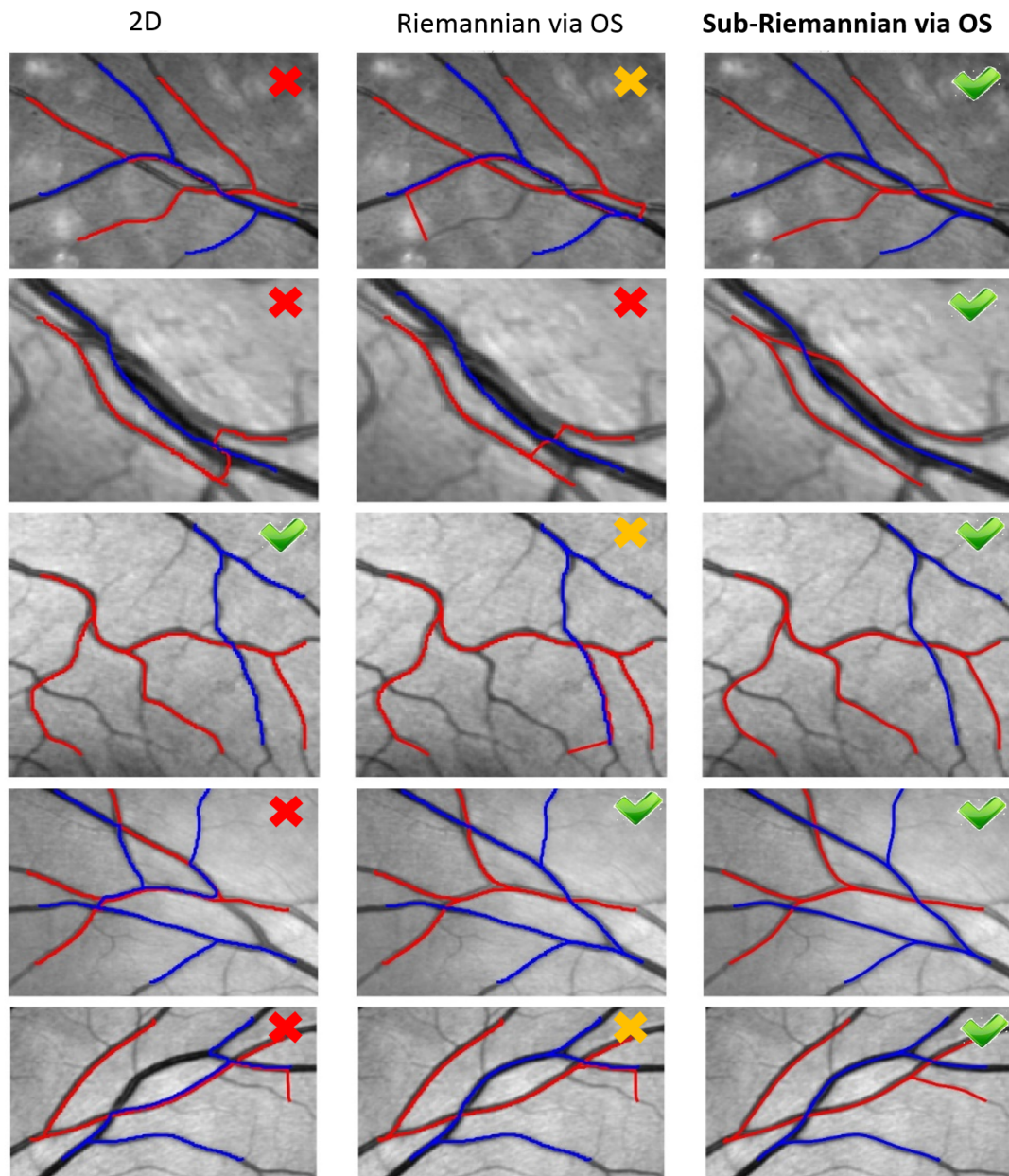


**Fig. 28** Some typical examples showing the benefit of vessel tracking in invertible orientation scores. When applying vessel-tracking along globally optimal sub-Riemannian geodesics (with infinite spatial anisotropy in the left-invariant frame of reference, recall Figure 23), in the orientation score domain results are better than the results obtained by globally optimal (isotropic) sub-Riemannian geodesics. Details will follow in part IV of this course.

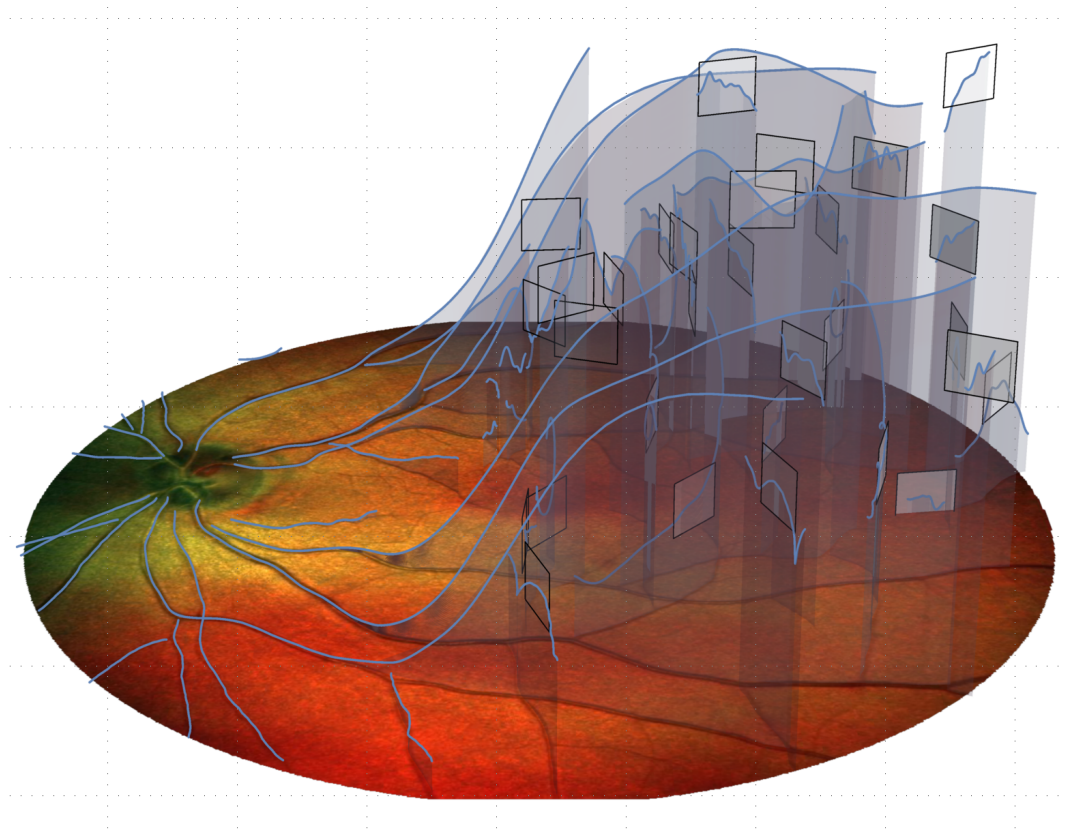


**Fig. 29** Illustration of vessel tracking in the domain of an orientation score, cf. [6].

**Exercise-Mathematica 1.** *Some steps regarding hands-on experience of invertible orientation score processing via our Lie Analysis package:*

a.) *Consider the Lie-Analysis package for latest version of Mathematica (version 11.0 or later), Wolfram Research. It can be downloaded from the web-address:*

<http://www.lieanalysis.nl/downloads>

b.) *If you are unfamiliar with Mathematica as a programming language, we recommend to first study the general Mathematica tutorial at*

<http://www.wolfram.com/language/elementary-introduction/2nd-ed/>

c.) *You can install the Lie-Analysis package in the right folder on your computer, that is in the Mathematica addons folder*

*(NB. this address is found by typing an input cell with `$UserBaseDirectory` or `$AddOnsDirectory`).*

d.) *Consider the Help-index (this is automatically included when installing the Lie Analysis package). Study the following items in the help-index:*

- `CakeWaveletStack`
- `OrientationScoreTransform`
- `InverseOrientationScoreTransform`.

e.) Study the tutorial "<http://www.lieanalysis.nl/documentation/?ref=www.lieanalysis.nl/reference/tutorial/ProcessingOn2DImages.html>"

You can run this tutorial yourself as follows:

- press F1 (this opens help index Mathematica),
- search for LieAnalysis,
- go to section tutorials,
- open processing on 2D images. Run the cells by pressing SHIFT-ENTER.

f.) Study the tutorial "<http://www.lieanalysis.nl/documentation/?ref=www.lieanalysis.nl/reference/tutorial/ProcessingOn3DImages.html>"



## A The closure of the distributional orientation score transform is an $\mathbb{L}_2$ -isometry on the whole $\mathbb{L}_2(\mathbb{R}^2)$ space.

From the condition  $\psi \in \mathbb{L}_1(\mathbb{R}^2) \cap \mathbb{L}_2(\mathbb{R}^2)$  it follows that the function  $M_\psi : \mathbb{R}^2 \rightarrow \mathbb{R}^+$  is a continuous function vanishing at infinity. In fact this follows by [66, Thm. 7.5], Fubini's theorem and compactness of  $\text{SO}(2)$ . As a result, we can not take the limit  $\varrho \rightarrow \infty$  in the definition of proper wavelets, recall Definition .

Therefore we restricted ourselves, a priori, to bandlimited/disklimited images  $f$ , bounded by a fixed radius  $\varrho > 0$  close to the Nyquist frequency induced by the sampling rate. However, as we will show in this section such a restriction to band limited images is not crucial (and in principle the invertibility of the orientation scores does not necessarily rely on finite pixel sizes).

Akin to the unitary Fourier transform  $\mathcal{F} : \mathbb{L}_2(\mathbb{R}^2) \rightarrow \mathbb{L}_2(\mathbb{R}^2)$ , whose kernel  $k(\omega, \mathbf{x}) = e^{-i\omega \cdot \mathbf{x}}$  is not square integrable, we can allow non-square integrable kernels and rely on Gelfand-Triples [78] as we will explain next.

To this end we first drop the constraint  $\psi \in \mathbb{L}_1(\mathbb{R}^d) \cap \mathbb{L}_2(\mathbb{R}^d)$  by imposing  $\psi$  to be in a dual Sobolev-space:

$$\psi \in \mathbb{H}_{-I}(\mathbb{R}^2) = \mathbb{H}_I^*(\mathbb{R}^2) = (\mathcal{D}(D_\beta))^*, \quad (126)$$

where

$$\mathbb{H}_I(\mathbb{R}^2) = \mathcal{D}(D_\beta) = \{f \in \mathbb{L}_2(\mathbb{R}^2) \mid f \text{ admits generalized derivatives s.t. } D_\beta f \in \mathbb{L}_2(\mathbb{R}^2)\} \quad (127)$$

equipped with inner product

$$(\cdot, \cdot)_{\mathbb{H}_I(\mathbb{R}^2)} = (D_\beta \cdot, D_\beta \cdot)_{\mathbb{L}_2(\mathbb{R}^2)}$$

and where  $\beta : \mathbb{R}^2 \mapsto \mathbb{R}^+$  is continuous, bounded from below, isotropic, and with differential operator

$$D_\beta = \mathcal{F}^{-1} \beta \mathcal{F}.$$

Now  $D_\beta$  is an unbounded self adjoint, positive operator with bounded inverse. This means that  $D_\beta$  defines a so-called Gelfand-Triple

$$\mathbb{H}_I(\mathbb{R}^2) \hookrightarrow \mathbb{L}_2(\mathbb{R}^2) \hookrightarrow \mathbb{H}_I^*(\mathbb{R}^2) = \mathbb{H}_{-I}(\mathbb{R}^2),$$

where  $\mathbb{H}_{-I}(\mathbb{R}^2)$  is equipped with inner product

$$(\cdot, \cdot)_{\mathbb{H}_{-I}(\mathbb{R}^2)} = (D_\beta^{-1} \cdot, D_\beta^{-1} \cdot)_{\mathbb{L}_2(\mathbb{R}^2)},$$

and where all embeddings are dense. Subsequently, we define the *distributional orientation score transform*<sup>16</sup>

$$(\mathfrak{W}_\psi f)(g) = \langle \psi, \mathcal{U}_{g^{-1}} f \rangle,$$

for all  $f \in \mathbb{H}_I(\mathbb{R}^2)$  and all  $g \in \text{SE}(2)$ , where we applied the notation  $\langle b, a \rangle = b(a)$  for functional  $b$  acting on vector  $a$ . Note that our non-distributional orientation score transform can be rewritten as

$$(\mathcal{W}_\psi f)(g) = (\mathcal{U}_g \psi, f) = (\psi, \mathcal{U}_g^* f) = (\psi, \mathcal{U}_{g^{-1}} f).$$

Under a certain condition on  $\psi$ , we show that operator  $\mathfrak{W}$  is an isometry from  $\mathbb{H}_I(\mathbb{R}^2)$  (with  $\mathbb{L}_2$ -norm) into  $\mathbb{L}_2(\text{SE}(2))$ . Therefore this operator is closable and its closure is an isometry. This brings us to the main result.

**Theorem 5** *Let  $\psi \in \mathbb{H}_{-I}(\mathbb{R}^2)$ . If  $M_{D_\beta^{-1}\psi} = \beta^{-2}$  then  $\mathfrak{W}_\psi$  maps  $\mathcal{D}(D_\beta)$  isometrically (w.r.t.  $\mathbb{L}_2$ -norm) onto a closed subspace of  $\mathbb{L}_2(\text{SE}(2))$ . Moreover, this operator is closable and its isometric closure is given by  $D_\beta \mathcal{W}_{D_\beta^{-1}\psi} : \mathbb{L}_2(\mathbb{R}^2) \rightarrow \mathbb{L}_2(\text{SE}(2))$ , where  $\mathcal{W}_{D_\beta^{-1}\psi}$  is the normed non-distributional orientation score transform, w.r.t. kernel  $D_\beta^{-1}\psi \in \mathbb{L}_2(\mathbb{R}^2)$ .*

*Proof.* First we provide some preliminaries. Operator  $D_\beta$  is an unbounded, self-adjoint (thereby closed) operator that is bounded from below, with bounded inverse. Therefore,  $\mathbb{H}_I(\mathbb{R}^2)$  is again a Hilbert space:

Let  $(f_n)_{n \in \mathbb{N}}$  be Cauchy in  $\mathbb{H}_I(\mathbb{R}^2)$ . Then  $(D_\beta f_n)_{n \in \mathbb{N}}$  is Cauchy in  $\mathbb{L}_2(\mathbb{R}^2)$ . Because  $\mathbb{L}_2(\mathbb{R}^2)$  is complete we have  $D_\beta f_n \rightarrow g$  in  $\mathbb{L}_2(\mathbb{R}^2)$ . But then, since  $D_\beta^{-1}$  is bounded,  $f_n$  is also Cauchy in  $\mathbb{L}_2(\mathbb{R}^2)$ , so  $f_n \rightarrow f$  in  $\mathbb{L}_2(\mathbb{R}^2)$  to some  $f \in \mathbb{L}_2(\mathbb{R}^2)$ . Now  $D_\beta$  is self adjoint and therefore closed so  $f \in \mathcal{D}(D_\beta)$  and  $D_\beta f = g$ . So we have  $D_\beta f_n \rightarrow D_\beta f$  in  $\mathbb{L}_2(\mathbb{R}^2)$ , so  $f_n \rightarrow f$  in  $\mathbb{H}_I(\mathbb{R}^2)$ , and  $f \in \mathbb{H}_I(\mathbb{R}^2)$ .

The space  $\mathbb{H}_{-I}(\mathbb{R}^2)$  is defined as the completion of  $\mathbb{H}_I(\mathbb{R}^2)$  and is equipped with inverse product  $(f, g)_{-I} = (D_\beta^{-1} f, D_\beta^{-1} g)_{\mathbb{L}_2(\mathbb{R}^2)}$ . This space is isomorphic to the dual space of  $\mathbb{H}_I(\mathbb{R}^2)$  under the pairing

$$\langle F, f \rangle = (R^{-1} F, R f)_{\mathbb{L}_2(\mathbb{R}^2)} \quad (128)$$

for all  $F \in \mathbb{H}_{-I}(\mathbb{R}^2)$  and  $f \in \mathbb{H}_I(\mathbb{R}^2)$ . In fact, all embeddings in  $\mathbb{H}_I(\mathbb{R}^2) \hookrightarrow \mathbb{L}_2(\mathbb{R}^2) \hookrightarrow \mathbb{H}_{-I}(\mathbb{R}^2)$  are dense. Now every  $\mathbb{L}_2(\mathbb{R}^2)$  element is the limit of  $\mathbb{H}_I(\mathbb{R}^2)$  elements, i.e.,  $\mathbb{H}_I(\mathbb{R}^2)$  is dense in  $\mathbb{L}_2(\mathbb{R}^2)$ . Furthermore, since  $D_\beta^{-1}$  is bounded we have  $\mathbb{H}_I(\mathbb{R}^2) = D_\beta^{-1}(\mathbb{L}_2(\mathbb{R}^2))$ .

<sup>16</sup> The unitary representation  $\mathcal{U}_g$  naturally extends to  $\mathbb{H}_I(\mathbb{R}^2)$  as the multiplier  $\beta$  in the Fourier domain is isotropic.

Now after these preliminaries, let us continue with the proof. Consider the associated normal orientation score transform

$$\mathcal{W}_{\tilde{\psi}} : \mathbb{L}_2(\mathbb{R}^2) \mapsto \mathbb{C}_K^{SE(2)}$$

with  $\tilde{\psi} = D_{\beta}^{-1}\psi \in \mathbb{L}_2(\mathbb{R}^2)$  associated to  $\psi \in \mathbb{H}_{-I}(\mathbb{R}^2)$ . Then by Lemma 4 and Theorem 2, this transform is unitary. This transform maps  $\mathbb{L}_2(\mathbb{R}^2)$  onto the unique reproducing kernel subspace  $\mathbb{C}_K^{SE(2)}$ , with reproducing kernel  $K(g, h) = (\mathcal{U}_g \tilde{\psi}, \mathcal{U}_h \tilde{\psi})$ . In fact we have

$$\|\mathcal{W}_{\tilde{\psi}} f\|_{\mathbb{C}_K^{SE(2)}}^2 = \int_{\mathbb{R}^2} \int_{S^1} |\mathcal{F}\mathcal{W}_{\tilde{\psi}} f(\omega, \theta)|^2 d\theta M_{\tilde{\psi}}^{-1}(\omega) d\omega = \int_{\mathbb{R}^2} |f(\mathbf{x})|^2 d\mathbf{x},$$

for all  $f \in \mathbb{L}_2(\mathbb{R}^2)$ . Therefore  $D_{\beta} \mathcal{W}_{\tilde{\psi}} = D_{\beta} \mathcal{W}_{D_{\beta}^{-1}\psi}$  is an isometry from  $\mathbb{L}_2(\mathbb{R}^2)$  into  $\mathbb{L}_2(SE(2))$  if  $M_{D_{\beta}^{-1}\psi} = \beta^{-2}$  (since  $\beta^2 M_{D_{\beta}^{-1}\psi} = 1$ ), and moreover if  $f \in \mathcal{D}(D_{\beta}) = \mathbb{H}_I(\mathbb{R}^2)$  we have (using Eq. (128) and  $D_{\beta} \mathcal{U}_g = \mathcal{U}_g D_{\beta}$ ) that

$$\begin{aligned} (D_{\beta} \mathcal{W}_{D_{\beta}^{-1}\psi} f)(g) &= (\mathcal{W}_{D_{\beta}^{-1}\psi} D_{\beta} f)(g) = (\mathcal{U}_g D_{\beta}^{-1}\psi, D_{\beta} f)_{\mathbb{L}_2(\mathbb{R}^2)} = (D_{\beta}^{-1}\psi, D_{\beta} \mathcal{U}_{g^{-1}} f)_{\mathbb{L}_2(\mathbb{R}^2)} \\ &= \langle \psi, \mathcal{U}_{g^{-1}} f \rangle = (\mathfrak{W}_{\psi} f)(g), \end{aligned}$$

for all  $g \in SE(2)$  and for all  $f \in \mathbb{H}_I(\mathbb{R}^2)$ .

Now Hilbert space  $\mathbb{H}_I(\mathbb{R}^2)$  is dense in  $\mathbb{L}_2(\mathbb{R}^2)$  and  $D_{\beta} \mathcal{W}_{D_{\beta}^{-1}\psi} \Big|_{\mathbb{H}_I(\mathbb{R}^2)} = \mathfrak{W}_{\psi}$  maps  $\mathbb{H}_I(\mathbb{R}^2)$  (with  $\mathbb{L}_2$ -norm) isometrically into  $\mathbb{L}_2(SE(2))$ . So  $\mathfrak{W}_{\psi}$  is closable as it admits the closed extension  $D_{\beta} \mathcal{W}_{D_{\beta}^{-1}\psi}$  as an extension.  $\square$

**Remark 15 (Conclusion)** By the result of the previous theorem,  $\psi \in \mathbb{H}_{-I}(\mathbb{R}^2)$  with  $M_{D_{\beta}^{-1}\psi} = \beta^{-2}$  can be called proper *distributional* wavelets. When insisting on an  $\mathbb{L}_2$ -isometric mapping between image and score one has to fall back on these kind of wavelets. In case of cake wavelets (proper wavelets of class I [18, Ch. 4.6.1]), when  $\varrho \rightarrow \infty$  such wavelets typically become oriented  $\delta$ -distributions.

In case of proper wavelets of class II [18, Ch. 4.6.2] (including the kernel proposed by Kalitzin [52]) such wavelets concentrate around and explode along the x-axis when  $N \rightarrow \infty$ , [18, Fig. 4.11 and Ch. 7.3]. In both cases the limits do not exist in  $\mathbb{L}_2$ -sense, but they do exist both pointwise and in  $\mathbb{H}_{-I}$ -sense. See also the exercise below.

We conclude from the results in this section that the orientation score framework does not insist on images to be bandlimited, and remains valid regardless the sampling size/rate.

### Exercise 19 (the distributional orientation score transform via Kalitzin's 2D-wavelet)

a.) Show that the following series converges pointwise in  $\mathbb{C}$

$$\psi(x^1, x^2) = \frac{1}{\sigma} \sum_{n=0}^{\infty} \frac{\left(\frac{z}{\sigma}\right)^n}{\sqrt{n!}} e^{-\frac{|z|^2}{\sigma^2}}, \text{ with } z = x^1 + i x^2 \in \mathbb{C}. \quad (129)$$

b.) Show that  $\mathcal{F}\psi(\omega) = \psi(R_{\frac{\pi}{2}} \omega)$  for all  $\omega = (\omega^1, \omega^2) \in \mathbb{R}^2$ .

c.) Show that the series (129) converges uniformly on compact sets, both in the spatial and Fourier domain.

d.) Show that the series does not converge in  $\mathbb{L}_2$ -sense.

e.) Show that both  $M_{\psi} = 1$  and deduce that  $\psi$  is a proper distributional wavelet, but not a proper wavelet.

f.) Show that  $\psi$  does *not* have the fast reconstruction property (recall Definition 13).

g.) Show that

$$\psi(r, 0) = (8\pi)^{\frac{1}{4}} \sqrt{r} + O(r^{-\frac{3}{2}}).$$

(hint: For details see [18, ch:7.3]).

h.) Show that  $\psi \in (\mathbb{H}^4(\mathbb{R}^2))^* = \mathbb{H}^{-4}(\mathbb{R}^2)$ .

i.) Choose  $\beta(\omega) = (1 + \|\omega\|^2)$  and show that  $\mathfrak{W}_{\psi}$  maps  $\mathbb{H}^4(\mathbb{R}^2)$  onto a closed subspace of  $\mathbb{L}_2(SE(2))$ .

j.) Determine the closure of  $\mathfrak{W}_{\psi}$ .

## B Separate Storage of the Low-frequency Components: Stability of the Vector-valued Transform

In practice we are not interested in the zero and lowest frequency components since they represent average value and global variations which appear at scales much larger than the structures of interest. We are however interested in storing this data for reconstruction. Therefore we perform an additional splitting of our proper wavelets into two parts

$$\psi = \psi_0 + \psi_1, \quad \text{with } \hat{\psi}_0 = \hat{G}_{s_{\rho}} \hat{\psi}, \quad \hat{\psi}_1 = (1 - \hat{G}_{s_{\rho}}) \hat{\psi}, \quad (130)$$



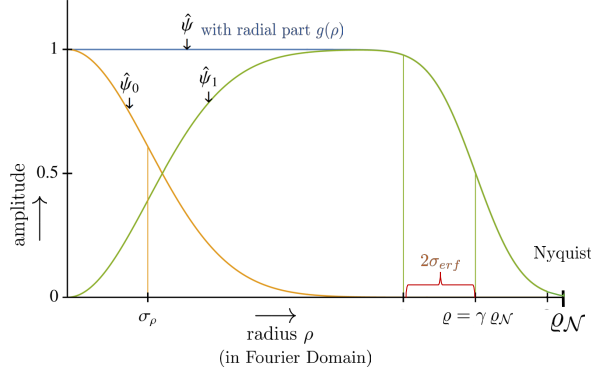


**Fig. 30** Radial function  $g$  of  $\hat{\psi}$ , see Eq. (66) and radial functions of  $\hat{\psi}_0$  and  $\hat{\psi}_1$  after splitting. The parameter  $\gamma$  controls the inflection point of the error function, here  $\gamma = 0.85$  relative to the Nyquist frequency  $\varrho_N$ . The steepness of the decay when approaching  $\rho_N$  is controlled by the parameter  $\sigma_{errf}$ . At what frequency the splitting of  $\hat{\psi}$  in  $\hat{\psi}_0$  and  $\hat{\psi}_1$  is done is controlled by parameter  $\sigma_\rho = \sqrt{2}s_\rho > 0$  which is here set relatively large for illustration purposes.

with Gaussian window in the Fourier domain given by

$$\hat{G}_{s_\rho}(\omega) = e^{-s_\rho \|\omega\|^2}, \quad (131)$$

which is one at  $\|\omega\| = 0$  and decreases when moving to higher frequencies. After splitting,  $\psi_0$  contains the average and low frequency components and  $\psi_1$  the higher frequencies relevant for further processing. In this case we construct two scores. One for the high-frequency components

$$(\mathcal{W}_{\psi_1}[f])(\mathbf{x}, \mathbf{n}) = \overline{(\psi_{1,\mathbf{n}} \star f)}(\mathbf{x}), \quad (132)$$

and one for the low-frequency components

$$(\mathcal{W}_{\psi_0}[f])(\mathbf{x}, \mathbf{n}) = \overline{(\psi_{0,\mathbf{n}} \star f)}(\mathbf{x}). \quad (133)$$

The vector transformation is then defined as

$$\underline{\mathcal{W}}_\psi[f] = (\mathcal{W}_{\psi_0}[f], \mathcal{W}_{\psi_1}[f]). \quad (134)$$

For this transformation we have exact reconstruction formula

$$\begin{aligned} f(\mathbf{x}) &= (\underline{\mathcal{W}}_\psi^{-1} \underline{\mathcal{W}}_\psi f)(\mathbf{x}) \\ &= \mathcal{F}^{-1} \left[ M_\psi^{-1} \mathcal{F} \left[ \tilde{\mathbf{x}} \mapsto \int_{S^{d-1}} (\check{\psi}_{1,\mathbf{n}} \star \mathcal{W}_{\psi_1}[f])(\cdot, \mathbf{n})(\tilde{\mathbf{x}}) + (\check{\psi}_{0,\mathbf{n}} \star \mathcal{W}_{\psi_0}[f])(\cdot, \mathbf{n})(\tilde{\mathbf{x}}) d\sigma(\mathbf{n}) \right] \right] (\mathbf{x}) \end{aligned} \quad (135)$$

with

$$M_\psi(\omega) = \int_{S^{d-1}} \left| \hat{\psi}_{0,\mathbf{n}}(\omega) \right|^2 + \left| \hat{\psi}_{1,\mathbf{n}}(\omega) \right|^2 d\sigma(\mathbf{n}) \quad (136)$$

Again,  $M_\psi$  quantifies the stability of the transformation. The additional splitting in low and high frequencies effectively causes a splitting in the radial function, see Fig. 30 where we used the relatively simple error function (66) as a point of departure.

The next lemma shows us that the stability of the vector-valued orientation score transform is maintained after performing the additional splitting.

**Lemma 7** Let  $\psi \in \mathbb{L}_2(\mathbb{R}^d) \cap \mathbb{L}_1(\mathbb{R}^d)$  such that

$$\exists_{M>0, \delta>0} \forall_{\omega \in B_\varrho} : 0 < \delta \leq M_\psi(\omega) \leq M < \infty. \quad (137)$$

holds and with  $\hat{\psi}(\omega) \in \mathbb{R}^+$ . Then the condition number of  $\mathcal{W}_\psi : \mathbb{L}_2^g(\mathbb{R}^d) \rightarrow \mathbb{L}_2^g(\mathbb{R}^d \rtimes S^{d-1})$  is given by

$$|\text{cond}(\mathcal{W}_\psi)|^2 = \|\mathcal{W}_\psi\|^2 \|\mathcal{W}_\psi^{-1}\|^2 = \frac{M}{\delta}. \quad (138)$$

The condition number of  $\underline{\mathcal{W}}_\psi : \mathbb{L}_2^g(\mathbb{R}^d) \rightarrow \mathbb{L}_2^g(\mathbb{R}^d \rtimes S^{d-1})$  obtained from  $\mathcal{W}_\psi$  by performing an additional splitting in low and high frequency components is given by

$$|\text{cond}(\underline{\mathcal{W}}_\psi)|^2 = \|\underline{\mathcal{W}}_\psi\|^2 \|\underline{\mathcal{W}}_\psi^{-1}\|^2 = \frac{2M}{\delta}, \quad (139)$$

therefore guaranteeing stability is maintained after performing the splitting.

*Proof.* First, we find the condition number of  $\mathcal{W}_\psi$  which is given by

$$|\text{cond}(\mathcal{W}_\psi)|^2 = \sup_{f \in \mathbb{L}_2^\theta(\mathbb{R}^d)} \frac{\|f\|_{\mathbb{L}_2}}{\|\mathcal{W}_\psi f\|_{\mathbb{L}_2}} \cdot \sup_{f \in \mathbb{L}_2^\theta(\mathbb{R}^d)} \frac{\|\mathcal{W}_\psi f\|_{\mathbb{L}_2}}{\|f\|_{\mathbb{L}_2}}. \quad (140)$$

For the first factor in Eq. (140) we find

$$\left( \sup_{f \in \mathbb{L}_2^\theta(\mathbb{R}^d)} \frac{\|f\|_{\mathbb{L}_2}}{\|\mathcal{W}_\psi f\|_{\mathbb{L}_2}} \right)^2 = \sup_{f \in \mathbb{L}_2^\theta(\mathbb{R}^3)} \frac{\|\mathcal{F}f\|_{\mathbb{L}_2^2}^2}{\|\mathcal{F}\mathcal{W}_\psi f\|_{\mathbb{L}_2^2}^2} = \sup_{f \in \mathbb{L}_2^\theta(\mathbb{R}^3)} \frac{\int_{\mathbb{R}^d} |\hat{f}(\omega)|^2 d\omega}{\int_{S^{d-1}} \int_{\mathbb{R}^d} |\hat{\psi}_{\mathbf{n}}(\omega)|^2 |\hat{f}(\omega)|^2 d\omega d\sigma(\mathbf{n})} = \sup_{\omega \in B_\varrho} \frac{1}{M_\psi(\omega)}, \quad (141)$$

which can be done similarly for the second factor now resulting in  $\sup_{\omega \in B_\varrho} M_\psi(\omega)$ . Then we obtain

$$|\text{cond}(\mathcal{W}_\psi)|^2 = \sup_{\omega \in B_\varrho} \frac{1}{M_\psi(\omega)} \cdot \sup_{\omega \in B_\varrho} M_\psi(\omega) = \frac{M}{\delta}. \quad (142)$$

Similarly the condition number of  $\mathcal{W}_{\underline{\psi}}$  is given by

$$|\text{cond}(\mathcal{W}_{\underline{\psi}})|^2 = \sup_{\omega \in B_\varrho} \frac{1}{M_{\underline{\psi}}(\omega)} \cdot \sup_{\omega \in B_\varrho} M_{\underline{\psi}}(\omega). \quad (143)$$

Then we express  $M_{\underline{\psi}}$  in  $M_\psi$  (keeping in mind  $\hat{\psi} \geq 0$ ) of the original wavelet

$$\begin{aligned} M_{\underline{\psi}}(\omega) &= \int_{S^{d-1}} \left| \hat{\psi}_{0,\mathbf{n}}(\omega) \right|^2 + \left| \hat{\psi}_{1,\mathbf{n}}(\omega) \right|^2 d\sigma(\mathbf{n}) \\ &= \int_{S^{d-1}} \left| \hat{\psi}_{0,\mathbf{n}}(\omega) + \hat{\psi}_{1,\mathbf{n}}(\omega) \right|^2 d\sigma(\mathbf{n}) - \int_{S^2} 2\hat{\psi}_{0,\mathbf{n}}(\omega)\hat{\psi}_{1,\mathbf{n}}(\omega) d\sigma(\mathbf{n}) = M_\psi(\omega) - I(\omega). \end{aligned} \quad (144)$$

So it remains to quantify  $I(\omega)$ . For a wavelet splitting according to (130) we have

$$\begin{aligned} I &= \int_{S^{d-1}} 2\hat{\psi}_{0,\mathbf{n}}\hat{\psi}_{1,\mathbf{n}} d\sigma(\mathbf{n}) \stackrel{(130)}{=} \int_{S^{d-1}} 2(\hat{G}_{s_\rho}\hat{\psi}_{\mathbf{n}})(1 - \hat{G}_{s_\rho})\hat{\psi}_{\mathbf{n}} d\sigma(\mathbf{n}) = 2(\hat{G}_{s_\rho}(1 - \hat{G}_{s_\rho}))M_\psi \\ &\Rightarrow \\ M_{\underline{\psi}}(\omega) &= \left( 1 - 2(\hat{G}_{s_\rho}(\omega)(1 - \hat{G}_{s_\rho}(\omega))) \right) M_\psi(\omega). \end{aligned} \quad (145)$$

And since  $\frac{1}{2} \leq 1 - 2x(1 - x) \leq 1$  for  $0 \leq x \leq 1$  we have for  $M_\psi$  satisfying (137) the following bounds on  $M_{\underline{\psi}}$ :

$$0 < \delta/2 \leq M_{\underline{\psi}}(\omega) \leq M < \infty, \quad \text{for all } \omega \in B_\varrho, \quad (146)$$

therefore guaranteeing stability after the splitting (130).  $\square$

If  $N_\psi \approx 1_{B_{0,\varrho}}$ , this vector transformation also allows for an approximate reconstruction by integration over orientations:

$$\begin{aligned} f(\mathbf{x}) &\approx \int_{S^2} \mathcal{W}_\psi[f](\mathbf{x}, \mathbf{n}) d\sigma(\mathbf{n}) \\ &= \int_{S^{d-1}} \mathcal{W}_{\psi_1}[f](\mathbf{x}, \mathbf{n}) d\sigma(\mathbf{n}) + \underbrace{\int_{S^{d-1}} \mathcal{W}_{\psi_0}[f](\mathbf{x}, \mathbf{n}) d\sigma(\mathbf{n})}_{L_{\psi_0}[f](\mathbf{x})}, \end{aligned} \quad (147)$$

and since we are only interested in processing  $\mathcal{W}_{\psi_1}[f]$  (the higher frequencies) and not  $\mathcal{W}_{\psi_0}[f]$  (the average and global variations) we do not have to separate the orientations in  $\mathcal{W}_{\psi_0}[f]$  and directly calculate  $L_{\psi_0}[f]$  via

$$L_{\psi_0}[f](\mathbf{x}) = (\overline{\phi_0} * f)(\mathbf{x}), \quad \text{with } \phi_0 = \int_{S^{d-1}} \psi_{0,\mathbf{n}} d\sigma(\mathbf{n}). \quad (148)$$

For a design with  $N_\psi = 1_{B_{0,\varrho}}$  we have

$$f(\mathbf{x}) = \int_{S^{d-1}} \mathcal{W}_{\psi_1}[f](\mathbf{x}, \mathbf{n}) d\sigma(\mathbf{n}) + (G_{s_\rho} * f)(\mathbf{x}). \quad (149)$$

## C The Bochner-Hecke Theorem and the Spectral Decomposition of the Hankel Transform

In this section we formulate the Bochner-Hecke theorem and then we present the basics that are needed in the analytic expansion of proper wavelets in the harmonic oscillator basis in Subsection 3.2. In fact, the basics in this appendix will provide analytic expressions for both  $\psi : \mathbb{R}^d \rightarrow \mathbb{C}$  and for  $M_\psi : \mathbb{R}^d \rightarrow \mathbb{R}^+$  in Subsection 3.2.

**Theorem 6** *Let  $H$  be a harmonic homogeneous polynomial of degree  $m$  in  $d$  variables. Let  $F$  be an element of  $\mathbb{L}_2((0, r); r^{d+2m-1} dr)$  then the Fourier transform of their direct product  $(r, \mathbf{x}) \mapsto F(r)H(\mathbf{x})$ , which is in  $\mathbb{L}_2(\mathbb{R}^d)$ , is given by:*

$$\begin{aligned} & (-i)^m H(\omega) \int_0^\infty (r\rho)^{\frac{d-2}{2}+m} J_{\frac{d-2}{2}+m}(\rho r) F(r) r^{d+2m-1} dr = \\ & (-i)^m H(\omega) \rho^{-(\frac{d-1}{2}+m)} \left[ \mathcal{H}_{\frac{d-2}{2}+m} r^{\frac{d-1}{2}+m} F \right](\rho), \end{aligned}$$

where  $\rho = \|\omega\|$  and the  $\mathcal{H}_{\frac{d-2}{2}+m}$  the Hankel Transform given by:

$$(\mathcal{H}_{\frac{d-2}{2}+m} \phi)(\rho) = \int_0^\infty (\rho r)^{1/2} \phi(r) J_{\frac{d-2}{2}+m}(\rho r) dr, \phi \in \mathbb{L}_2((0, \infty)). \quad (150)$$

The proof can be found in [31]pp.24-25. The Hankel Transform  $\mathcal{H}_\mu$ ,  $\mu = \frac{d-2}{2}+m$ , is a unitary map on  $\mathbb{L}_2((0, \infty), dr)$  and has a complete set of orthonormal eigen functions  $\{E_n^\mu\}$  given by

$$r \mapsto E_n^\mu(r) = \left( \frac{2n!}{\Gamma(n+\mu+1)} \right)^{\frac{1}{2}} r^{\mu+\frac{1}{2}} e^{-\frac{r^2}{2}} L_n^{(\mu)}(r^2), n = 0, 1, 2, \dots, r > 0, \quad (151)$$

where  $L_n^{(\mu)}(r)$  is the  $n$ -th generalized Laguerre polynomial of type  $\mu > -1$ ,

$$L_n^{(\mu)}(r) = \frac{r^{-\alpha} e^r}{n!} \left( \frac{d}{dr} \right)^n (e^{-r} r^{n+\mu}), r > 0,$$

with corresponding eigenvalues  $(-1)^n$ :  $(\mathcal{H}_\mu \phi) = \sum_{n=0}^\infty (-1)^n \langle E_n^\mu, \phi \rangle_{\mathbb{L}_2((0, \infty), dr)} E_n^\mu$ . The functions  $E_n^\mu$  are also eigen functions of the operator

$$-\frac{d^2}{dr^2} + r^2 + \frac{\mu^2 - \frac{1}{4}}{r^2} - 2\alpha,$$

with eigen value  $4n + 2$ , cf.[30]p.79, which coincides with the fact that the Harmonic oscillator  $\|\mathbf{x}\|^2 - \Delta$  commutes with Fourier transform.

These results gives us:

- For  $d = 2$ , we have  $\mathbb{L}_2(\mathbb{R}^2) = \mathbb{L}_2(S^1) \otimes \mathbb{L}_2((0, \infty); r dr)$  and a Fourier invariant orthonormal base is given by  $\{Y_m \otimes h_n^m\}_{m \in \mathbb{Z}, n \in \mathbb{N} \cup \{0\}}$ , where

$$h_n^m = r^{-1/2} E_n^m(r), \quad (152)$$

and  $Y_m(\phi) = \frac{1}{\sqrt{2\pi}} e^{im\phi}$ . It now follows by the Bochner-Hecke Theorem that:

$$\mathcal{F}(Y_m \otimes h_n^m) = \mathcal{F}(r^m Y_m \otimes \frac{h_n^m}{r^m}) = (-1)^n (-i)^{|m|} (Y_m \otimes h_n^m). \quad (153)$$

- For  $d = 3$ , we have  $\mathbb{L}_2(\mathbb{R}^2) = \mathbb{L}_2(S^1) \otimes \mathbb{L}_2((0, \infty); r dr)$ . All  $l$  homogeneous harmonic polynomials are spanned by  $\{\mathbf{x} \mapsto r^l Y_l^m(\theta, \phi)\}_{l=0, \dots, \infty; m=-l, \dots, l}$ . Define

$$g_n^l(r) = r^{-1} E_n^{l+\frac{1}{2}}(r), r > 0 \quad (154)$$

then  $g_n^l \in \mathbb{L}_2((0, \infty); r dr)$  are eigen functions of  $\rho^{-1} \mathcal{H}_{\frac{1}{2}+m} r^1$  with corresponding eigenvalues  $(-1)^n$ . Therefore it follows by the Bochner-Hecke Theorem that

$$\mathcal{F}(Y_l^m \otimes g_n^l) = (i)^l (-1)^{n+l} (Y_l^m \otimes g_n^l). \quad (155)$$

## D Steerable Orientation Score Transform

In this manuscript we often rely on spherical harmonic decomposition of the angular part of proper wavelets in spatial and Fourier domain. As the choice of radial basis does not affect steerable filter [39,38,65] properties, we simply write  $\{g_n^l(r)\}_{n=0}^\infty$  for a radial orthonormal basis for  $\mathbb{L}_2(\mathbb{R}^+, r^2 dr)$  associated to each  $2l + 1$ -dimensional  $SO(3)$ -irreducible subspace indexed by  $l$ . Then by the celebrated Bochner-Hecke theorem of the previous section this induces a corresponding orthonormal radial basis  $\{\tilde{g}_n^l(\rho)\}_{n=0}^\infty$  in the Fourier domain which can be obtained by a Hankel-type of transform. We expand our wavelets in spherical harmonics  $Y_l^m$  and ball-coordinates (cf. (93)) accordingly:

$$\begin{aligned} \psi(\mathbf{x}) &= \sum_{n=0}^\infty \alpha_l^n g_n^l(r) Y_l^0(\theta, \phi), \text{ with } \mathbf{x} = (r \cos \phi \sin \theta, r \cos \phi \sin \theta, r \cos \theta), \\ \hat{\psi}(\omega) &= \sum_{n=0}^\infty \alpha_l^n \tilde{g}_n^l(\rho) Y_l^0(\vartheta, \varphi), \text{ with } \omega = (\rho \cos \varphi \sin \vartheta, \rho \cos \varphi \sin \vartheta, \rho \cos \vartheta). \end{aligned} \quad (156)$$

*Remark 16* In Section 3.3, we consider the modified Zernike basis in which case  $g_n^l$  and  $\tilde{g}_n^l$  are given by respectively by (100) and (98), whereas for the harmonic oscillator basis one has  $g_n^l = i^l(-1)^{n+l}\tilde{g}_n^l$  given respectively by (92) and (94).

We obtain steerability via finite series truncation at  $n = N$  and  $l = L$ . Then we rotate the steerable kernels via the Wigner-D functions  $D_{0,m}^l(\gamma, \beta, 0) \in \mathbb{R}$  and one obtains the following steerable implementations of orientation scores:

$$\begin{aligned} U(\mathbf{x}, \mathbf{n}) &= \sum_{n=0}^N \sum_{l=0}^L \sum_{m=-l}^l \overline{\alpha_l^n D_{0,m}^l(\gamma, \beta, 0)} \cdot ((g_n^l \otimes Y_l^0) \star f)(\mathbf{x}) = \\ &= \sum_{n=0}^N \sum_{l=0}^L \sum_{m=-l}^l \overline{\alpha_l^n D_{0,m}^l(\gamma, \beta, 0)} \cdot \mathcal{F}^{-1} \left[ \overline{\tilde{g}_n^l \otimes Y_l^0} \cdot \hat{f} \right](\mathbf{x}) \end{aligned} \quad (157)$$

where  $\mathbf{n} = (\cos \gamma \sin \beta, \sin \gamma \sin \beta, \cos \beta)^T$ ,  $\star$  denotes correlation, the overline denotes complex conjugation and with function product  $(\tilde{g}_n^l \otimes Y_l^m)(\mathbf{x}) = \tilde{g}_n^l(r) Y_l^m(\theta, \phi)$ .

## References

1. R.M. Aarts, A.J.E.M. Janssen. *On-axis and far-field sound radiation from resilient flat and dome-shaped radiators*. J. Acoust. Soc. Am. **125**(3), 1444–1455, 2009.
2. S.T. Ali, J.P. Antoine, and J.P. Gazeau. *Coherent States, Wavelets and Their Generalizations*. Springer Verlag, New York, Berlin, Heidelberg, 1999.
3. J.P. Antoine. Directional wavelets revisited: Cauchy wavelets and symmetry detection in patterns. *Applied and Computational Harmonic Analysis*, 6:314–345, 1999.
4. N. Aronszajn. Theory of reproducing kernels. *Trans. A.M.S.*, 68:337–404, 1950.
5. J. August and S.W. Zucker. The curve indicator random field and markov processes. *IEEE-PAMI, Pattern Recognition and Machine Intelligence*, 25, 2003. Number 4.
6. E. Bekkers, *Retinal Image Analysis using Sub-Riemannian Geometry in SE(2)*. PhD thesis, Eindhoven University of Technology, 2017. cum laude ( $\leq 5\%$  best at TU/e), URL: [https://pure.tue.nl/ws/files/52750592/20170123\\_Bekkers.pdf](https://pure.tue.nl/ws/files/52750592/20170123_Bekkers.pdf).
7. E.J. Bekkers, R. Duits, A. Mashtakov, and G. Sanguinetti. A PDE Approach to Data-Driven Sub-Riemannian Geodesics in SE(2). *SIAM J. Imaging Sci.*, 8(4):2740–2770, 2015.
8. E.J. Bekkers, R. Duits, A. Mashtakov, and Y. L. Sachkov. Vessel Tracking via Sub-Riemannian Geodesics on  $\mathbb{R}^2 \times P^1$ . available on arxiv, accepted for publication in proc. Geometric Science of Information GSI 2017.
9. W.H. Bosking, Y. Zhang, B. Schofield, and D. Fitzpatrick. Orientation selectivity and the arrangement of horizontal connections in tree shrew striate cortex. *The Journal of Neuroscience*, 17(6):2112–2127, March 1997.
10. Brunner, T.A.: Impact of lens aberrations on optical lithography. IBM J. Res. Dev. **41**(1.2), 57–67 (1997)
11. D. Chen, *New Minimal Paths Models for Tubular Structure Extraction and Image Segmentation*. PhD thesis, Université Paris Dauphine, PSL Research University, 2016.
12. G.S. Chirikjian, and A. Kyatkin, *Engineering Applications of Noncommutative Harmonic Analysis: With Emphasis on Rotation and Motion Groups* CRC press, 2000.
13. G. Citti and A. Sarti. A Cortical Based Model of Perceptual Completion in the Roto-Translation Space. *J Math Imaging Vis*, 24(3):307–326, February 2006.
14. E. Caruyer, and C. Lenglet and G. Sapiro and R. Deriche. *Design of Multishell Sampling Schemes with Uniform Coverage in Diffusion MRI* Magn Reson Med. 69(6), p.1534–1540, 2013.
15. J. Dieudonné. *Treatise on Analysis*, Academic Press, 1977.
16. M. Duits. A functional Hilbert space approach to frame transforms and wavelet transforms. September 2004. Master thesis in Applied Analysis group at the department of Mathematics and Computer Science at the Eindhoven University of Technology.
17. M. Duits and R. Duits. A functional Hilbert space approach to the theory of wavelets. Technical report, TUE, Eindhoven, March 2004. RANA/CASA Report RANA-7-2004, available on the web: <ftp://ftp.win.tue.nl/pub/rana/rana04-07.pdf> Department of Mathematics Eindhoven University of Technology.
18. R. Duits. *Perceptual Organization in Image Analysis*. PhD thesis, Eindhoven University of Technology, Department of Biomedical Engineering, The Netherlands, 2005. A digital version is available on the web: URL: <http://www.bmi2.bmt.tue.nl/Image-Analysis/People/RDuits/THESISRDuits.pdf>.
19. R. Duits, M. Felsberg, G. Granlund, and B. M. ter Haar Romeny, “Image analysis and reconstruction using a wavelet transform constructed from a reducible representation of the Euclidean motion group,” *International Journal of Computer Vision*, vol. 79, no. 1, pp. 79–102, 2007.
20. R. Duits, H. Führ, B. Janssen, M. Bruurmijn, L. Florack, H. van Assen, Evolution equations on gabor transforms and their applications, *Applied and Computational Harmonic Analysis* 35 (2013) 483–526.
21. R. Duits, M. Duits, and M. van Almsick. Invertible orientation scores as an application of generalized wavelet theory. Technical report, TUE, Eindhoven, March 2004. Technical Report 04-04, Biomedical Image and Analysis, Department of Biomedical Engineering, Eindhoven University of Technology.
22. R. Duits, L.M.J. Florack, J. de Graaf, and B. ter Haar Romeny. On the axioms of scale space theory. *Journal of Mathematical Imaging and Vision*, 20:267–298, May 2004.
23. R. Duits, M. van Almsick, M. Duits, E. Franken, and L.M.J. Florack. Image processing via shift-twist invariant operations on orientation bundle functions. In Niemann Zhuravlev et al. Geppener, Gurevich, editor, *7th International Conference on Pattern Recognition and Image Analysis: New Information Technologies*, pages 193–196, St.Petersburg, October 2004. Extended version is to appear in special issue of the International Journal for Pattern Recognition and Image Analysis MAIK.

24. R.Duits, E.Franken. Left-invariant parabolic evolutions on  $SE(2)$  and contour enhancement via invertible orientation scores. part I: linear left-invariant diffusion equations on  $SE(2)$ . *Q APPL MATH*, **68**, 293–331, 2010.
25. R.Duits, E.Franken. Left-invariant parabolic evolutions on  $SE(2)$  and contour enhancement via invertible orientation scores. part II: Non-linear left-invariant diffusions on invertible orientation score. *Q APPL MATH*, **68**, 293–331, 2010.
26. R.Duits, E.Franken. Line enhancement and completion via left invariant scale spaces on  $SE(2)$ , LNCS 5576, SSVM 2009, p.795–807, 2009.
27. R. Duits and E. M. Franken. Left-invariant diffusions on the space of positions and orientations and their application to crossing-preserving smoothing of HARDI images. *IJCV* vol. 92, pp. 231–264, 2011.
28. R. Duits, S. Meesters, J. Mirebeau, J. Portegies, *Optimal paths for variants of the 2d and 3d Reeds-Shepp car with applications in image analysis*, (*arXiv:1612.06137*), submitted to JMIV 2017.
29. N. Dungey, A. F. M. ter Elst, and D. W. Robinson. *Analysis on Lie groups with polynomial growth*, volume 214. Birkhauser-Progress in Mathematics, Boston, 2003.
30. S.J.L. Eijndhoven and J. de Graaf. Some results on hankel invariant distribution spaces. *Proceedings of the Koninklijke Akademie van Wetenschappen, Series A*, 86(1):77–87, 1982.
31. J. Faraut and K. Harzallah. *Deux cours d'analyse harmonique*. Birkhaeuser, Tunis, 1984.
32. M. Felsberg, P.-E. Forssén, and H. Scharr. Efficient robust smoothing of low-level signal features. Technical Report LiTH-ISY-R-2619, SE-581 83 Linköping, Sweden, August 2004.
33. M. Felsberg, P.-E. Forssén, and H. Scharr. Channel smoothing: Efficient robust smoothing of low-level signal features. *IEEE Transactions on Pattern Analysis and Machine Intelligence*, 2005. accepted.
34. L. M. J. Florack. *Image Structure*. Kluwer Academic Publishers, Dordrecht, The Netherlands, 1997.
35. P.-E. Forssén and G. H. Granlund. Sparse feature maps in a scale hierarchy. In G. Sommer and Y.Y. Zeevi, editors, *Proc. Int. Workshop on Algebraic Frames for the Perception-Action Cycle*, volume 1888 of *Lecture Notes in Computer Science*, Kiel, Germany, September 2000. Springer, Heidelberg.
36. P.E. Forssen. *Low and Medium Level Vision using Channel Representations*. PhD thesis, Linköping University, Dept. EE, Linköping, Sweden, March 2004.
37. E.M.Franken and R.Duits. *Crossing-Preserving Coherence-Enhancing Diffusion via Invertible Orientation Scores* *IJCV*(85), p.253-278, 2009.
38. E. M. Franken, *Enhancement of Crossing Elongated Structures in Images*. PhD thesis, Eindhoven University of Technology, Department of Biomedical Engineering, Eindhoven, The Netherlands, 2008. <http://www.bmia.bmt.tue.nl/people/EFranken/PhDThesisErikFranken.pdf>.
39. Freeman, W.T., Adelson, E.H.: The design and use of steerable filters. *IEEE Trans. Pattern Anal. Mach. Intell* **13**(9), 891–906, 1991.
40. H. Führ. *Abstract Harmonic Analysis of Continuous Wavelet Transforms* Springer Heidelberg-New York, 2005.
41. M. van Ginkel. *Image Analysis using Orientation Space based on Steerable Filters*. PhD thesis, Delft University of Technology, Delft, Netherlands, October 2002.
42. D. Prandi, U. Boscaín and J.P. Gauthier. Image Processing in the semidiscrete group of rototranslations. Conference Geometric Science of Information, GSI, LNCS 9389, pp.627–634, 2015
43. G.H. Granlund. An associative perception-action structure using a localized space variant information representation. In *Proceedings of Algebraic Frames for the Perception-Action Cycle (AFPAC)*, Kiel, Germany, September 2000. Also as Technical Report LiTH-ISY-R-2255.
44. A. Grossmann, J. Morlet, and T. Paul. Integral transforms associated to square integrable representations. *J.Math.Phys.*, 26:2473–2479, 1985.
45. C. J. Isham and J. R. Klauder. Coherent states for  $n$ -dimensional euclidean groups  $e(n)$  and their application. *Journal of Mathematical Physics*, 32(3):607–620, March 1991.
46. A.J.E.M. Janssen. Generalized 3D Zernike functions for analytic construction of band-limited line-detecting wavelets. arXiv 2015.
47. A. Mashtakov, R. Duits, Yu Sachkov, E. J. Bekkers, and I. Beschastnyi. Tracking of Lines in Spherical Images via Sub-Riemannian Geodesics in  $SO(3)$ . *J Math Imaging Vis*, pages 1–26, February 2017.
48. M.H.J. Janssen, A.J.E.M. Janssen, J. Olivan Bescos, and R. Duits, Design and Processing of Invertible Orientation Scores of 3D Images for Enhancement of Complex Vasculature 60(9),p.1427–1458, JMIV 2018. <http://bmia.bmt.tue.nl/people/RDuits/CEDUS-3D.pdf>.
49. A.Louis. Orthogonal Function Series Expansions and the Null Space of the Radon Transform. *SIAM J. Math. Anal.* **15**(3), 621–633, 1984.
50. H. Liu, B.K. Poon, A.J.E.M. Janssen and P.H.Zwart. Computation of fluctuating scattering profiles via three-dimensional Zernike Polynomials. *Acta Crystallographica A* **68**, 561–567, 2012.
51. R.J. Mathar. Zernike basis to Cartesian transformations. *Serb. Asrtion*. J. 179,
52. S. N. Kalitzin, B. M. ter Haar Romeny, and M. A. Viergever. Invertible apertured orientation filters in image analysis. *International Journal of Computer Vision*, 31(2/3):145–158, April 1999.
53. T. S. Lee. Image representation using 2d gabor wavelets. *IEEE-Transactions on Pattern Analysis and Machine Intelligence*, 18(10):959–971, 1996.
54. A.K. Louis, P. Maass, and A. Rieder. *Wavelets, Theory and Applications*. Wiley, New York, 1997.
55. G.W. Mackey. Imprimitivity for representations of locally compact groups *Proc. N.A.S.* 35: 537–545, 1949.
56. S. Mallat, *A Wavelet Tour to Signal and Image Processing* Academic Press, 1999.
57. F.J.L. Martens. *Spaces of analytic functions on inductive/projective limits of Hilbert Spaces*. PhD thesis, University of Technology Eindhoven, Department of Mathematics and Computing Science, Eindhoven, The Netherlands, 1988. This PHD thesis is available on the webpages of the Technische Universiteit Eindhoven. Webpage in 2004: <http://alexandria.tue.nl/extra3/proefschrift/PRF6A/8810117.pdf>.
58. S. Meesters, P. Ossenkop, L. Wagner, O. Schijns, P. Boon, L.M.J. Florack, A. Vilanova, R. Duits. Stability metrics for optic radiation tractography: Towards damage prediction after resective surgery *Journal of Neuroscience Methods* (288), pp.34–44, 2017

59. D. Mumford. Elastica and computer vision. *Algebraic Geometry and Its Applications. Springer-Verlag*, pages 491–506, 1994.
60. M. Péchaud, M. Descoteaux, and R. Keriven. Brain connectivity using geodesics in HARDI. *Med Image Comput Assist Interv*, 12(Pt 2):482–489, 2009.
61. J. Petitot. Neurogéométrie de la vision - Modeles mathématiques et physiques des architectures fonctionelles. Les Éditions de l'École Polytechnique 2008.
62. J. Petitot. The neurogeometry of pinwheels as a sub-Riemannian contact structure. *Journal of Physiology-Paris*, 97(2–3):265–309, March 2003.
63. J.M. Portegies, R.H.J.Fick, G.R.Sanguinetti, G.Girard, S.P.L.Meesters and R.Duits. Improving Fiber Alignment in HARDI by Combining Contextual PDE Flow with Constrained Spherical Deconvolution PLoSOne Magnetic Resonance Imaging, DOI: 10.1371/journal.pone.0138122, 2015.
64. G.R. Sanguinetti, E.J. Bekkers, R. Duits, M.H.J. Janssen, A. Mashtakov, and J-M. Mirebeau. Sub-Riemannian Fast Marching in SE(2). In *Progress in Pattern Recognition, Image Analysis, Computer Vision, and Applications*, number 9423 in Lecture Notes in Computer Science, pages 366–374. Springer International Publishing, 2015. DOI: 10.1007/978-3-319-25751-8\_44.
65. Reisert, M.: Group Integration Techniques in Pattern Analysis - A Kernel View. Ph.D. thesis, Albert-Ludwigs-University, 2008.
66. W. Rudin *Functional Analysis*, Mc-Graw Hill Science, 1973.
67. Ruijters, D., Vilanova, A.: Optimizing GPU volume rendering. *J. WSCG* **14**(1-3), 9–16, 2006.
68. W. Schempp and B. Dresler Einführung in die Harmonische Analyse. *B.G.Teubner, Stuttgart, 1980*.
69. U. Sharma and R. Duits, Left-invariant evolutions of wavelet transforms on the similitude group, *ACHA*, vol. 39, pp. 110–137, 2015.
70. L. Siffre, *Rigid-Motion Scattering for Image Classification*. PhD thesis, Ecole Polytechnique, CMAP, Paris, 2014.
71. M. Sugiura. *Unitary representations and harmonic analysis*. North-Holland Mathematical Library, 44., Amsterdam, Kodansha, Tokyo, second edition, 1990.
72. K.K. Thornber and L.R. Williams. Analytic solution of stochastic completion fields. *Biological Cybernetics*, 75:141–151, 1996.
73. D. Y. Ts'o, R. D. Frostig, E. E. Lieke, and A. Grinvald. Functional organization of primate visual cortex revealed by high resolution optical imaging. *Science*, 249:417–20, 1990.
74. S. Twareque Ali. A general theorem on square-integrability: Vector coherent states. *Journal of Mathematical Physics*, 39, 1998. Number 8.
75. M. A. van Almsick, R. Duits, E. Franken, and B.M. ter Haar Romeny. From stochastic completion fields to tensor voting. In *Proceedings DSSCC-workshop on Deep Structure Singularities and Computer Vision*, pages –, Maastricht the Netherlands, June 9-10 2005. Springer-Verlag.
76. J. Weickert. Coherence enhancing diffusion, *IJCV* 31(3), p. 111–127, 1999.
77. L. R. Williams and J.W. Zweck. A rotation and translation invariant saliency network. *Biological Cybernetics*, 88:2–10, 2003.
78. J. Wloka. *Partial Differential Equations*. Cambridge University Press, 1987.